


REPORT DOCUMENTATION PAGE				Form Approved OMB No. 0704-0188	
<small>Public reporting burden for this collection of information is estimated to average 1 hour per response, including the time for reviewing instructions, searching existing data sources, gathering and maintaining the data needed, and completing and reviewing the collection of information. Send comments regarding this burden estimate or any other aspect of this collection of information, including suggestions for reducing the burden, to Department of Defense, Washington Headquarters Services, Directorate for Information Operations and Reports (0704-0188), 1215 Jefferson Davis Highway, Suite 1204, Arlington, VA 22202-4302. Respondents should be aware that notwithstanding any other provision of law, no person shall be subject to any penalty for failing to comply with a collection of information if it does not display a currently valid OMB control number.</small> PLEASE DO NOT RETURN YOUR FORM TO THE ABOVE ADDRESS.					
1. REPORT DATE (DD-MM-YYYY) 22-07-2004		2. REPORT TYPE Final Report		3. DATES COVERED (From – To) 01-Jul-02 - 01-Jul-04	
4. TITLE AND SUBTITLE Theoretical Studies of Boundary Layer Receptivity			5a. CONTRACT NUMBER ISTC Registration No: 2393		
			5b. GRANT NUMBER		
			5c. PROGRAM ELEMENT NUMBER		
6. AUTHOR(S) Dr. Alexandre Fedorov			5d. PROJECT NUMBER		
			5d. TASK NUMBER		
			5e. WORK UNIT NUMBER		
7. PERFORMING ORGANIZATION NAME(S) AND ADDRESS(ES) Moscow Institute of Physics and Technology 16 Gagarin St Zhukovsky 140180 Russia				8. PERFORMING ORGANIZATION REPORT NUMBER N/A	
9. SPONSORING/MONITORING AGENCY NAME(S) AND ADDRESS(ES) EOARD PSC 802 BOX 14 FPO 09499-0014				10. SPONSOR/MONITOR'S ACRONYM(S)	
				11. SPONSOR/MONITOR'S REPORT NUMBER(S) ISTC 01-7035	
12. DISTRIBUTION/AVAILABILITY STATEMENT Approved for public release; distribution is unlimited.					
13. SUPPLEMENTARY NOTES					
14. ABSTRACT This report results from a contract tasking Moscow Institute of Physics and Technology as follows: To predict boundary-layer transition in a rational way and capture its sensitivity to freestream noise, turbulence, surface roughness, steps/gaps/waviness, etc., a toolbox combining receptivity theory with nonlinear Parabolized Stability Equations and Direct Navier-Stokes Simulation is needed. This project addresses this need with theoretical modeling of high speed boundary-layer receptivity to acoustic disturbances as they interact with 3D roughness elements and waviness. The effort is basic, theoretical research on receptivity. Using the multiple-modes method, a compact and computationally robust algorithm providing fast calculations of receptivity characteristics will be developed. This algorithm will be integrated into a computational module that can be linked with a standard stability solver. Receptivity calculations will be made for the conditions relevant to future experiments in the new high Reynolds-number, Mach-6, quiet 'Ludwig' tube of Purdue University. This will help to formulate recommendations for design of receptivity experiments and interpretation of the data. The results of the project can also be applied at the component level to assess laminar flow control concepts.					
15. SUBJECT TERMS EOARD, Physics, Fluid Mechanics					
16. SECURITY CLASSIFICATION OF:			17. LIMITATION OF ABSTRACT UL	18. NUMBER OF PAGES	19a. NAME OF RESPONSIBLE PERSON WAYNE A. DONALDSON
a. REPORT UNCLAS	b. ABSTRACT UNCLAS	c. THIS PAGE UNCLAS			19b. TELEPHONE NUMBER (Include area code) +44 (0)20 7514 4299

Rector of MIPT



Professor N.N. Kudryavtsev

" 7 " 07 2004



**Final
Project Technical Report
of ISTC 2393**

Theoretical Studies of Boundary Layer Receptivity*

(From 1 July 2002 to 30 June 2004 for 24 months)

**Yuri Vladimirovich Manoshkin
(Project Manager)**

**Alexander Vitalievich Fedorov
(Principle Investigator)**

Moscow Institute of Physics and Technology

June 2004

* This work was supported financially by European Office of Aerospace Research and Development and performed under the contract to the International Science and Technology Center (ISTC), Moscow.

Theoretical Studies of Boundary Layer Receptivity
(From 1 July 2002 to 30 June 2004 for 24 months)

Yuri Vladimirovich Manoshkin (Project Manager) and
Alexander Vitalievich Fedorov (Principle Investigator)
Moscow Institute of Physics and Technology*

The objectives of this project are:

1. Extend the receptivity models developed for 2-D disturbances to 3-D disturbances to treat receptivity of high-speed boundary layers to acoustics, vorticity and entropy fluctuations interacting with 3-D roughness/waviness.
2. Package the theoretical model in a computational module with input and output to be accessible for a standard stability solver or PSE code.

Analyses of high-speed boundary layer receptivity to three-dimensional external waves interacting with roughness element or waviness were performed. The FORTRAN computational module RECEPT.FOR was developed and delivered to the end user Dr. Roger Kimmel with the usage instructions. This module allows for calculations of the receptivity coefficients and the weight coefficients of unstable modes. It was shown that the module RECEPT extracts the normal wave of relatively small amplitude ($\sim 0.1\%$) from the disturbance field. With this tool, the user can identify normal waves, which latent in a “messy” disturbance field at early stages of instability. The module RECEPT was applied to the problem of high-speed boundary-layer receptivity to acoustic disturbances interacting with three-dimensional roughness element. This option was demonstrated by numerical examples. Namely, the receptivity coefficients were calculated for two-dimensional second mode and three-dimensional Tollmien-Schlichting waves. Recommendations for design of receptivity experiments in supersonic quiet wind tunnels were formulated. This helps to reduce the risk and cost of experiments, especially in high-speed wind tunnels where runs are quite expensive.

Keywords (about 10 words): high speed, boundary layer, receptivity, computational module, acoustic waves, roughness, unstable disturbances.

* 141700 Dolgoprudnyj Moscow Region Institutskij per. 9
Phone: 7 (095) 408 5700, Fax: 7 (095) 408 6869

E-mail: rector@mipt.ru

The work was performed by the following institutes and collaborators

1. Participated institutes:

1.1 Leading institute:

Moscow Institute of Physics and Technology
141700 Dolgoprudnyj Moscow Region Institutskij per. 9
Telephone: 7 (095) 408 5700
Fax: 7 (095) 408 6869
E-mail: rector@mipt.ru

1.2 Subcontracted institutes: No

2. Foreign Collaborators

European Office of Aerospace Research and Development
223-231 Old Marylebone Road, London, United Kingdom, NW1 5TH
Phone +44 (0) 20 7514 4953, Fax +44 (0) 20 7514 4960
Email: wayne.donaldson@london.af.mil

Abstract

Laminar-turbulent transition is relevant to many aspects of high-speed vehicle design. Early transition causes a significant increase in heat transfer. Higher heating requires a higher-performance thermal protection system or active cooling that increases cost and weight. Vehicle drag, engine performance and vehicle aerodynamics are also affected. Since transition prediction methods currently used in engineering practice are subject to great uncertainty, conservative worst-case conditions are normally assumed in vehicle design. For existing or near-term vehicles, the payoff for improved transition prediction is enhanced performance. For extended cruise airbreathers, transition prediction and control may be critical to achieving design requirements. Most transition prediction methods have been, at best, semi-empirical. To predict boundary-layer transition in a rational way and capture its sensitivity to freestream noise, turbulence, surface roughness, steps/gaps/waviness, etc., a toolbox combining receptivity theory with linear stability solvers is needed. This project addresses this need with theoretical modeling of high-speed boundary-layer receptivity to acoustic disturbances as they interact with 3-D roughness elements and waviness. The study is based on combined asymptotic and numerical approach. Using the multiple-modes method, the receptivity models for 2-D disturbances are extended to the 3-D case to handle interaction of acoustics, vorticity and entropy spottiness with 3-D roughness/waviness of aerodynamic surfaces. These models are used to develop a compact and computationally robust algorithm providing fast calculations of receptivity characteristics. The numerical algorithm is integrated into the FOPRTRAN module RECEPT that can be linked with a standard stability solver. This module allows for calculations of the receptivity coefficients and weight coefficients of various modes of the discrete spectrum: TS waves, second mode, cross-flow instability etc.

Table of Contents

Nomenclature	6
List of figures	7
Introduction	11
1. Basic relations	13
1.1 Disturbance field.....	13
1.2 Resonant excitation of a discrete mode by an external wave interacting with wall waviness.....	14
1.3 Excitation of a discrete mode by an external wave interacting with a local hump.....	15
1.4 Weight coefficients	16
1.5 Summary.....	16
2. Receptivity module RECEPT and usage instructions	16
2.1 Mean flow.....	17
2.2 Solutions of direct and adjoint problems.....	18
2.3 Solution for external wave.....	20
2.4 Solution for stationary disturbance induced by wavy wall.....	21
2.5 Disturbance field.....	21
2.6 Options of RECEPT.FOR.....	22
3. How to use the module output?	24
4. Weight coefficients	25
5. Receptivity coefficients for 2-D second mode generated by 3-D acoustic waves interacting with local 3-D roughness element	31
5.1 Problem formulation and basic relations.....	31
5.2 Numerical results.....	33
6. Receptivity coefficients for 3-D Tollmien-Schlichting waves generated by acoustic waves interacting with local 3-D roughness element	44
6.1 Problem formulation and basic relations.....	44
6.2 Numerical results.....	45
7. Recommendations for design of receptivity experiments in quiet wind tunnels	58
8. Conclusions	63
9. Future effort	64
References	65
List of papers	68
Appendix	69

Nomenclature

A	eigenfunction vector (direct problem)
B	eigenfunction vector (conjugate problem)
C	phase velocity
c	receptivity coefficient or weight coefficient
$F = \omega^* \nu_e^* / U_e^{*2}$	frequency parameter
$\mathbf{F}(x, y, z)$	vector-function of disturbance amplitude
g	roughness shape function
G	matrix of nonlinear interaction of external wave with roughness
h	roughness amplitude
H_0	matrix of linear stability problem
M	Mach number at the upper boundary-layer edge
p	pressure disturbance
q_m	mass-flux disturbance
$R = U_e^* \delta^* / \nu_e^*$	Reynolds number
t	time
T	mean-flow temperature
U, V, W	mean-flow velocity
u, v, w	velocity disturbance
x, y, z	Cartesian coordinates
x_0	resonance point
$(x', z') = (x - x_0, z - z_0)$	local coordinates
$x_1 = x^* / x_0^* = \varepsilon x$	slow variable
α, β	wave-vector components in x - and z -direction respectively
δ^*	boundary-layer scale
$\varepsilon = \delta^* / x_0^*$	small parameter
γ	specific heat ratio
μ	viscosity
ν	kinematic viscosity
ρ_e^*	mean-flow density at the upper boundary-layer edge
$\rho(\alpha, \beta)$	Fourier component of the shape-function $g(x', z')$
ω	angular frequency
θ	temperature disturbance
Ψ	disturbance vector-function
<i>Superscripts:</i>	
*	dimensional
T	transposed

Subscripts:

0	resonance point
a	external disturbance
e	upper boundary
i	imaginary
r	real
w	roughness induced
2-D	two-dimensional
3-D	three-dimensional
DNS	direct numerical simulation
LST	linear stability theory
PSE	parabolized stability equations
TPS	thermal protection system
TS	Tollmien-Schlichting

List of figures

		Page
Figure 1a	Mean-flow velocity profile; $M_e = 6$, $T_w = T_{ad}$	27
Figure 1b	Mean-flow temperature profile; $M_e = 6$, $T_w = T_{ad}$	28
Figure 2	The real part of pressure distributions for acoustic wave $\mathbf{F}_a(y)$, the second mode $\mathbf{F}_2(y)$, and the disturbance field $\mathbf{F}_0(y) = \mathbf{F}_a(y) + \mathbf{F}_2(y)$; $R = 10^3$, $F = 1.3 \times 10^{-4}$	28
Figure 3	The weight coefficients predicted by RECEPT at various upper boundaries y_1	29
Figure 4a	Real part of the second-mode eigenvalue α_2 as a function of the sweep angle Θ_z ; $M_e = 6$, $T_w = T_{ad}$, $R = 10^3$, $F = 1.3 \times 10^{-4}$	29
Figure 4b	Imaginary part of the second-mode eigenvalue α_2 as a function of the sweep angle Θ_z ; $M_e = 6$, $T_w = T_{ad}$, $R = 10^3$, $F = 1.3 \times 10^{-4}$	30
Figure 5	The weight coefficient of the second mode predicted by the RECEPT for various sweep angles Θ_z ; $M_e = 6$, $T_w = T_{ad}$, $R = 10^3$, $F = 1.3 \times 10^{-4}$	30
Figure 6	Schematics of incident acoustic wave interacting with local roughness element	35

Figure 7a	Profile of mean-flow velocity	36
Figure 7b	Profile of mean-flow temperature	36
Figure 8a	The real part of second-mode eigenvalue $\text{Re } \alpha_2$ as a function of Reynolds number. R	37
Figure 8b	The second-mode growth rate $\sigma = -\text{Im } \alpha_2$ as a function of Reynolds number R	37
Figure 8c	The second-mode phase speed $C_2 = \text{Re}(\omega / \alpha_2)$ as a function of Reynolds number R	38
Figure 9a	The receptivity coefficient modulus $ c(\Theta_y, \Theta_z) $ at the roughness element locus $R_0 = 500$ (upstream from the neutral point); fast acoustic waves; angles are given in degrees	38
Figure 9b	The receptivity coefficient modulus $ c(\Theta_y, \Theta_z) $ at the roughness element locus $R_0 = 1000$ (neutral point); fast acoustic waves; angles are given in degrees	39
Figure 9c	The receptivity coefficient modulus $ c(\Theta_y, \Theta_z) $ at the roughness element locus $R_0 = 1500$ (downstream from the neutral point); fast acoustic waves; angles are given in degrees	39
Figure 10a	The receptivity coefficient modulus $ c(\Theta_y, \Theta_z) $ at the roughness element locus $R_0 = 500$ (upstream from the neutral point); slow acoustic waves; angles are given in degrees	40
Figure 10b	The receptivity coefficient modulus $ c(\Theta_y, \Theta_z) $ at the roughness element locus $R_0 = 1000$ (neutral point); slow acoustic waves; angles are given in degrees	40
Figure 10c	The receptivity coefficient modulus $ c(\Theta_y, \Theta_z) $ at the roughness element locus $R_0 = 1500$ (downstream from the neutral point); slow acoustic waves; angles are given in degrees	41
Figure 11a	The real part of $c(\Theta_y, \Theta_z)$ at the roughness element locus $R_0 = 1000$ (neutral point); fast acoustic waves; angles are given in degrees	41

Figure 11b	The imaginary part of $c(\Theta_y, \Theta_z)$ at the roughness element locus $R_0 = 1000$ (neutral point); fast acoustic waves; angles are given in degrees	42
Figure 12a	The real part of $c(\Theta_y, \Theta_z)$ at the roughness element locus $R_0 = 1000$ (neutral point); slow acoustic waves; angles are given in degrees	42
Figure 12b	The imaginary part of $c(\Theta_y, \Theta_z)$ at the roughness element locus $R_0 = 1000$ (neutral point); slow acoustic waves; angles are given in degrees	43
Figure 13a	Profile of mean-flow velocity, boundary-layer thickness $\eta_\delta \approx 9.2$, $M = 2.98$	47
Figure 13b	Profile of mean-flow temperature on adiabatic plate, $M = 2.98$	48
Figure 14a	The real part of TS eigenvalue $\text{Re } \alpha_{TS}$ as a function of Reynolds number R and F_β	48
Figure 14b	The TS growth rate $\sigma_{TS} = -\text{Im } \alpha_{TS}$ as a function of Reynolds number R and F_β	49
Figure 15a	Receptivity coefficient as a function of F_β for fast acoustic wave of $\Theta_y = 45^\circ$, $\Theta_z = 0$; $R = 620$, $F = 1.4 \times 10^{-5}$	49
Figure 15b	Receptivity coefficient as a function of φ_w for fast acoustic wave of $\Theta_y = 45^\circ$, $\Theta_z = 0$; $R = 620$, $F = 1.4 \times 10^{-5}$	50
Figure 16	Orientations of the wave-front of resonant waviness with respect to Mach waves	50
Figure 17a	Receptivity coefficient as a function of F_β for fast acoustic wave of $\Theta_y = 0$, $\Theta_z = 45^\circ$; $R = 620$, $F = 1.4 \times 10^{-5}$	51
Figure 17b	Receptivity coefficient as a function of φ_w for fast acoustic wave of $\Theta_y = 0$, $\Theta_z = 45^\circ$; $R = 620$, $F = 1.4 \times 10^{-5}$	51
Figure 18	The function $\lambda_1(F_\beta)$ for the case of fast acoustic wave of $\Theta_y = 0$, $\Theta_z = 45^\circ$, $R = 620$, $F = 1.4 \times 10^{-5}$	52

Figure 19	Distributions of the x -component velocity induced by the wavy wall in the vicinity of the transonic point $F_\beta \approx 5.5 \times 10^{-5}$	53
Figure 20	Distributions of the y -component velocity induced by the wavy wall in the vicinity of the transonic point $F_\beta \approx 5.5 \times 10^{-5}$	54
Figure 21	Modulus of receptivity coefficient as a function of the fast acoustic-wave angles Θ_y and Θ_z ; $R = 620$, $F = 1.4 \times 10^{-5}$, $F_\beta = 6.8 \times 10^{-5}$	54
Figure 22a	Receptivity coefficient as a function of F_β for slow acoustic wave of $\Theta_y = 45^\circ$, $\Theta_z = 0$; $R = 620$, $F = 1.4 \times 10^{-5}$	55
Figure 22b	Receptivity coefficient as a function of φ_w for slow acoustic wave of $\Theta_y = 45^\circ$, $\Theta_z = 0$; $R = 620$, $F = 1.4 \times 10^{-5}$	55
Figure 23a	Receptivity coefficient as a function of F_β for slow acoustic wave of $\Theta_y = 0$, $\Theta_z = 45^\circ$; $R = 620$, $F = 1.4 \times 10^{-5}$	56
Figure 23b	Receptivity coefficient as a function of φ_w for slow acoustic wave of $\Theta_y = 0$, $\Theta_z = 45^\circ$; $R = 620$, $F = 1.4 \times 10^{-5}$	56
Figure 24	Modulus of receptivity coefficient as a function of the slow acoustic-wave angles Θ_y and Θ_z ; $R = 620$, $F = 1.4 \times 10^{-5}$, $F_\beta = 6.8 \times 10^{-5}$; dashed red lines shows Θ_y and Θ_z of transonic resonant waviness	57
Figure 25	Hot-wire measurements of disturbances generated by acoustic wave train in supersonic boundary layer	60
Figure 26	Acoustic sources at various positions (red and black points) radiate the roughness element by wave trains of various front angles Θ_y	61
Figure 27	Receptivity to acoustic waves interacting with 2-D roughness element (strip)	61
Figure 28	Receptivity to acoustic waves interacting with 3-D periodic roughness element	62

Introduction

Laminar-turbulent transition is relevant to many aspects of high-speed vehicle design [1,2]. Early transition causes a significant increase of heat transfer. Higher heating requires a higher-performance thermal protection system (TPS) or active cooling that increases cost and weight. Even modest savings in TPS weight can translate into significant payload increases due to the low payload mass fraction. Vehicle drag, engine performance and vehicle aerodynamics are also affected. Since transition prediction methods currently used in engineering practice are subject to great uncertainty, conservative worst-case conditions are normally assumed in vehicle design. For existing or near-term vehicles, the payoff for improved transition prediction is enhanced performance. For extended cruise airbreathers, transition prediction and control may be critical to achieving design requirements.

Boundary layer transition is difficult to predict due to its sensitivity to initial conditions. Most transition prediction methods have been, at best, semi-empirical. Recent research opens a possibility of first-principles transition prediction accounting for freestream disturbance levels and surface non-uniformities. The process by which freestream disturbances interact with the boundary layer and engender instabilities that lead to turbulence is termed receptivity. This project extends past basic theoretical research on receptivity funded by EOARD, AFOSR, and AFRL to develop the theory and computational modules predicting receptivity of the boundary layer on a rough surface exposed to acoustic noise or other external disturbances (vortical waves and entropy spottiness).

It is possible to identify two major routes to turbulence. The first route is observed in a low-disturbance environment typical for flight and quiet wind tunnels. In this case, the transition process can be treated as an initial boundary-value problem that comprises excitation of unstable boundary-layer modes (receptivity phase), their downstream amplification (linear stability phase) and nonlinear breakdown to turbulence [3, 4]. The second route is observed in high-disturbance environments and associated with “bypass” of the linear phase [5]. This project addresses the first route of transition for high-speed boundary layers.

Reviews on transition prediction methods [6-10] indicate good progress in modeling of the linear stability phase including three-dimensional stability codes under the quasi-parallel approximation [11] and non-parallel linear stability codes based on the multiple-scales method [12-14]. Parabolized stability equations (PSE) methods [15-17] enable capturing of both non-parallel and weakly non-linear effects. Direct numerical simulations (DNS) [18] provide insight into breakdown mechanisms. Despite this progress, the operative transition prediction method remains the e^N method [10], which does not consider receptivity and nonlinear breakdown. These phases are incorporated into the value N , which is calibrated for a particular set of experimental data. Malik [10] reported that the e^N method (with $N \approx 10$) provides an upper bound on the transition location relevant to an extremely low-disturbance limit whereas the lower bound ($N \approx 1$) corresponds to bypass. These two limits are often wide apart and transition occurs anywhere in between. To predict the transition locus in a rational way and capture its sensitivity to freestream noise and turbulence, surface roughness, steps/gaps/waviness, etc., one needs a more sophisticated toolbox, which combines receptivity theory with stability theory.

A number of theoretical models have been developed for receptivity of high-speed boundary layers including sharp leading-edge receptivity to freestream acoustic and vortical disturbances [19, 20], receptivity to vortical/entropy disturbances near the lower branch of the neutral curve [21], local and distributed receptivity to wall-induced disturbances such as skin vibrations [22,23], and receptivity to external disturbances interacting with a small roughness/waviness [22,24]. The multiple-modes method described in [24] (see also [21]) serves as a general formalism for the aforementioned theoretical models. This provides a good launching pad for further extension of receptivity studies to more practical cases accessible for experimental verification.

Important mechanism of boundary-layer receptivity is the interaction of acoustic disturbances with steady disturbances induced by spatial variations of boundary conditions on the wall surface such as roughness/waviness, local heating/cooling and suction/blowing. Early experimental [25] and theoretical [26-28] studies of this mechanism were performed in Russia for subsonic flows. Their results were summarized in Ref. [24]. An asymptotic theory of the Tollmien-Schlichting (TS) wave excitation due to interaction of acoustic waves with surface irregularities was developed in Refs. [29-31] and reviewed in Refs. [31-33]. Detailed parametrical studies were discussed in Refs. [34-37]. The theoretical predictions are in good agreement with the experiment [38] conducted on a flat plate in low-speed wind tunnel.

Choudhari and Streett [39] analyzed receptivity of high-speed boundary layers (in the Mach number range from 1.15 to 4.5) to freestream disturbances interacting with surface irregularities. They reported that, although the Mach=4.5 boundary layer is nearly 6 times thicker than in the Mach=0 case, the instability amplitudes generated by a wall hump of fixed height are only marginally smaller than those at low speeds. This example indicates that receptivity of high-speed boundary layer to acoustic plus roughness disturbances may play important role in the initial phase of transition.

In many cases, it is needed to identify a particular mode of discrete spectrum in a disturbance field, which is resulted from DNS or experimental measurements. This is not a trivial problem because the disturbance field may contain many modes of discrete and continuous spectra. The unstable mode may be latent in such a “messy” field, especially in early phases of instability evolution when the amplitude of unstable waves is relatively small. This motivated us to include in the receptivity module an option providing calculations of the weight coefficients for disturbances of discrete spectrum (TS waves, second mode etc.)

In this report, we describe the FORTRAN receptivity module RECEPT.FOR and discuss basic features of receptivity to acoustic waves interacting with roughness elements. In Section 1, we outline basic relations incorporated into the module. The theoretical analysis leading to these relations is presented in Appendix. In Section 2, we discuss the module input and output and explain how to couple the module with a linear stability solver. In Section 3, we illustrate how to use the module output for calculations of physical quantities. In Section 4, we present numerical examples demonstrating computations of the weight coefficients. In Section 5, we consider receptivity for 2-D second mode generated by 3-D acoustic waves interacting with local 3-D roughness element. For Mach=6 boundary layer on a flat plate, we present numerical results illustrating distributions of the receptivity coefficient versus the angles of inclination and incidence of fast and slow acoustic waves. In Section 6, we discuss receptivity for 3-D Tollmien-

Schlichting (TS) waves. Using the module RECEPT we calculate the receptivity coefficient for various angles of acoustic and TS waves. Special attention is paid to the fact that the receptivity coefficient is singular if the resonant roughness component is transonic; i.e., the freestream velocity normal to the waviness front equals to the speed of sound. In Section 7, we formulate recommendations for design of receptivity experiments in quiet high-speed wind tunnels. In Section 8, we conclude the report, and in Section 9 we discuss the future effort.

1. Basic relations

Herein we briefly summarize basic analytical relations, which are incorporated into the FORTRAN module RECEPT.FOR. Details of the theoretical analysis are given in Appendix.

Consider the boundary layer on a 2-D body (planar or axisymmetric), on a swept wing or similar configurations for which the boundary layer is predominantly two-dimensional. At a certain streamwise station $x^* = x_0^*$, the mean-flow profiles are

$$\begin{aligned} U &\equiv U^* / U_e^* = U(y), \quad W \equiv W^* / U_e^* = W(y), \\ T &\equiv T^* / T_e^* = T(y). \end{aligned} \quad (1.1)$$

Hereafter the longitudinal x^* , normal y^* , transversal z^* coordinates and time t^* are made nondimensional using the boundary-layer length scale δ^* and the velocity U_e^* as

$$(x, y, z) = (x^*, y^*, z^*) / \delta^*, \quad t = t^* U_e^* / \delta^*, \quad (1.2)$$

where subscript “e” denotes quantities at the upper boundary-layer edge. Introduce the small parameter $\varepsilon = \delta^* / x_0^*$, which is a ratio of the boundary-layer scale to the global scale x_0^* . If the boundary-layer scale is specified as $\delta^* = \sqrt{\nu_e^* x_0^* / U_e^*}$, then the Reynolds number is $R = \sqrt{U_e^* x_0^* / \nu_e^*} = \varepsilon^{-1}$. The slow streamwise variable is defined as $x_1 = \varepsilon x$. The vertical velocity component $V \equiv V^* / U_e^* = O(\varepsilon)$ is neglected in the first-order approximation.

Disturbances of the velocity components (u, v, w) , pressure p and temperature θ are nondimensionalized as

$$(u, v, w) = \frac{(u^*, v^*, w^*)}{U_e^*}, \quad p = \frac{p^*}{\rho_e^* U_e^{*2}}, \quad \theta = \frac{\theta^*}{T_e^*}. \quad (1.3)$$

1.1 Disturbance field

A disturbance of angular frequency ω is given by the vector function

$$\Psi = (u, \frac{\partial u}{\partial y}, v, p, \theta, \frac{\partial \theta}{\partial y}, w, \frac{\partial w}{\partial y})^T. \quad (1.4)$$

The disturbance field comprises: the stationary disturbance induced by the wall roughness of the amplitude h ; the external disturbance of continuous spectrum with the amplitude ε_a ; modes of discrete spectrum

$$\Psi = h\mathbf{Q}_w(x, y, z) + \varepsilon_a \mathbf{F}_a(x_1, y) \exp(i\alpha_a x + i\beta_a z - i\omega t) + \mathbf{F}(x, y, z) \exp(-i\omega t) + (c.c). \quad (1.5)$$

The disturbance of continuous spectrum may be acoustic wave, vortical wave or entropy wave. Hereafter these waves are called “external waves”. Modes of the discrete spectrum are expressed in the form

$$\mathbf{F} = h\varepsilon_a \sum_n [\mathbf{F}_{n0}(x_1, y) + \varepsilon \mathbf{F}_{n1}(x_1, y) + \dots] \exp(i\varepsilon^{-1} S_n + i\beta z), \quad (1.6)$$

$$S_n = \int_{x_{1s}}^{x_1} \alpha_n(x_1, \omega, \beta) dx_1, \quad \alpha_n = \alpha_n(x_1, \omega, \beta), \quad (1.7)$$

where the amplitude of Mode “ n ” is

$$\mathbf{F}_{n0} = c_n(x_1) \mathbf{A}_n(x_1, y, \alpha_n), \quad \alpha_n = \alpha_n(x_1, \omega, \beta). \quad (1.8)$$

1.2 Resonant excitation of a discrete mode by an external wave interacting with the wall waviness

The stationary disturbance induced by a wavy wall is expressed as

$$\mathbf{Q}_w = \mathbf{F}_w(x_1, y) \exp(i\alpha_w x + i\beta_w z) + (c.c). \quad (1.9)$$

At the station $x = x_0$, the roughness wave-number is determined from the resonance conditions

$$\alpha_w = \alpha_n(x_{10}, \omega, \beta) - \alpha_a, \quad \beta_w = \beta - \beta_a. \quad (1.10)$$

The amplitude of Mode “ n ”, propagating downstream from the resonance point x_0 , is

$$\mathbf{F}_n = \varepsilon_a h c_n(x_{10}, \beta) \mathbf{A}_n(x_1, y) \exp \left[i\varepsilon^{-1} \int_{x_{10}}^{x_1} \alpha_n(x_1) dx_1 + i\beta z \right], \quad x_1 > x_{10}; \quad (1.11)$$

$$c_n(x_{10}, \beta) = \varepsilon^{-1/2} q \sqrt{\frac{2\pi i}{b}}, \quad (1.12)$$

$$b = \frac{\partial \alpha_n}{\partial x_1}(x_{10}), \quad (1.13)$$

$$q = - \frac{i \langle \mathbf{B}_0, G(x_{10}) \mathbf{F}_a \rangle}{\langle \mathbf{B}_0, \frac{\partial H_0}{\partial \alpha}(x_{10}, \alpha_0) \mathbf{A}_0 \rangle}, \quad (1.14)$$

$$\alpha_0 = \alpha_n(x_{10}, \omega, \beta), \quad \mathbf{A}_0 = \mathbf{A}_n(x_{10}, y, \alpha_0), \quad \mathbf{B}_0 = \mathbf{B}_n(x_{10}, y, \alpha_0). \quad (1.15)$$

Here c_n is receptivity coefficient, which couples the amplitudes of external disturbance and wavy wall with the amplitude of Mode n at the station $x_1 = x_{10}$. Derivation of these relations and definitions of other quantities are given in Appendix.

1.3 Excitation of a discrete mode by an external wave interacting with a local hump

It is assumed that the surface roughness is a local hump of the shape

$$y_w(x, y, z) = hg(x', z'), \quad x' = x - x_0, \quad z' = z - z_0. \quad (1.16)$$

Fourier transform of $g(x', z')$ is expressed as

$$\rho(\alpha_w, \beta_w) = \int_{-\infty}^{+\infty} dz' \int_{-\infty}^{+\infty} dx' g(x', z') \exp(-i\alpha_w x' - i\beta_w z'). \quad (1.17)$$

For a two-dimensional hump with $g = g(x')$ and $\beta_w = 0$, Mode n has the amplitude

$$\mathbf{F}_n = \varepsilon_a h c_n(x_{10}, \beta) \mathbf{A}_n(x', y) \exp \left(i \int_0^{x'} \alpha_n(x') dx' + i\beta z \right), \quad x_1 > x_{10}; \quad (1.18)$$

$$c_n(x_{10}, \beta) = q\rho(\alpha_{w0}), \quad (1.19)$$

$$\alpha_{w0} = \alpha_n(x_{10}, \omega, \beta) - \alpha_a, \quad \beta = \beta_a. \quad (1.20)$$

For a three-dimensional hump with $g = g(x', z')$, Mode n has the amplitude

$$\mathbf{F}_n = \frac{\varepsilon_a h}{2\pi} \int_{-\infty}^{+\infty} c_n(x_{10}, \beta) \mathbf{A}_n(x_1, y; \beta) \exp \left(i\varepsilon^{-1} \int_{x_{10}}^{x_1} \alpha_n(x_1) dx_1 + i\beta z' \right) d\beta, \quad x_1 > x_{10}; \quad (1.21)$$

$$c_n(x_{10}, \beta) = q\rho(\alpha_{w0}, \beta_w), \quad (1.22)$$

$$\alpha_{w0} = \alpha_n(x_{10}, \omega, \beta) - \alpha_a, \quad \beta = \beta_w + \beta_a. \quad (1.23)$$

1.4 Weight coefficients

In many cases, it is needed to identify a mode of the discrete spectrum, say Mode n , in a disturbance field, which is resulted from DNS or experimental measurements. This is not a trivial problem because the disturbance field may contain many modes of discrete and continuous spectra. The amplitude of unstable mode may be latent in such a “messy” field, especially in early stages of instability.

The weight coefficient of a particular discrete mode is calculated as follows. The disturbance field is assumed to be known. Performing Fourier transform with respect to t and z , we obtain

$$\mathbf{Q} = \mathbf{F}(x, y) \exp(i\beta z - i\omega t). \quad (1.24)$$

This Fourier component may contain modes of discrete spectrum (TS wave, second mode, etc.), which are solutions of the eigenvalue problem. If the disturbance field at a particular station $x = x_0$ is $\mathbf{F}_0(y) = \mathbf{F}(x_0, y)$, then Mode n of the eigenvalue $\alpha_n(x_0, \omega, \beta)$ has the amplitude

$$\mathbf{F}_n = c_n(x_0, \beta) \mathbf{A}_n(x_0, y, \alpha_n), \quad (1.25)$$

where the weight coefficient is expressed as

$$c_n(x_0, \beta) = \frac{\langle \frac{\partial H_0}{\partial \alpha}(x_0, \alpha_n) \mathbf{F}_0, \mathbf{B}_n \rangle}{\langle \frac{\partial H_0}{\partial \alpha}(x_0, \alpha_n) \mathbf{A}_n, \mathbf{B}_n \rangle}. \quad (1.26)$$

1.5 Summary

Basic relations of Sections 1.1 and 1.2 have similar structures. This allows for the development of a compact computational module, which calculates:

- Receptivity coefficients $c_n(x_{10}, \beta)$ given by (1.12), (1.22) for the case of receptivity to external wave interacting with roughness-induced disturbance
- Weight coefficient $c_n(x_{10}, \beta)$ given by (1.26).

This module can be linked with a standard linear stability solver as described in Section 2.

2. Receptivity module RECEPT and usage instructions

The FORTRAN module RECEPT.FOR calculates:

- The coefficient (1.12) for receptivity to external wave interacting with a wavy surface
- The coefficient (1.22) for receptivity to external wave interacting with a local hump
- The weight coefficient (1.26) for a given disturbance field

In this version, it is assumed that the branch points of the discrete spectrum are far from the resonance region; i.e. $\langle \frac{\partial H_0}{\partial \alpha}(x_0, \alpha_n) \mathbf{A}_n, \mathbf{B}_n \rangle \neq 0$ (see Appendix).

The RECEP.FOR is a FORTRAN subroutine, which needs to be linked with a linear stability solver. In order to specify the full input for this module, the user should follow steps indicated in Sections 2.1-2.3. Note that not all of the input data are needed for a particular option. Subsets of data for different options are given in Section 2.4.

2.1 Mean flow

2.1.1 Specify gas parameters:

PR - Prandtl number (real)

G = γ - specific heat ratio (real)

$K \equiv e = \frac{3 \text{ (bulk viscosity)}}{2 \text{ (viscosity)}}$ (real)

(K=0. corresponds to Stokes hypothesis; K=1.2 was recommended by L. Mack)

2.1.2 Specify the mean-flow profiles and their derivatives with respect to y at station $x_1 = x_{10}$

$$\begin{aligned} (U, W, T), (DU, DW, DT) &= \left(\frac{\partial U}{\partial y}, \frac{\partial W}{\partial y}, \frac{\partial T}{\partial y} \right), \\ (D^2U, D^2W, D^2T) &= \left(\frac{\partial^2 U}{\partial y^2}, \frac{\partial^2 W}{\partial y^2}, \frac{\partial^2 T}{\partial y^2} \right), \end{aligned} \quad (2.1)$$

as well as the distributions of viscosity and its derivatives with respect to the gas temperature

$$\frac{\mu^*}{\mu_e} = \mu(y), \quad \mu'(y) = \frac{d\mu}{dT}(y), \quad \mu''(y) = \frac{d^2\mu}{dT^2}(y) \quad (2.2)$$

2.1.3 Specify the local Mach number $M = \frac{U_e^*}{a_e}$ at the upper boundary $y = y_e$ (real)

2.1.4 Store these data in the common blocks:

COMMON/OUT/K,PR,G,M

COMMON/BASA5/NBAS,YY,BU,BU1,BU2,BT,BT1,BT2
*,BW,BW1,BW2,BMU,BMU1,BMU2

where

YY(I)= y (real), I=1,...,NBAS;

BU(I)= U (real), I=1,...,NBAS;

BU1(I)=DU (real), I=1,...,NBAS;
 BU2(I)= D²U (real), I=1,...,NBAS;
 BT(I)=T (real), I=1,...,NBAS;
 BT1(I)=DT (real), I=1,...,NBAS;
 BT2(I)= D²T (real), I=1,...,NBAS;
 BW(I)=W (real), I=1,...,NBAS;
 BW1(I)=DW (real), I=1,...,NBAS;
 BW2(I)= D²W (real), I=1,...,NBAS;
 BMU(I)=μ (real), I=1,...,NBAS;
 BMU1(I)= $\frac{d\mu}{dT}$ (real), I=1,...,NBAS;
 BMU2(I)= $\frac{d^2\mu}{dT^2}$ (real), I=1,...,NBAS;

NBAS =number of grid points in the range $0 \leq y \leq y_e$; y_e is upper boundary of the integration domain.

2.2 Solutions of direct and adjoint problems

2.2.1 Specify the disturbance angular frequency ω , the wave-number component β and the Reynolds number R . Solve the direct eigenvalue problem for a particular mode of discrete spectrum (say Mode “n”) at the station $x_1 = x_{10}$

$$\begin{aligned}
 \frac{d\mathbf{A}}{dy} &= H_0 \mathbf{A}, \\
 A_1 &= A_3 = A_5 = A_7 = 0, \quad y = 0, \\
 \mathbf{A} &\rightarrow 0, \quad y \rightarrow \infty.
 \end{aligned} \tag{2.3}$$

Store the eigenvalue $\alpha=A$, and the parameters $\omega=W$, $\beta=B$ and R in the common block

COMMON/SCAL2/A,B,W,R

where A,B,W,R are complex.

2.2.2 Calculate the eigenvector $\mathbf{A}(y)$ of the direct problem (2.3) in the range $0 \leq y \leq y_e$.

2.2.3 Calculate the asymptotic form of $\mathbf{A}(y)$ for $y \geq y_e$

$$\mathbf{A} = \sum_{j=1}^4 \mathbf{A}_0^{(j)} \exp[\lambda_j(y - y_e)], \tag{2.4}$$

where $\text{Re}(\lambda_j) < 0$.

2.2.4 Solve the adjoint problem using α , β and ω of the direct problem (2.3)

$$\begin{aligned} \frac{d\mathbf{B}}{dy} &= -H_0^T \mathbf{B}, \\ B_2 &= B_4 = B_6 = B_8 = 0, \quad y = 0, \\ \mathbf{B} &\rightarrow 0, \quad y \rightarrow \infty. \end{aligned} \quad (2.5)$$

2.2.5 Calculate the eigenvector \mathbf{B} in the range $0 \leq y \leq y_e$.

2.2.6 Calculate the asymptotic form of \mathbf{B} for $y \geq y_e$

$$\mathbf{B} = \sum_{j=1}^4 \mathbf{B}_0^{(j)} \exp[\lambda_j(y - y_e)]. \quad (2.6)$$

2.2.7 Store solutions of the direct and adjoint problems in the common block

COMMON/SCAL1/ YZ,Z,DZ,Z0,DZ0,LZ,LDZ,SC,NZ,MF,L

where

YZ(K)= y (real), K=1,...,NZ, is vector of grid points;

Z(I,K)= \mathbf{A} (complex), I=1,...,8 is component number, K=1,...,NZ;

DZ(I,K)= \mathbf{B} (complex), I=1,...,8 is component number, K=1,...,NZ;

Z0(I,J)= $\mathbf{A}_0^{(j)}$ (complex), I=1,...,8, J=1,...,4 ;

DZ0(I,J)= $\mathbf{B}_0^{(j)}$ (complex), I=1,...,8, J=1,...,4 ;

LZ=LDZ= λ_j (complex), J=1,...,4;

NZ – (integer) is number of grid points in the range $0 \leq y \leq y_e$ for the eigenvectors Z and DZ;

SC (complex), MF (integer) and L (integer) are additional parameters, which are not specified by the user.

2.2.8 Calculate the derivative $\text{DADX1} = \frac{\partial \alpha}{\partial x_1}(x_{10})$. This can be done by solving the direct problem (2.3) at two close stations $x_1 = x_{10} - \Delta x_1$ and $x_1 = x_{10} + \Delta x_1$. Then

$$\frac{\partial \alpha}{\partial x_1}(x_{10}) = \frac{\alpha(x_{10} + \Delta x_1) - \alpha(x_{10} - \Delta x_1)}{2\Delta x_1}. \quad (2.7)$$

The parameter DADX1 (complex) is a formal parameter of RECEPT.

2.3 Solution for external wave

Hereafter, we discuss the case when the external disturbance is an acoustic wave. The replacement of acoustic wave by vortical or entropy wave is straightforward.

2.3.1 Solve the local problem for the acoustic wave of the wave numbers α_a , β_a and frequency ω (this frequency=frequency of the direct and adjoint problems of Section 2.2) at the station $x_1 = x_{10}$

$$\begin{aligned} \frac{d\mathbf{A}_a}{dy} &= H_0 \mathbf{A}_a, \\ A_{a1} &= A_{a3} = A_{a5} = A_{a7} = 0, \quad y = 0, \\ \text{external conditions at the upper boundary } y &= y_e. \end{aligned} \tag{2.8}$$

The external condition may be different. For example: (the pressure amplitude of incident acoustic wave at $y = y_e$)=1.

2.3.2 Calculate the external-disturbance vector $\mathbf{A}_a(y)$ in the range $0 \leq y \leq y_e$

2.3.3 Calculate the asymptotic form of $\mathbf{A}_a(y)$ for $y \geq y_e$

$$\mathbf{A}_a = \sum_{j=1}^5 \mathbf{A}_{a0}^{(j)} \exp(\lambda_{aj}(y - y_e)), \tag{2.9}$$

where $\text{Re}(\lambda_{aj}) \leq 0$. Note that the external-disturbance vector is a sum of five vectors. Three of them exponentially decay as $y \rightarrow \infty$. Two others, with $\text{Re}(\lambda_a) = 0$, oscillate outside the boundary layer without damping. They represent an external disturbance outside the boundary layer. For the acoustic disturbance, the oscillatory components represent the incident and reflected waves.

2.3.4 Store characteristics of the external disturbance in the common block

COMMON/SCALA/ YA,ZA,ZA0,LA,AAK,BAK,NA

where

YA(K)= y (real), K=1,...,NA, is vector of grid points;

ZA(I,K)= \mathbf{A}_a (complex), I=1,...,8 is component number, K=1,...,NA;

ZA0(I,J)= $\mathbf{A}_{a0}^{(j)}$ (complex), I=1,...,8 is component number, J=1,...,5;

LA= λ_j (complex), J=1,...,5;

AAK= α_a (complex);

BAK= β_a (complex);

NA – (integer) is number of grid points in the range $0 \leq y \leq y_e$ for the vector ZA.

2.4. Solution for stationary disturbance induced by wavy wall

2.4.1 Solve the problem for the stationary disturbance induced by the wavy wall of $\alpha_w = \alpha - \alpha_a$, $\beta_w = \beta - \beta_a$ and $\omega_w = 0$ at the station $x_1 = x_{10}$

$$\begin{aligned} \frac{d\mathbf{F}_w}{dy} &= H_0 \mathbf{F}_w, \\ F_{w1} &= -DU, F_{w5} = -DT, F_{w7} = -DW, y = 0, \\ \mathbf{F}_w &\rightarrow 0, y \rightarrow \infty. \end{aligned} \quad (2.10)$$

2.4.2 Calculate the vector function $\mathbf{F}_w(y)$ in the range $0 \leq y \leq y_e$.

2.4.3 Calculate the asymptotic form of $\mathbf{F}_w(y)$ for $y \geq y_e$

$$\mathbf{F}_w = \sum_{j=1}^4 \mathbf{F}_{w0}^{(j)} \exp[\lambda_{wj}(y - y_e)], \quad (2.11)$$

where $\text{Re}(\lambda_{wj}) < 0$.

2.4.4 Store characteristics of the stationary disturbance in the common block

COMMON/SCALV/ YV,ZV,ZV0,LV,AVV,BVV,NV

where

YV(K)= y (real), K=1,...,NV, is vector of grid points;

ZV(I,K)= \mathbf{F}_w (complex), I=1,...,8 is component number, K=1,...,NV;

ZV0(I,J)= $\mathbf{F}_{w0}^{(j)}$ (complex), I=1,...,8 is component number, J=1,...,4;

LV= λ_{wj} (complex), J=1,...,4;

AVV= α_w (complex);

BVV= β_w (complex);

NV – (integer) is number of grid points in the range $0 \leq y \leq y_e$ for the vector ZV.

2.5 Disturbance field

2.5.1 Specify the disturbance field vector $\mathbf{F}_0(y)$ in the range $0 \leq y \leq y_e$ at the station $x_1 = x_{10}$.

2.5.2 Store the vector $\mathbf{F}_0(y)$ in the common block

COMMON/FIELD/YA0,A0,NA0

where

YA0(K)= y (real), K=1,...,NA0, is vector of grid points;
A0(I,K)= F_0 (complex), I=1,...,8 is component number; K=1,...,NA0;
NA0 – (integer) is number of grid points for the vector A0.

2.6 Options of RECEIPT.FOR

The module includes the subroutine RECEIPT and the auxiliary subroutines and functions:

- Subroutine SCAL (calculations of scalar products)
- Subroutine BASIC (interpolation of mean-flow profiles)
- Function PARAB2 (interpolation of real function)
- Function PARAB3 (interpolation of complex function)
- Function SIM (integration)

Calculations are performed with double precision:

- All real quantities are described as REAL*8
- All complex quantities are describes as COMPLEX*16

The calling line is

CALL **RECEIPT**(ICONTR,IGNOR,Y1,N,DADX1,EPSIL,CC)

Since the major portion of input data are specified in COMMON blocks, the parameter NNY is included in RECEIPT and BASIC to reserve space for vectors. The user needs to specify NNY in these subroutines: **NNY should be larger then NA, NZ, NV and NBAS.**

2.6.1 To calculate the receptivity coefficient (1.12) for external waves interacting with the wavy wall, the user should put **ICONTR=1** and specify the input data of:

- Steps 1.1-1.4 (mean-flow data)
- Steps 2.1-2.8 (solutions of the direct and adjoint problems for particular mode of discrete spectrum, as well as the derivative $DADX1 = \frac{\partial \alpha}{\partial x_1}(x_{10})$ (complex))
- EPSIL= ϵ (real)
- Steps 3.1-3.4 (external wave)
- Steps 4.1-4.4 (stationary disturbance from wavy wall)
- Y1= y_e - upper boundary (real)
- N – number of knots for calculation of the scalar product integrals in the range $0 \leq y \leq y_e$ (integer, odd)

If the linear stability solver does not provide the asymptotic forms (2.4), (2.6) and (2.9), (2.11), then the user should put **IGNOR=1**. In this case, the contribution to the scalar products from the region $y_e < y < \infty$ is ignored. If the upper boundary $y = y_e$ is not large enough, this may lead to significant error in calculations of the receptivity coefficients. To evaluate this error the user should perform calculations at different y_e .

If the asymptotic forms (2.4), (2.6) and (2.9), (2.11) are available, then the user should put **IGNOR=0**. In this case, it is recommended to specify:

- The upper boundary as $Y1=y_e \approx 3\Delta$, where Δ is nondimensional displacement thickness
- The number of knots $N=501$

However, this recommendation is not universal. For different boundary-layer modes and external waves, the optimal y_e may be different. The user needs to check sensitivity of the computational result to $Y1$ and N .

Output of this option is

CC – receptivity coefficient (1.12) (complex)

2.6.2 To calculate the receptivity coefficient (1.22) for external waves interacting with a local hump, the user should put **ICONTR=2** and specify the input data of:

- Steps 1.1-1.4 (mean-flow data)
- Steps 2.1-2.7 (solutions of the direct and adjoint problems for particular mode of discrete spectrum)
- Steps 3.1-3.4 (external wave)
- Steps 4.1-4.4 (stationary disturbance from wavy wall)
- $Y1=y_e$ - upper boundary (real)
- N – number of knots for calculation of the scalar product integrals in the range $0 \leq y \leq y_e$ (integer, odd)

In this case, the formal parameter DADX1 and EPSIL are not used.

If the LST solver does not provide the asymptotic forms (2.4), (2.6), (2.9), (2.11), then the user should put **IGNOR=1** and follow instructions of Item 2.6.1.

Output of this option is

CC - receptivity coefficient (1.22) for external wave plus local hump (complex)

2.6.3 To calculate the weight coefficient of the discrete mode in the disturbance field, the user should put **ICONTR=3** and specify the input data of:

- Steps 1.1-1.4 (mean-flow data)
- Steps 2.1-2.7 (solutions of the direct and adjoint LST problems)
- Steps 5.1-5.2 (disturbance field)
- $Y1=y_e$ - upper boundary (real)
- N – number of knots for calculation of the scalar product integrals in the range $0 \leq y \leq y_e$ (integer, odd)

In this option, the asymptotic forms (2.6), (2.8) and the parameters **DADX1**, **IGNOR** are not used. Contributions to the scalar products from the region $y_e < y < \infty$ are neglected. If the upper boundary $y = y_e$ is not large enough, this may lead to significant error in calculations of the weight coefficient. With this option, the user should perform calculations at different y_e to evaluate the error (see Section 4).

Output of this option is

CC – the weight coefficient (1.26) (complex)

3. How to use the module output?

Using the receptivity coefficient CC and the eigenfunction vector $Z(I,J)$ of discrete mode, the user can calculate the amplitude of any physical quantity. For example, the pressure disturbance on the wall $p(y=0)$ at station $x = x_0$ is calculated as:

$$\text{For wavy wall: } p = h\varepsilon_a \operatorname{Re} [CC \times Z(4,1)] + (c.c) \quad (3.1)$$

$$\text{For local hump: } p = h\varepsilon_a \operatorname{Re} \left[\frac{1}{2\pi} \int_{-\infty}^{+\infty} CC(\beta) \times Z(4,1) \times \rho(\alpha_0, \beta) \times \exp(i\beta z) d\beta \right] \quad (3.2)$$

where $I=4$ corresponds to the pressure component of the vector $Z(I,J)$ (see (1.4)), and $J=1$ corresponds to $y = 0$.

For analysis of hot-wire measurements, the user needs to calculate the mass-flow disturbance, which is expressed as

$$q_m(y) = \left[u(y) + \left(\gamma M^2 p(y) - \frac{\theta(y)}{T(y)} \right) U(y) \right] \frac{1}{T(y)}. \quad (3.3)$$

At the point $y = y_j$ the correspondent quantity is calculated using the components of vector Z as

$$QM(J)=(Z(1,J)+(G*M*M*Z(4,J)-Z(5,J)/T(J))*U(J))/T(J). \quad (3.4)$$

Replacing $Z(4,1)$ by $QM(J)$ in (3.1) and (3.2), the user obtain the mass-flow amplitude of the discrete mode.

Similar relations are used for calculations of the discrete mode amplitude in the disturbance field (the option ICONTR=3).

4. Weight coefficients

The discrete-mode weight coefficient is calculated using RECEPT with the option ICONTR=3. Herein this option is demonstrated by numerical examples.

Consider the mean flow in the boundary layer on a flat plate. This flow is modeled using the self-similar (compressible Blasius) solution, which provides the longitudinal velocity profile $U(y) \equiv U^* / U_e^*$ and the temperature profile $T(y) \equiv T^* / T_e^*$, where the vertical coordinate is $y = y^* / \sqrt{\nu_e^* x^* / U_e^*}$. The mean-flow pressure is constant across the boundary layer, $P \equiv P^* / P_e^* = 1$. The fluid is a perfect gas with Prandtl number $Pr=0.72$ and the specific heat ratio $\gamma = 1.4$; viscosity depends on temperature as $\mu^* = \mu_e^* (T^* / T_e^*)^{0.7}$; the second viscosity is zero. The local Mach number is $M_e = 6$; the plate-surface temperature equals to the temperature of adiabatic wall, $T_w^* = T_{ad}^*$. The profiles $U(y)$ and $T(y)$ are shown in Figs. 1a,b. The boundary-layer edge (at which $U = 0.99$) is approximately $y = 16$ (see the red line in Fig. 1a).

The disturbance field $\mathbf{F}_0(y)$ of the frequency parameter $F = 1.3 \times 10^{-4}$ is specified at the fixed station x^* , which corresponds to the Reynolds number $R = \sqrt{U_e^* x^* / \nu_e^*} = 10^3$. This field contains the acoustic wave of amplitude $\mathbf{F}_a(y)$ and the second mode of amplitude $c_2 \mathbf{F}_2(y)$, where c_2 is the weight coefficient; i.e., the disturbance field distribution is specified as

$$\mathbf{F}_0(y) = \mathbf{F}_a(y) + c_2 \mathbf{F}_2(y). \quad (4.1)$$

The acoustic component $\mathbf{F}_a(y)$ represents 2-D fast acoustic wave of the angle of incidence $\Theta_y = 60^\circ$. Its phase velocity is $C_a \equiv \frac{\omega}{\alpha_a} = 1 + \frac{1}{M_e \cos \Theta_y}$. The second-mode component has the eigenvalue $\alpha_2 = 1.38896E-01 - i9.26306E-04$, which corresponds to 2-D unstable normal wave in the boundary layer.

In our calculations, we:

- Assign c_2 and calculate the disturbance field (4.1)
- Call RECEPT with the option ICONTR=3 and calculate the weight coefficient $c_{2,num}$

- Compare the weight coefficient $c_{2,num}$ predicted by RECEPT with the actual weight coefficient c_2

The calculations are conducted using a uniform grid versus y with 541 grid points. The upper boundary $y_1 \equiv y_e$ of the computational domain $0 \leq y \leq y_1$ is varied in order to investigate the sensitivity of $c_{2,num}$ to y_1 .

Figure 2 shows the pressure distributions $p_r(y)$ of the second mode with $c_2 = 1$ (red line), for the acoustic wave (blue line), and for the disturbance field=(acoustic wave)+(second mode) (black line). This example corresponds to the upper boundary $y_1 \approx 42$. The weigh coefficient predicted by the module RECEPT is $c_{2,num} = 1.00916$. With this coefficient, the second-mode eigenfunction extracted from the disturbance field (red circles) practically coincides with the actual second-mode component (red line).

Figure 3 shows the numerical weigh coefficient $c_{2,num}$ as a function of the actual weight coefficient c_2 for various upper boundaries y_1 . As c_2 decreases, the curve $c_{2,num}(c_2)$ deviates from the bisectrix $c_{2,num} = c_2$ that indicates the computational error. For the upper boundary $y_1 = 30 \approx 2\Delta$ (where $\Delta=16$ is the boundary-layer thickness), the error is $\sim 2 \times 10^{-2}$. It quickly decreases with y_1 and attains its minimal quantity $\sim 5 \times 10^{-4}$ at $y_1 \approx 70 \approx 4.4\Delta$ (blue line). This trend is due to the fact that the theoretical weight coefficient (1.26) is the ratio of scalar products, which are integrals over the half-infinite interval $0 \leq y < \infty$. However, in calculations of the weight coefficient the integration is performed over the finite interval $0 \leq y < y_1$; i.e., the exponentially decaying tail of the integrant is ignored. This leads to the computational error, which decreases as the upper boundary of computational domain increases.

Further increase of y_1 leads to the increase of computational error that is illustrated in Fig. 3 by the magenta line for $y_1 = 90$. The minimal error depends on accuracy of the mean-flow profiles and eigenfunctions, which are used in calculations of the scalar products.

To verify robustness of the module RECEPT for 3-D disturbances, we calculated the weight coefficient for the disturbance field comprising:

- The fast acoustic wave of the angle of incidence $\Theta_y = 30^\circ$ and various sweep angles $0^\circ \leq \Theta_z \leq 40^\circ$. Its phase velocity is $C_a \equiv \frac{\omega}{\alpha_a} = 1 + \frac{1}{M_e \cos \Theta_y \cos \Theta_z}$, and the z-component of wavenumber is $\beta_a = \alpha_a \tan \Theta_z$
- The 3-D second-mode wave with $\beta_2 = \beta_a$ and the weight coefficient $c_2 = 1$

The disturbance frequency parameter is $F = 1.3 \times 10^{-4}$; the Reynolds number $R = \sqrt{U_e^* x^*} / \nu_e^* = 10^3$. The computational grid contains 501 equally spaced knots with the upper boundary $y_1 = 50$.

The real and imaginary parts of the normal-wave eigenvalue $\alpha_2(\Theta_z)$ are shown in Figs. 4a,b. The growth rate $-\alpha_{2,i}$ is maximal at $\Theta_z = 0$ that is typical for the second mode. Figure 5 compares the actual weight coefficient (black line) with the weigh coefficient $c_{2,num}$ predicted by the RECEPT (red line). The computational error is smaller than 0.5% at $\Theta_z = 0$ and decreases with the sweep angle.

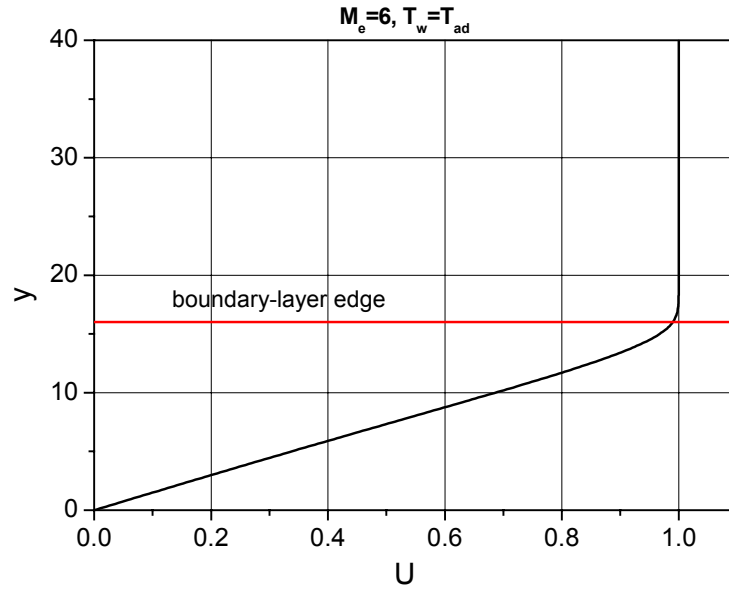


Fig. 1a. Mean-flow velocity profile; $M_e = 6$, $T_w = T_{ad}$.

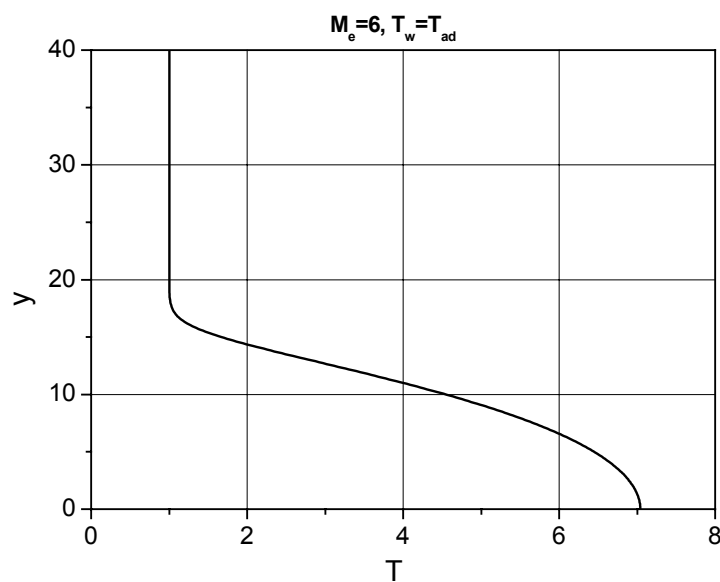


Fig. 1b. Mean-flow temperature profile; $M_e = 6$, $T_w = T_{ad}$.

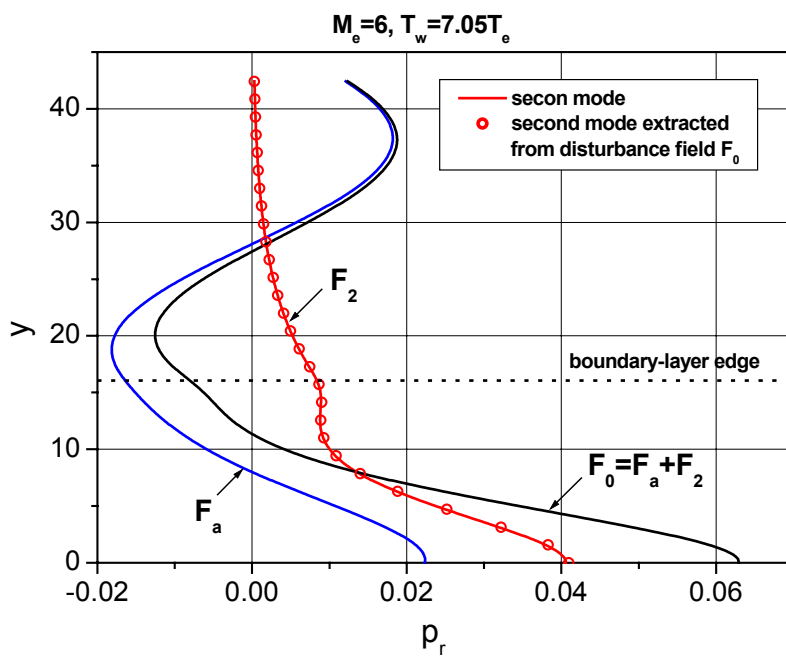


Fig. 2. The real part of pressure distributions for acoustic wave $\mathbf{F}_a(y)$, the second mode $\mathbf{F}_2(y)$, and the disturbance field $\mathbf{F}_0(y) = \mathbf{F}_a(y) + \mathbf{F}_2(y)$; $R = 10^3$, $F = 1.3 \times 10^{-4}$.

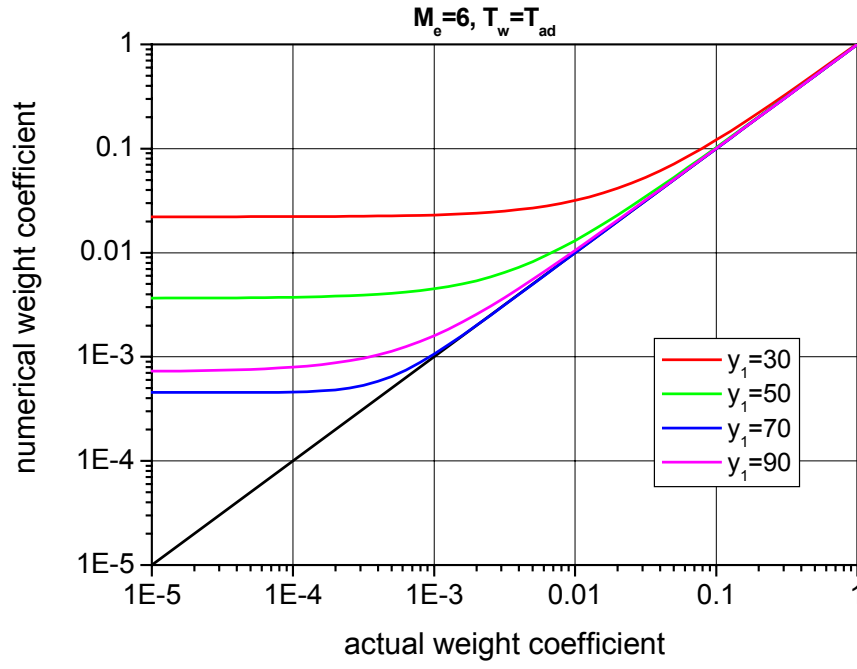


Fig. 3. The weight coefficients predicted by RECEPT at various upper boundaries y_1 .

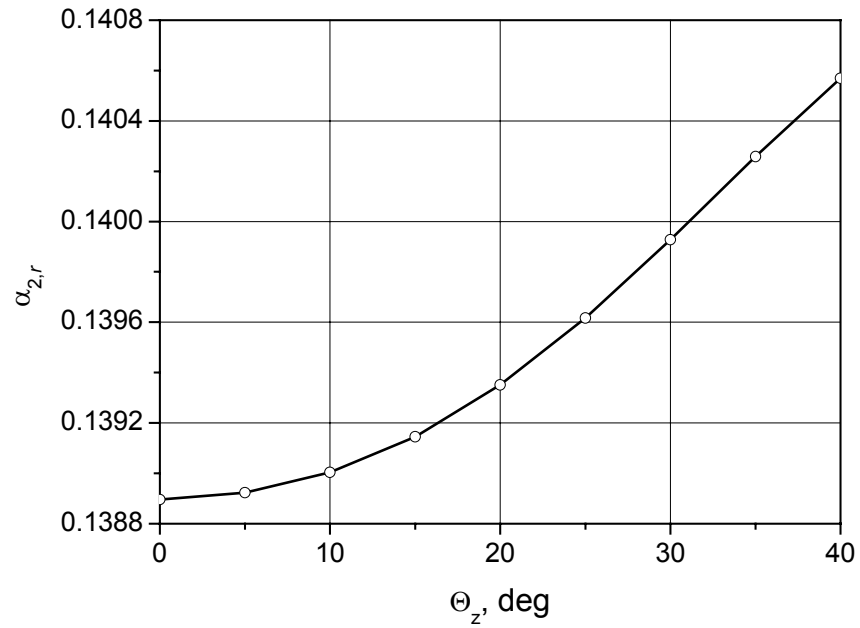


Fig. 4a. Real part of the second-mode eigenvalue α_2 as a function of the sweep angle Θ_z ; $M_e = 6$, $T_w = T_{ad}$, $R = 10^3$, $F = 1.3 \times 10^{-4}$.

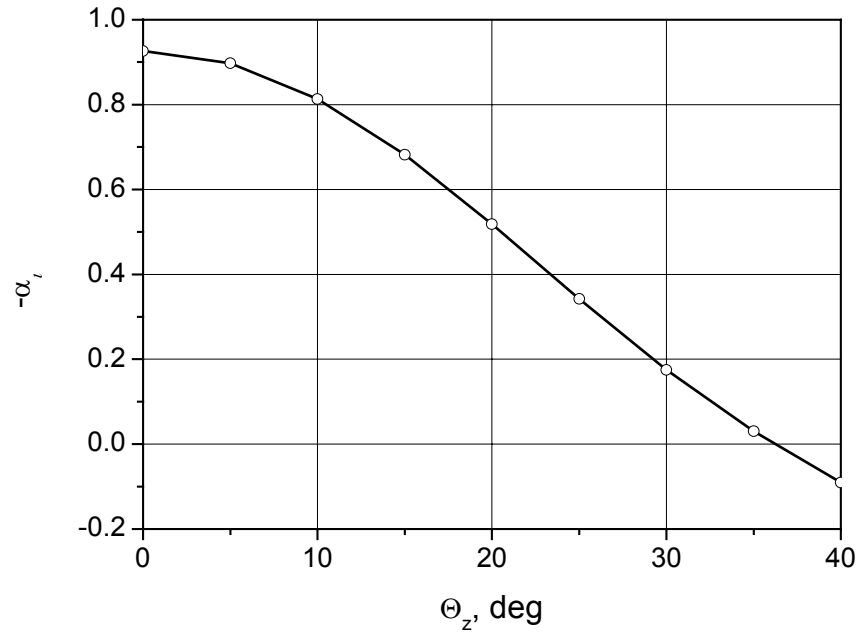


Fig. 4b. Imaginary part of the second-mode eigenvalue α_2 as a function of the sweep angle Θ_z ; $M_e = 6$, $T_w = T_{ad}$, $R = 10^3$, $F = 1.3 \times 10^{-4}$.

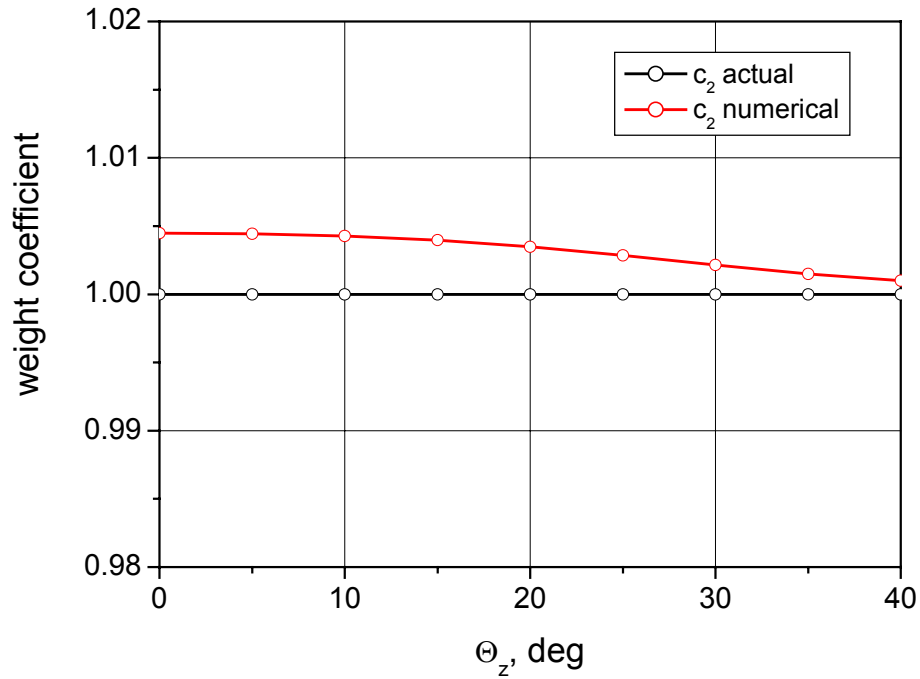


Fig. 5. The weight coefficient of the second mode predicted by the RECEPT for various sweep angles Θ_z ; $M_e = 6$, $T_w = T_{ad}$, $R = 10^3$, $F = 1.3 \times 10^{-4}$.

5. Receptivity coefficients for 2-D second mode generated by 3-D acoustic waves interacting with local 3-D roughness element

5.1 Problem formulation and basic relations

Consider the boundary layer on a flat plate radiated by 3-D acoustic wave as schematically shown in Fig. 6. The longitudinal x^* , normal y^* , transversal z^* coordinates and time t^* are made nondimensional using the boundary-layer length scale $\delta^* = \sqrt{\nu_e^* x^* / U_e^*}$ and U_e^* as $(x, y, z) = (x^*, y^*, z^*) / \delta^*$, $t = t^* U_e^* / \delta^*$. With the assumptions that the wall temperature is constant and the interaction of the boundary layer with the inviscid flow is weak, the nondimensional mean-flow velocity U , temperature T , and pressure P are approximated by the compressible Blasius profiles

$$U \equiv U^* / U_e^* = U(\eta), \quad T \equiv T^* / T_e^* = T(\eta), \quad P \equiv P^* / P_e^* = 1, \quad (5.1)$$

where $\eta = y^* / \sqrt{\nu_e^* x^* / U_e^*}$.

At the distance x_0^* from the leading edge, there is 3-D local roughness element of the shape

$$y_w^*(x^*, z^*) = h^* \delta(x^* - x_0^*) \delta(z^* - z_0^*), \quad (5.2)$$

where δ is Dirac delta function, h^* is roughness height.

A three-dimensional external acoustic wave of the angular frequency $\omega = \omega^* \delta^* / U_e^*$ and wave-numbers $\alpha_a = \alpha_a^* \delta^*$, $\beta_a = \beta_a^* \delta^*$ incidents upon the plate as shown in Fig. 6. The nondimensional pressure of the incident wave is expressed as

$$p = \varepsilon_a \exp(i\alpha_a x + i\beta_a z + ik_{a,inc} y - i\omega t) + (c.c). \quad (5.3)$$

where ε_a is acoustic-pressure amplitude. The vertical wave-number component, $k_{a,inc}$, is determined from the acoustic dispersion relation $k_{a,inc} = k_{a,inc}(\alpha_a, \omega, M)$, where $k_a = \sqrt{(M^2 - 1)(\alpha_a - \alpha_1)(\alpha_a - \alpha_2)}$, $\text{Re}(k_a) > 0$. For β_a real and fixed, the branch points $\alpha_{1,2}$ of the function $k_a(\alpha)$ correspond to slow and fast acoustic waves with the wave front being perpendicular to the wall; i.e., the angle of incidence is $\Theta_y \equiv \tan^{-1}(k_a / \alpha_a) = 0$, whereas the inclination angle is $\Theta_z \equiv \tan^{-1}(\beta_a / \alpha_a)$ with $k_a(\alpha_{1,2}) = 0$. The wave numbers $\alpha_{1,2}$ and the correspondent phase speeds $C_{1,2} = \omega / \alpha_{1,2}$ can be written in terms of Θ_z

$$\alpha_{1,2} = \frac{\omega M \cos \Theta_z}{M \cos \Theta_z \mp 1}, \quad C_{1,2} = 1 \mp \frac{1}{M \cos \Theta_z}. \quad (5.4)$$

Hereafter we assume that $M \cos \Theta_z > 1$. The ranges $\alpha_a > \alpha_1$ and $\alpha_a < \alpha_2$ are relevant to slow and fast acoustic waves with non-zero angle Θ_y ; the wave-numbers of these ranges are expressed as

$$\alpha_a = \frac{\omega M \cos \Theta_z \cos \Theta_y}{M \cos \Theta_z \cos \Theta_y \mp 1}, \quad (5.5)$$

where minus (plus) corresponds to slow (fast) acoustic waves.

The incident acoustic wave interacts with the roughness element and excites boundary-layer modes of frequency ω . Hereafter we focus on excitation of 2-D second mode, which is dominant instability at sufficiently high Mach numbers. This mode is given by the vector-function

$$\mathbf{\Psi}_2(x, y, z, t) = \mathbf{F}_2(x, y, z) \exp(-i\omega t) + (c.c.). \quad (5.6)$$

Downstream from the roughness element, $x > x_0$, the second-mode amplitude is expressed as

$$\mathbf{F}_2 = h\varepsilon_a c(x_0) \mathbf{A}_2(x, y) \exp(iS_2), \quad S_2 = \int_{x_0}^x \alpha_2(x, \omega) dx, \quad \alpha_2 = \alpha_2(x, \omega), \quad (5.7)$$

where $h = h^* / \delta^*$, \mathbf{A}_2 is eigenfunction normalized by the condition $A_{24}(x, 0) = 1$ (the pressure amplitude on the plate surface is $h\varepsilon_a c$); c is the receptivity coefficient, which depends on the roughness element locus x_0 and parameters of the acoustic wave. Using the similarity variables R, η we can express the disturbance amplitude in the form

$$\mathbf{F}_2 = h\varepsilon_a c(R_0) \mathbf{A}_2(R, \eta) \exp(iS_2), \quad S_2 = 2 \int_{R_0}^R \alpha_2(R, \omega) dR; \quad R > R_0. \quad (5.8)$$

As shown in Section 1 the receptivity coefficient is expressed as

$$c(R_0) = q\rho(\alpha_{w0}, \beta_w), \quad (5.9)$$

where q is given by Eq. (1.14). The roughness-shape Fourier transform $\rho(\alpha_w, \beta_w)$ is given by Eq. (1.17). For the roughness shape (5.1), we have

$$\rho(\alpha_w, \beta_w) = \int_{-\infty}^{+\infty} dz' \int_{-\infty}^{+\infty} dx' \delta(x') \delta(z') \exp(-i\alpha_w x' - i\beta_w z') = 1, \quad (5.10)$$

where $x' = x - x_0$, $z' = z - z_0$ are local coordinates. The wave-numbers α_{w0}, β_w satisfy the resonance conditions (1.23), which for 2-D second mode with $\beta = 0$ are expressed as

$$\alpha_{w0} = \alpha_2(x_0, \omega) - \alpha_a, \quad \beta_w + \beta_a = 0. \quad (5.11)$$

Substituting (5.10) into (5.9) we obtain

$$c(R_0) = q(R_0, \Theta_y, \Theta_z, \omega). \quad (5.12)$$

Using the receptivity coefficient (5.12) we calculate the initial amplitude of the second mode as

$$\mathbf{F}_2(R_0, \eta) = h\varepsilon_a c(R_0) \mathbf{A}_2(R_0, \eta). \quad (5.13)$$

In particular, the initial pressure amplitude on the plate surface is given by

$$p_2(R_0, 0) \equiv F_{24}(R_0, 0) = h\varepsilon_a c(R_0). \quad (5.14)$$

The receptivity coefficients are calculated using the module RECEIPT described in Section 2.

5.2. Numerical results

Consider the case: $M = 6$, Prandtl number $\text{Pr} = 0.72$, specific heat ratio $\gamma = 1.4$, the local temperature $T_e^* = 57.56 \text{ K}$, the wall temperature ratio $T_w \equiv T_w^* / T_e^* = 5.212$. The viscosity-temperature dependency is given by Sutherland formula

$$\mu(T) = \frac{(1 + S)}{(T + S)} T^{3/2}, \quad (5.15)$$

where $S = 110. / T_e^*$ for air temperature measured in Kelvin and $\mu = \mu^* / \mu_e^*$ is nondimensional dynamic viscosity. The ratio of the bulk viscosity to the dynamic viscosity is $\mu_v / \mu = 0.8$ (the corresponding coefficient in the stability equations is $e = \frac{3}{2} \frac{\mu_v}{\mu} = 1.2$). This regime was used in

Ref. [40] for parametric studies of receptivity to 2-D acoustic waves interacting with 2-D roughness (waviness or hump).

The incident acoustic wave is specified at the upper boundary $\eta_{up} = 30\sqrt{2} = 42.426$, which is located at the distance from the wall $\cong 2.5$ of the boundary-layer thickness (see Fig. 7a). The disturbance frequency corresponds to the frequency parameter $F = 8. \times 10^{-5}$, which was considered in Ref. [40] for 2-D case.

The mean flow profiles $U(\eta)$ and $T(\eta)$ are shown in Figs. 7a and 7b. A small positive temperature gradient $dT/d\eta$ on the wall indicates that the plate surface temperature is slightly less than the adiabatic wall temperature.

Distributions of $\text{Re}\alpha_2(R)$, the spatial growth rate $\sigma = -\text{Im}\alpha_2(R)$ and the phase speed $C_2 = \text{Re}(\omega/\alpha_2)$ are shown in Figs. 8a,b,c. The point on the lower neutral branch corresponds to $R = 1000$. The non-monotonic behavior of $C_2(R)$ is associated with the presence of the spectrum branch points in the complex R -plane [21,23,40].

Distributions of the receptivity coefficient modulus $|c(\Theta_y, \Theta_z)|$ for the roughness element loci: $R_0 = 500$ (upstream from the neutral point), $R_0 = 1000$ (at the neutral point) and $R_0 = 1500$ (downstream of the neutral point) are shown in Figs. 9a,b,c for fast acoustic waves. The receptivity coefficient monotonically decreases with the inclination angle Θ_z ; i.e., 2-D acoustic waves interacting with 3-D local roughness element provide maximum excitation of 2-D second mode. On the contrary, the functions $|c(\Theta_y)|$ at $\Theta_z = \text{fixed}$ have maximums. For $\Theta_z = 0$ (2-D acoustic waves), these maximums are:

- $|c| \approx 7. \times 10^{-4}$ at $\Theta_y \approx 42^\circ$ and $R_0 = 500$
- $|c| \approx 10. \times 10^{-4}$ at $\Theta_y \approx 38^\circ$ and $R_0 = 1000$
- $|c| \approx 6. \times 10^{-4}$ at $\Theta_y \approx 48^\circ$ and $R_0 = 1500$

The receptivity coefficient has maximum near the neutral point where the most effective angle of incidence is close to its minimum. However, the receptivity maximums at $R_0 = 500$ and 1500 are wider than that at $R_0 = 1000$. This trend may compensate the maximum in the neutral point vicinity if the incident acoustic waves have broad distributions with respect to angles Θ_y and Θ_z .

Numerical results for slow acoustic waves are shown in Figs. 10a,b,c for the same loci of roughness element. Similar to the case of fast acoustic waves, the receptivity coefficient monotonically decreases with the inclination angle Θ_z and has maximum versus the angle of incidence Θ_y . For 2-D acoustic waves ($\Theta_z = 0$) these maximums are:

- $|c| \approx 14. \times 10^{-4}$ at $\Theta_y \approx 52^\circ$ and $R_0 = 500$
- $|c| \approx 16. \times 10^{-4}$ at $\Theta_y \approx 52^\circ$ and $R_0 = 1000$

- $|c| \approx 22. \times 10^{-4}$ at $\Theta_y \approx 30^\circ$ and $R_0 = 1500$

As contrasted to the case of fast acoustic waves, the receptivity maximum increases downstream, while its width is non-monotonic: it is essentially larger near the neutral point $R_0 = 1000$. Note also that slow acoustic waves are more effective than fast waves: for $R_0 = 1000$, $\max |c(\Theta_y, \Theta_z, \text{slow waves})| \cong 1.6 \max |c(\Theta_y, \Theta_z, \text{fast waves})|$.

Figures 11a,b and 12a,b show that the real and imaginary parts of the receptivity coefficients oscillate versus Θ_y ; i.e., the initial phase of the second-mode strongly depends on the angle of incidence. If acoustic waves are widely distributed with respect to Θ_y , these oscillations may lead to significant reduction of the second-mode initial amplitude.

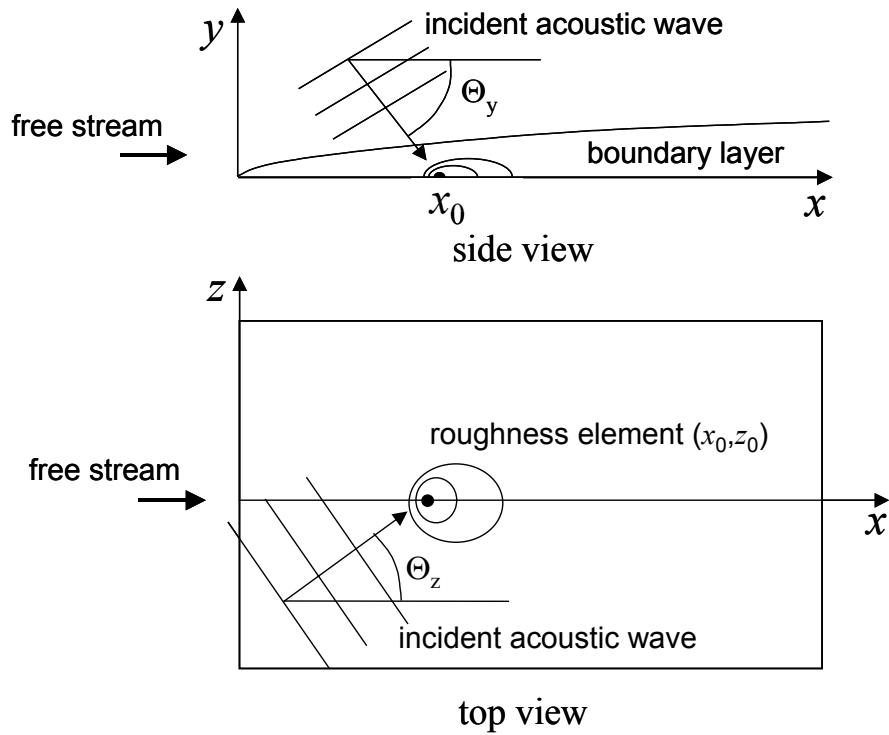


Fig. 6. Schematics of incident acoustic wave interacting with local roughness element.

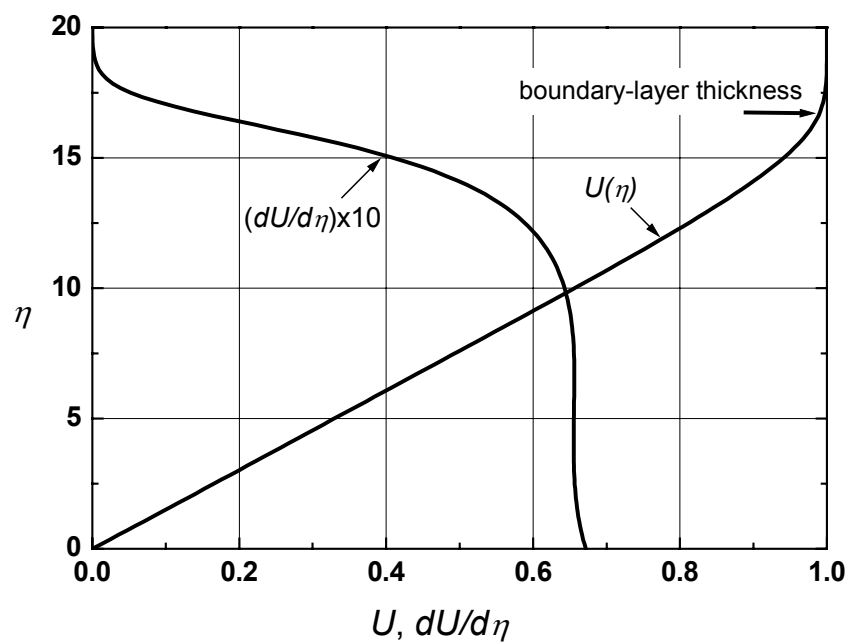


Fig. 7a. Profile of mean-flow velocity.

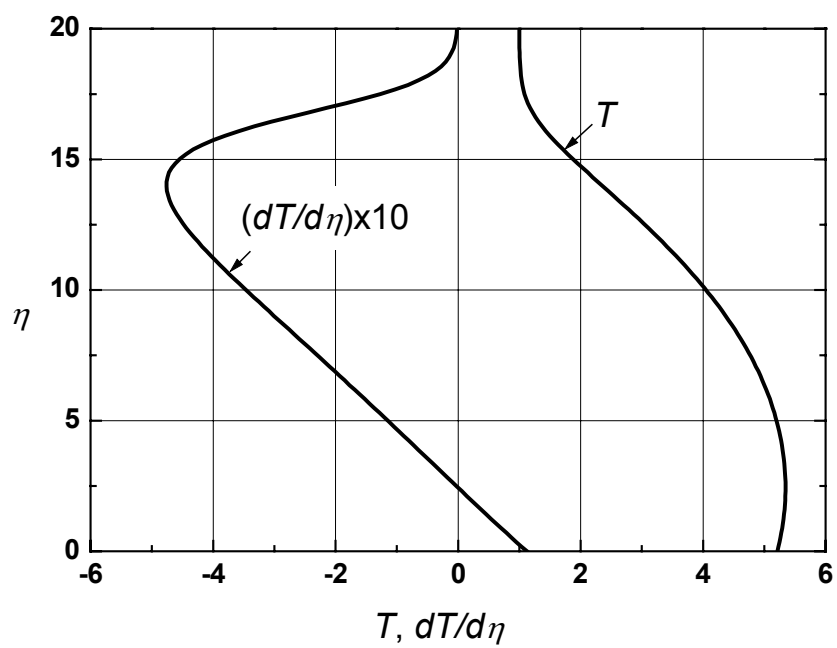


Fig. 7b. Profile of mean-flow temperature.

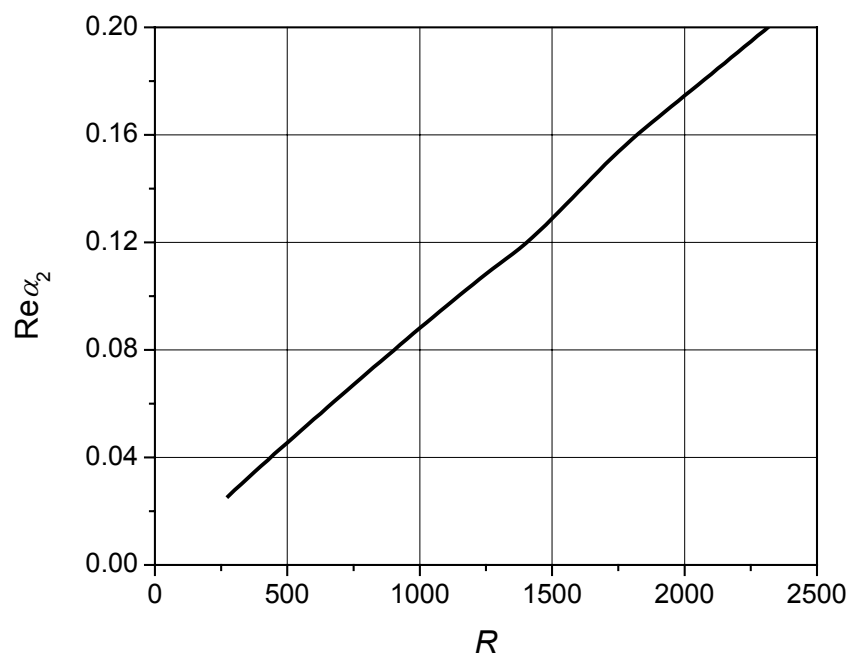


Fig. 8a. The real part of second-mode eigenvalue $\text{Re}\alpha_2$ as a function of Reynolds number R .

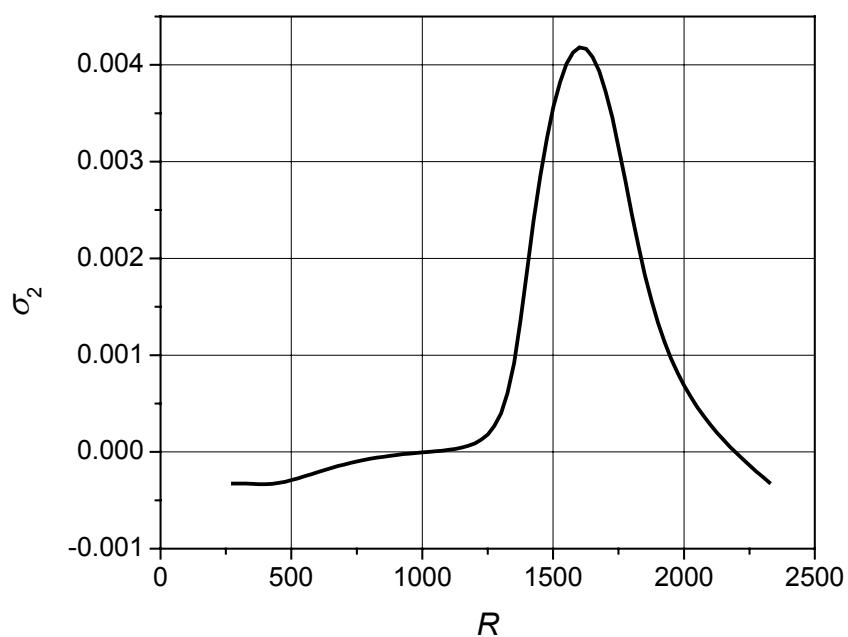


Fig. 8b. The second-mode growth rate $\sigma = -\text{Im}\alpha_2$ as a function of Reynolds number R .

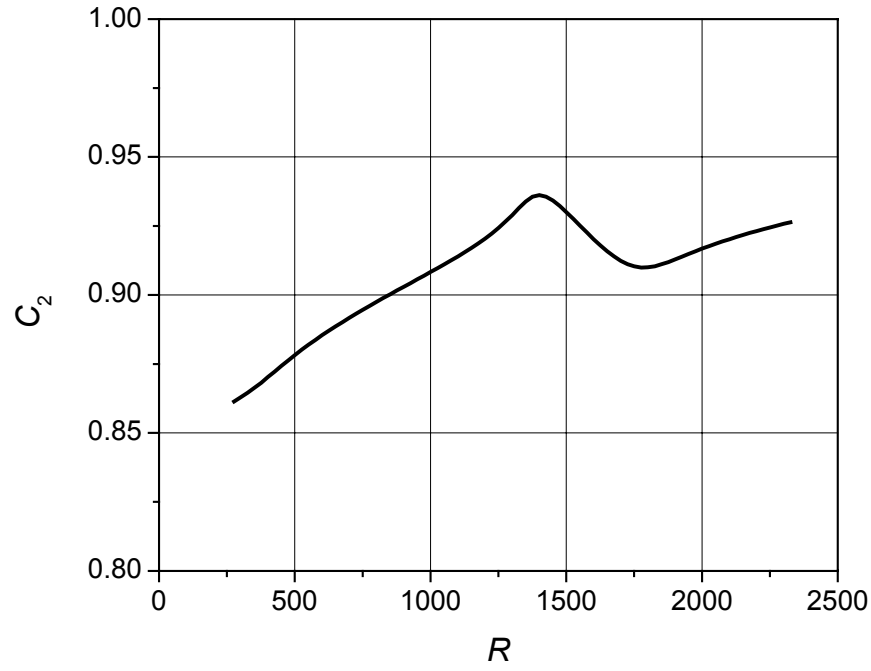


Fig. 8c. The second-mode phase speed $C_2 = \text{Re}(\omega / \alpha_2)$ as a function of Reynolds number R .

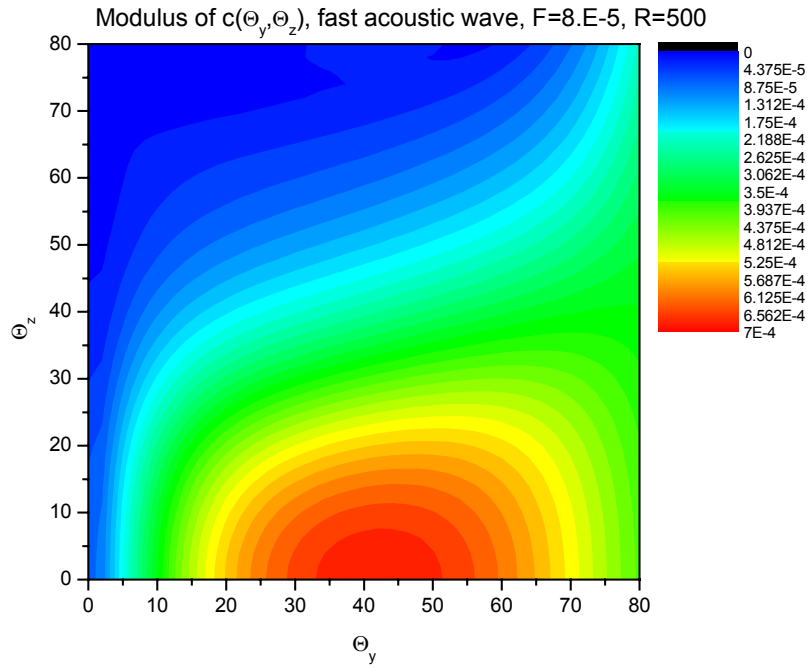


Fig. 9a. The receptivity coefficient modulus $|c(\Theta_y, \Theta_z)|$ at the roughness element locus $R_0 = 500$ (upstream from the neutral point); fast acoustic waves; angles are given in degrees.

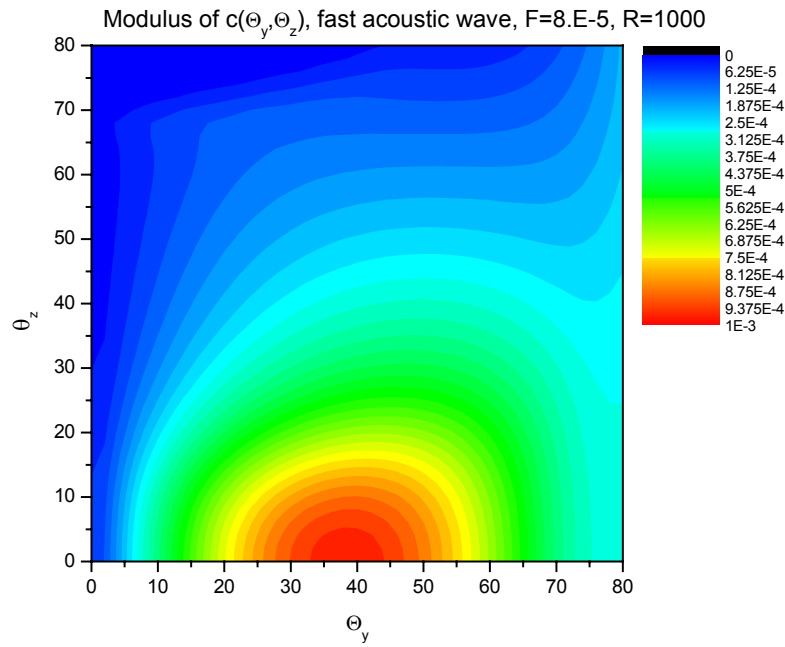


Fig. 9b. The receptivity coefficient modulus $|c(\Theta_y, \Theta_z)|$ at the roughness element locus $R_0 = 1000$ (neutral point); fast acoustic waves; angles are given in degrees.

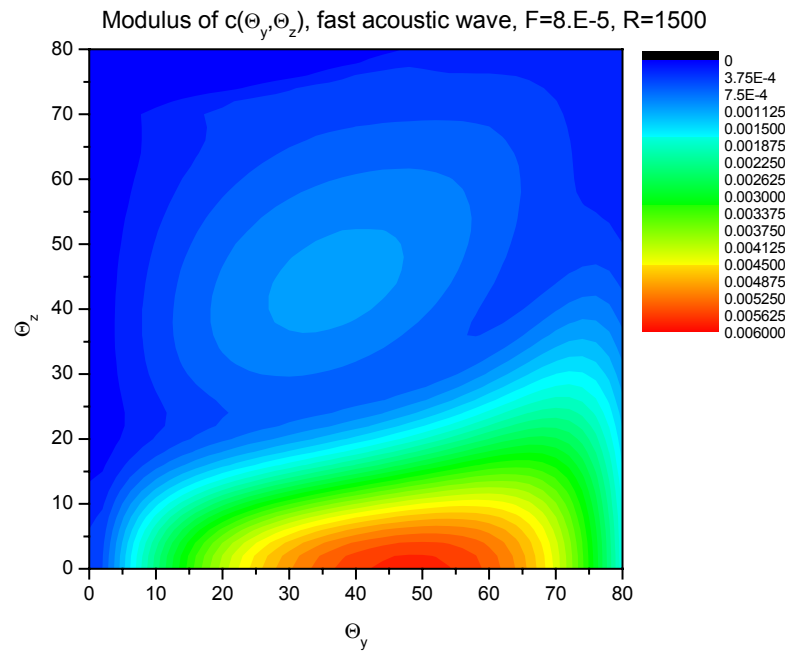


Fig. 9c. The receptivity coefficient modulus $|c(\Theta_y, \Theta_z)|$ at the roughness element locus $R_0 = 1500$ (downstream from the neutral point); fast acoustic waves; angles are given in degrees.

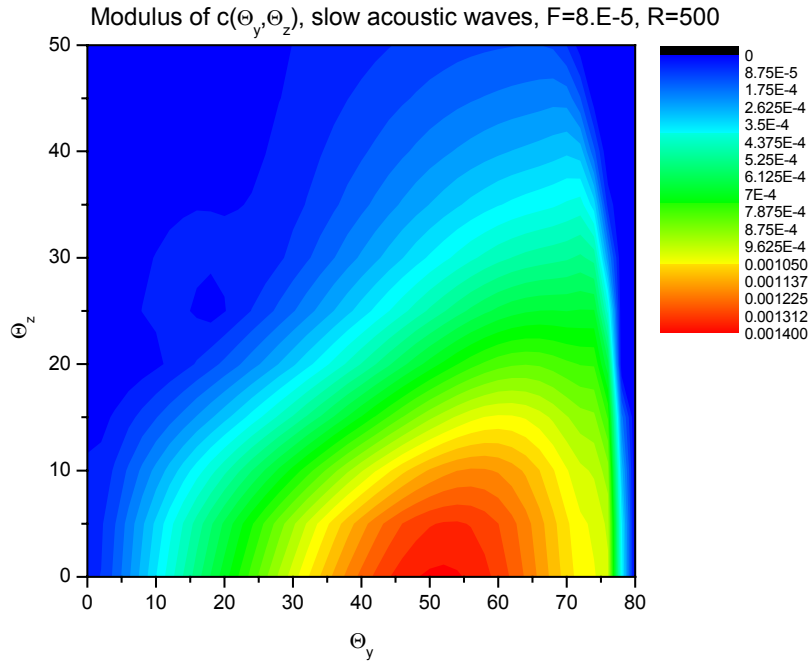


Fig. 10a. The receptivity coefficient modulus $|c(\Theta_y, \Theta_z)|$ at the roughness element locus $R_0 = 500$ (upstream from the neutral point); slow acoustic waves; angles are given in degrees.

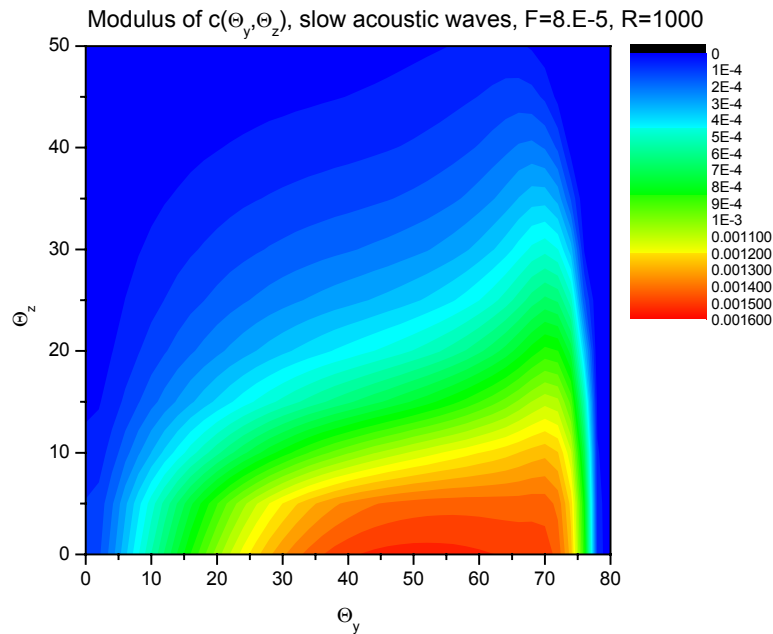


Fig. 10b. The receptivity coefficient modulus $|c(\Theta_y, \Theta_z)|$ at the roughness element locus $R_0 = 1000$ (neutral point); slow acoustic waves; angles are given in degrees.

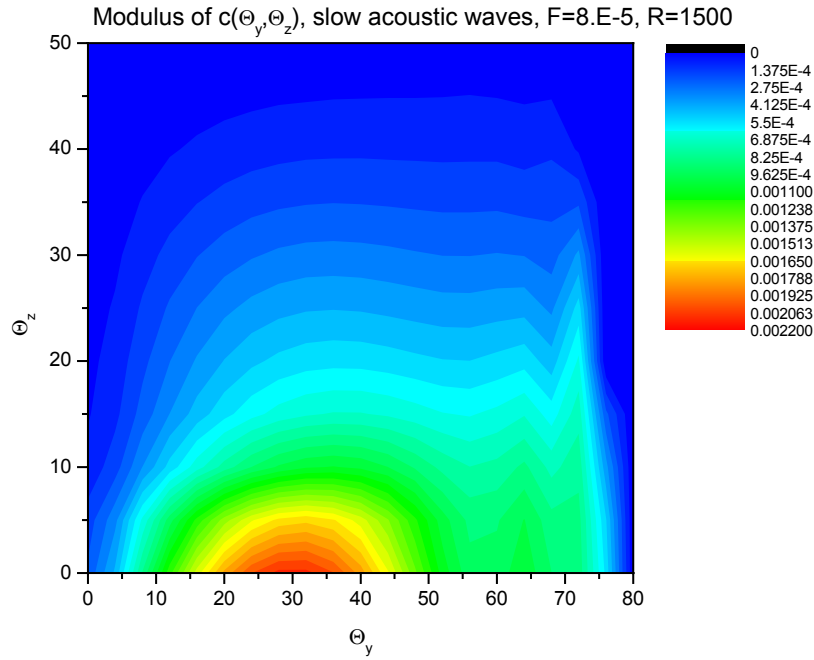


Fig. 10c. The receptivity coefficient modulus $|c(\Theta_y, \Theta_z)|$ at the roughness element locus $R_0 = 1500$ (downstream from the neutral point); slow acoustic waves; angles are given in degrees.

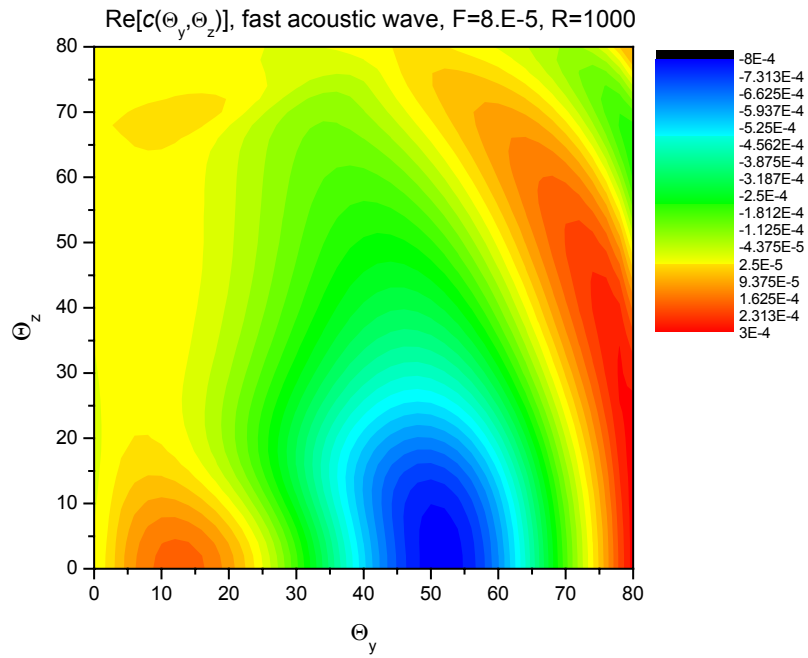


Fig. 11a. The real part of $c(\Theta_y, \Theta_z)$ at the roughness element locus $R_0 = 1000$ (neutral point); fast acoustic waves; angles are given in degrees.

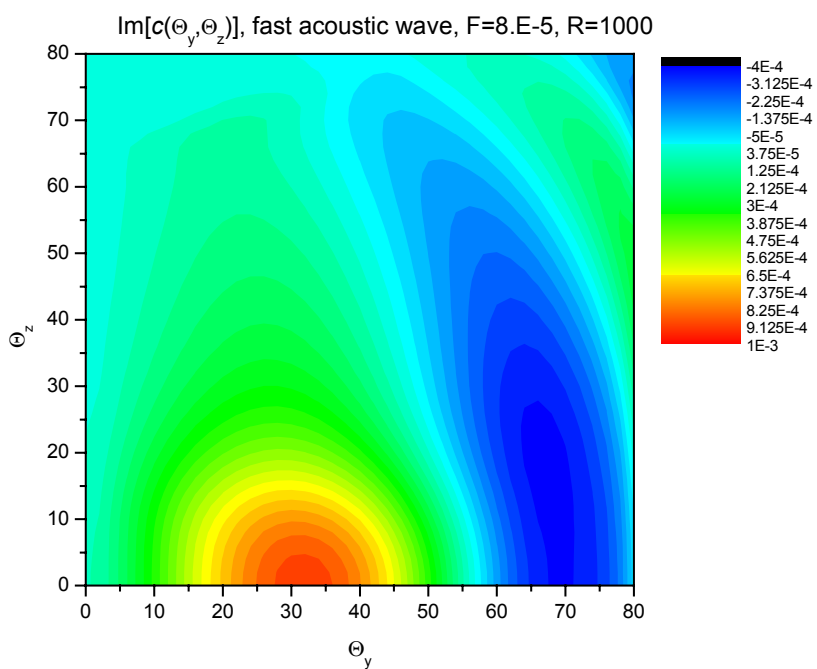


Fig. 11b. The imaginary part of $c(\Theta_y, \Theta_z)$ at the roughness element locus $R_0 = 1000$ (neutral point); fast acoustic waves; angles are given in degrees.

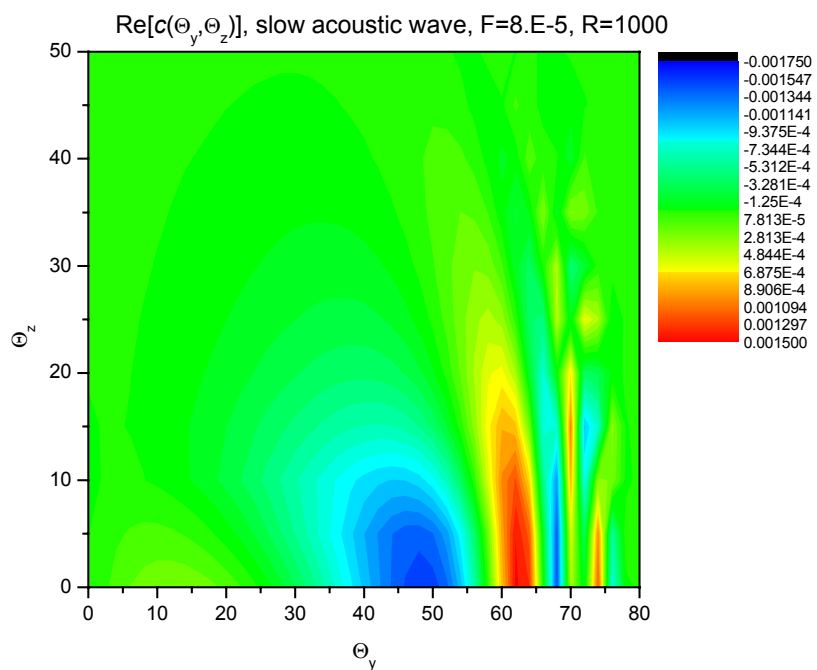


Fig. 12a. The real part of $c(\Theta_y, \Theta_z)$ at the roughness element locus $R_0 = 1000$ (neutral point); slow acoustic waves; angles are given in degrees.

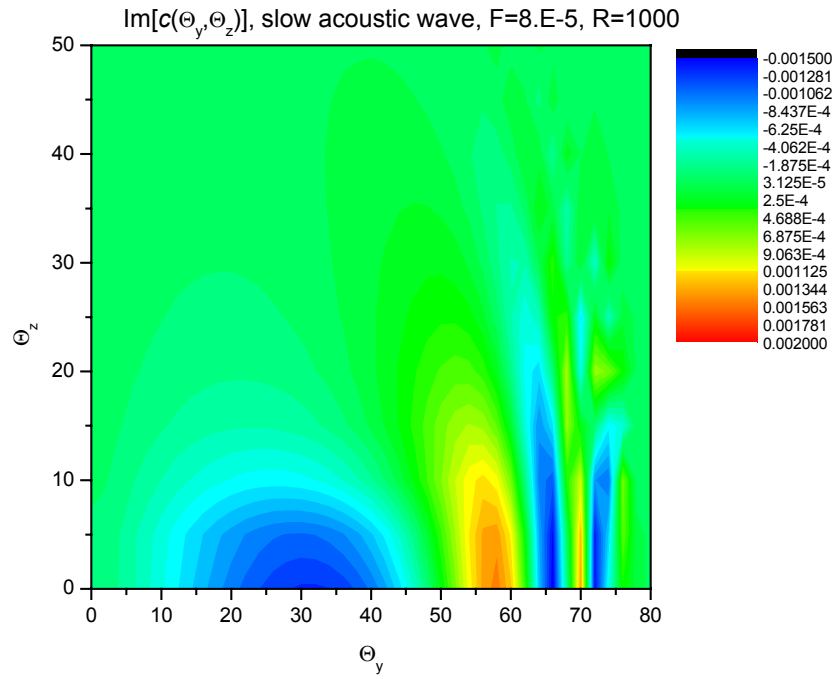


Fig. 12b. The imaginary part of $c(\Theta_y, \Theta_z)$ at the roughness element locus $R_0 = 1000$ (neutral point); slow acoustic waves; angles are given in degrees.

6. Receptivity coefficients for 3-D Tollmien-Schlichting waves generated by acoustic waves interacting with local 3-D roughness element

6.1. Problem formulation and basic relations

The problem is formulated similar to the case of second-mode excitation discussed in Section 5. Consider the boundary layer on a flat plate radiated by 3-D acoustic wave as schematically shown in Fig. 6. The nondimensional mean-flow velocity U , temperature T , and pressure P are approximated by the compressible Blasius profiles (5.1). At the distance x_0^* from the plate leading edge, there is 3-D local roughness element of the shape (5.2). The nondimensional pressure of 3-D incident acoustic wave is given by (5.3). This wave interacts with the roughness-induced disturbance and excites 3-D Tollmien-Schlichting (TS) wave, which is dominant instability at moderate supersonic Mach numbers. This mode is given by the vector-function

$$\Psi_{TS}(x, y, z, t) = \mathbf{F}_{TS}(x, y) \exp(i\beta_{TS}z - i\omega t) + (c.c.). \quad (6.1)$$

Downstream from the roughness element, $x > x_0$, the TS-mode amplitude is expressed as

$$\mathbf{F}_{TS} = h\varepsilon_a c(x_0) \mathbf{A}_{TS}(x, y) \exp(iS_{TS}), \quad S_{TS} = \int_{x_0}^x \alpha_{TS}(x, \omega, \beta) dx, \quad (6.2)$$

where $h = h^* / \delta^*$, \mathbf{A}_{TS} is eigenfunction normalized by the condition $A_{TS4}(x, 0) = 1$. The receptivity coefficient c depends on the roughness element locus x_0 and parameters of the acoustic wave. Using the similarity variables R, η we express the disturbance amplitude in the form

$$\mathbf{F}_{TS} = h\varepsilon_a c(R_0) \mathbf{A}_{TS}(R, \eta) \exp(iS_{TS}), \quad S_{TS} = 2 \int_{R_0}^R \alpha_{TS}(R, \omega, \beta) dR; \quad R > R_0. \quad (6.3)$$

The receptivity coefficient is $c(R_0) = q\rho(\alpha_{w0}, \beta_w)$, where q is given by Eq. (1.14). The roughness-shape Fourier transform $\rho(\alpha_w, \beta_w)$ is given by Eq. (1.17). The wave-numbers α_{w0}, β_w satisfy the resonance conditions (1.23), which for TS-wave are expressed as

$$\alpha_{w0} = \pm(\alpha_{TS}(x_0, \omega, \beta) - \alpha_a), \quad \beta_w = \pm(\beta_{TS} - \beta_a). \quad (6.4)$$

Then the receptivity coefficient is

$$c(R_0) = q_+(R_0, \Theta_y, \Theta_z, \omega) + q_-(R_0, \Theta_y, \Theta_z, \omega), \quad (6.5)$$

where the subscript “ \pm ” corresponds to the \pm component of (6.4). Using (6.5) we calculate the initial amplitude of the TS mode as

$$\mathbf{F}_{TS}(R_0, \eta) = h\varepsilon_a c(R_0) \mathbf{A}_{TS}(R_0, \eta). \quad (6.6)$$

In particular, the initial pressure amplitude on the plate surface is given by

$$p_{TS}(R_0, 0) \equiv F_{TS4}(R_0, 0) = h\varepsilon_a c(R_0). \quad (6.7)$$

The receptivity coefficients are calculated using the module RECEPT described in Section 2.

6.2 Numerical results

Consider the case related to the receptivity experiments of Graziosi and Brown [41]: $M = 2.98$, Prandtl number $Pr = 0.72$, specific heat ratio $\gamma = 1.4$, the stagnation temperature $T_0^* = 278$ K, the plate temperature corresponds to the adiabatic wall, $T_w^* = T_{ad}^*$. The viscosity-temperature dependency is given by Sutherland formula (5.15). The bulk viscosity is assumed to be zero, $\mu_v = 0$. The mean-flow profiles $U(\eta)$ and $T(\eta)$ are shown in Figs. 13a,b. The boundary-layer thickness is approximately $\eta_\delta \approx 9.2$.

The incident acoustic wave is specified at the upper boundary $\eta_{up} = 15\sqrt{2} \approx 21.2$, which is located at the distance from the wall $\cong 2.3$ of the boundary-layer thickness (see Fig. 13a). The disturbance frequency corresponds to the frequency parameter $F = 1.4 \times 10^{-5}$.

Contour plots representing the distributions of $\text{Re } \alpha_{TS}(R, F_\beta)$ and the spatial growth rate $\sigma_{TS} = -\text{Im } \alpha_{TS}(R, F_\beta)$ are shown in Figs. 14a,b, where $F_\beta = \beta^* \nu_e^* / U_e^*$ so that the nondimensional transversal wave-number is $\beta = F_\beta R$. In Fig. 14b, the boundary of colored region represents the neutral curve in the $R - F_\beta$ plane. At $R = 900$ the maximum growth rate is observed at $F_\beta \approx 0.68 \times 10^{-4}$ that corresponds to the TS wave-front angle $\varphi_{TS} = \tan^{-1}(\beta / \text{Re}(\alpha_{TS})) \approx 71^\circ$. Hereafter, the roughness element is located at the station $R = 620$, which is close to the neutral curve tip (see the vertical black line in Fig. 14b).

6.2.1 Fast acoustic waves

Figure 15a shows the receptivity coefficient c as a function of F_β for the fast acoustic wave of the angles $\Theta_y = 45^\circ$ and $\Theta_z = 0$. In the vicinity of $F_\beta = 4.6 \times 10^{-5}$, the imaginary part and modulus of c rapidly drop. A nature of this behavior is clarified in Fig. 15b, where the receptivity coefficient is plotted as a function of the angle φ_w between the z -axis and the wave front of the resonant component of roughness-induced disturbance, $\varphi_w = \tan^{-1}(\beta_w / \alpha_w)$ (see

Fig. 16). The rapid change of receptivity coefficient corresponds to $\varphi_w^{trans} = 70.4^\circ$ (see magenta vertical line in Fig. 15b) at which the wave-front of resonant waviness is directed along the Mach wave. In this case, the freestream velocity component normal to the wave front corresponds to the transonic Mach number $M_n = 1$. For $\varphi_w < \varphi_w^{trans}$, the resonant waviness generates supersonic disturbances outside the boundary layer since $M_n > 1$. For $\varphi_w > \varphi_w^{trans}$, these disturbances are subsonic. Transition from supersonic to subsonic waviness is accompanied by the singular behavior of receptivity coefficient.

Similar trends are observed in the case of 3-D fast acoustic wave with $\Theta_y = 0$ and $\Theta_z = 45^\circ$ (see Figs. 17a,b). For this case, more details on transition through the transonic regime are shown in Figs. 18-20. The waviness-induced disturbance is given by (1.9). Outside the boundary layer, the vector \mathbf{F}_w is represented by the sum of four vectors

$$\mathbf{F}_w = \sum_{j=1}^4 \mathbf{q}_w^{(j)} \exp(\lambda_j y), \quad \text{Re}(\lambda_j) \leq 0, \quad y \rightarrow \infty. \quad (6.8)$$

One of these vectors, say $\mathbf{q}_w^{(1)}$, is relevant to inviscid disturbances of acoustic type; the others are associated with vorticity and entropy waves. The function $\lambda_1(F_\beta)$ is shown in Fig. 18. For supersonic waviness, $\text{Re}(\lambda_1)$ is almost zero and $\text{Im}(\lambda_1) > 0$; i.e., the disturbance oscillates outside the boundary and forms Mach waves. For subsonic waviness, this disturbance exponentially decays. Transition from supersonic to subsonic regime is accompanied by rapid changes of $\lambda_1(F_\beta)$. In the vicinity of the transonic point $F_\beta \approx 5.5 \times 10^{-5}$, where λ_1 is practically zero, the vector-function $\mathbf{F}_w(y)$ varies sharply as shown in Figs. 19, 20.

Figures 15b and 17b show that the modulus of receptivity coefficient in the case of supersonic resonant waviness is significantly larger than in the case of subsonic waviness. This seems to be due to weak penetration of subsonic waviness-induced disturbance into the outer inviscid flow.

Figure 21 shows the contour plot of the receptivity coefficient modulus as a function of the acoustic-wave angles Θ_y and Θ_z . The transversal wave-number parameter of TS wave is fixed, $F_\beta = 6.8 \times 10^{-5}$, and corresponds to TS-wave of maximum downstream growth (see Fig. 14b). For small angles of incidence $\Theta_y < 5^\circ$, the receptivity coefficient has maximum versus Θ_z . At $\Theta_y = 0$ this maximum is close to the inclination angle of TS wave $\varphi_{TS} \approx 71^\circ$. For larger angles of incidence, $|c|$ monotonically increases with Θ_z . For $\Theta_z > 85^\circ$, the function $|c(\Theta_y)|$ has maximum $|c| \approx 9. \times 10^{-4}$ in the vicinity of $\Theta_y \approx 18^\circ$.

6.2.2 Slow acoustic waves

Figures 22a,b show the functions $c(F_\beta)$ and $c(\varphi_w)$ for the slow acoustic wave of $\Theta_y = 45^\circ$ and $\Theta_z = 0$. The receptivity maximum lies in the range of subsonic resonant waviness. Its value, $|c|_{\max} \approx 6.25 \times 10^{-4}$, is close to the receptivity maximum, $|c|_{\max} \approx 6. \times 10^{-4}$, for the fast acoustic

wave of the same angles Θ_y, Θ_z (see Figs. 15a,b). Similar to the case of fast acoustic waves, the receptivity coefficient is singular at $\varphi_w = 70.4^\circ$ corresponding to the transonic resonant waviness.

Figures 23a,b show the functions $c(F_\beta)$ and $c(\varphi_w)$ for the slow acoustic wave of $\Theta_y = 0$ and $\Theta_z = 45^\circ$. In this case, there are two singular points associated with the resonant transonic waviness of $\varphi_w = \mp 70.4^\circ$. In Fig. 24 a contour plot of the receptivity coefficient modulus is shown as a function of Θ_y and Θ_z . As in the case of fast acoustic waves (Fig. 21), the transversal wave-number parameter $F_\beta = 6.8 \times 10^{-5}$ corresponds to TS-wave of maximum downstream growth. The red dashed lines indicate Θ_y and Θ_z at which the resonant waviness is transonic. Between these lines the receptivity coefficient reaches the maximum $|c|_{\max} \approx 2.8 \times 10^3$ at $\Theta_y \approx 52^\circ$ and $\Theta_z \approx 38^\circ$. This maximum is approximately 3 times larger than $|c|_{\max}$ for fast acoustic waves (see Fig. 21).

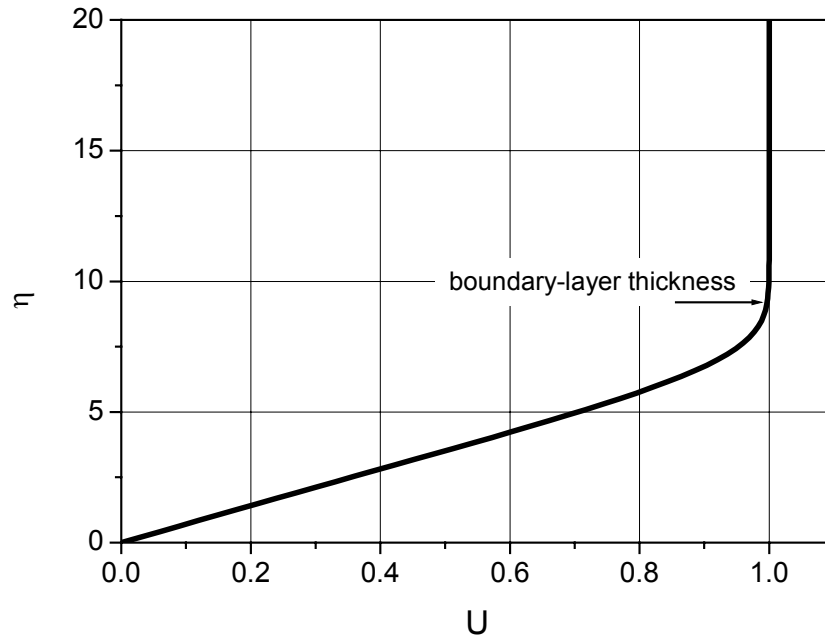


Fig. 13a. Profile of mean-flow velocity, boundary-layer thickness $\eta_\delta \approx 9.2$, $M = 2.98$.

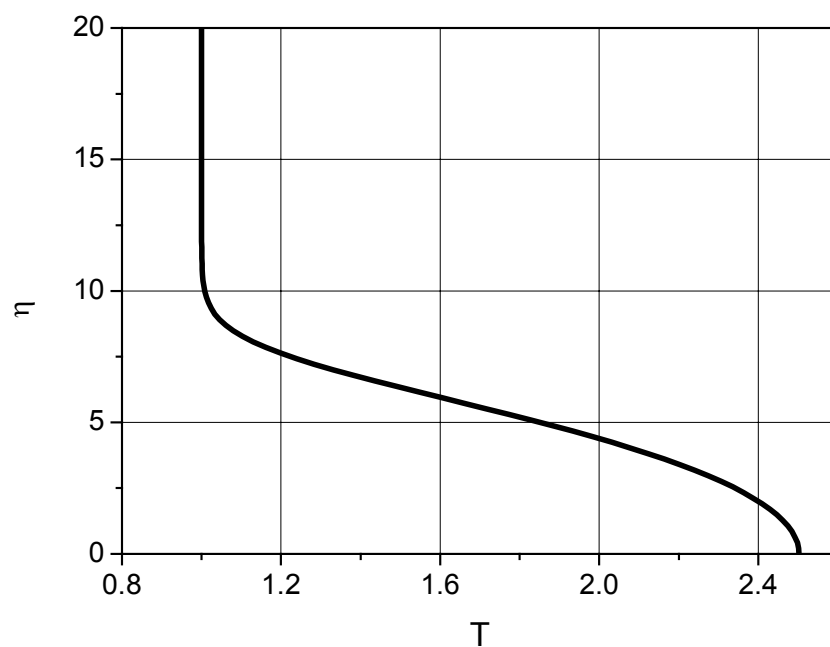


Fig. 13b. Profile of mean-flow temperature on adiabatic plate, $M = 2.98$.

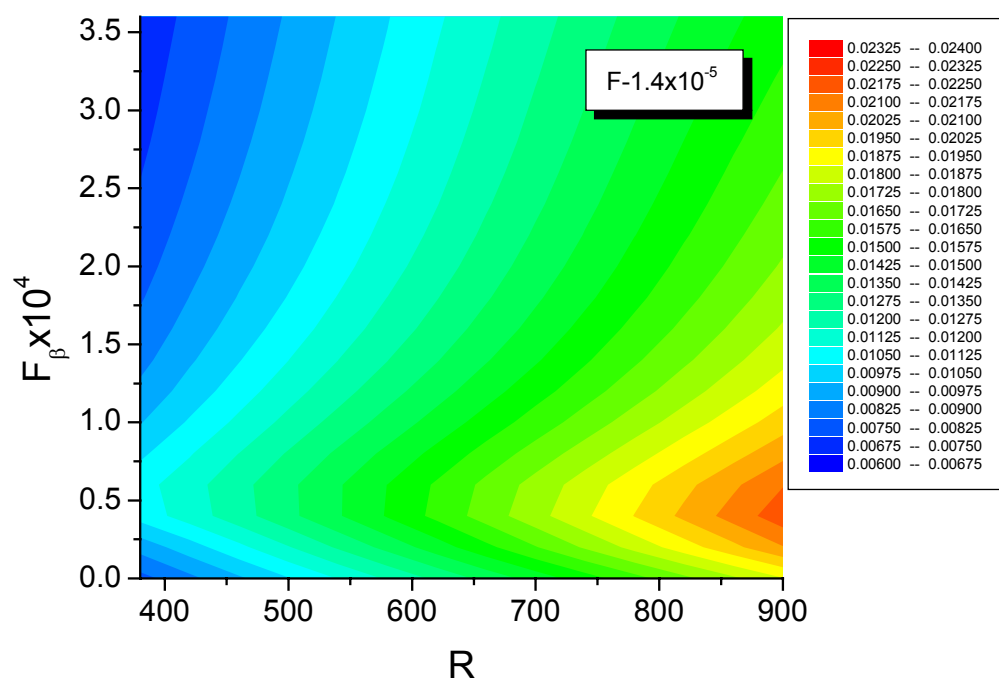


Fig. 14a. The real part of TS eigenvalue $\text{Re } \alpha_{TS}$ as a function of Reynolds number R and F_β .

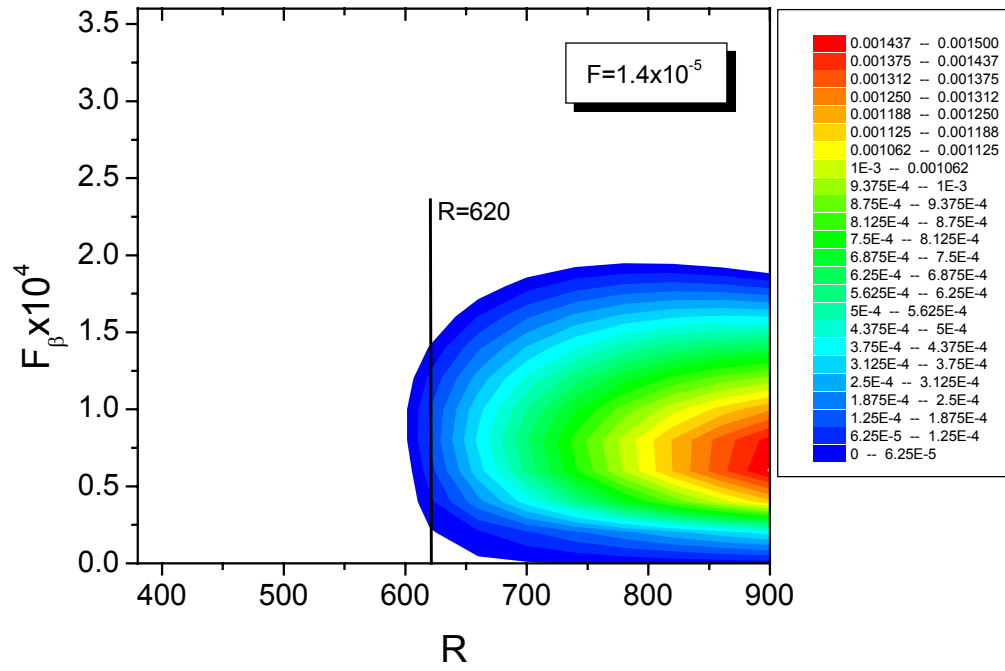


Fig. 14b. The TS growth rate $\sigma_{TS} = -\text{Im } \alpha_{TS}$ as a function of Reynolds number R and F_β .

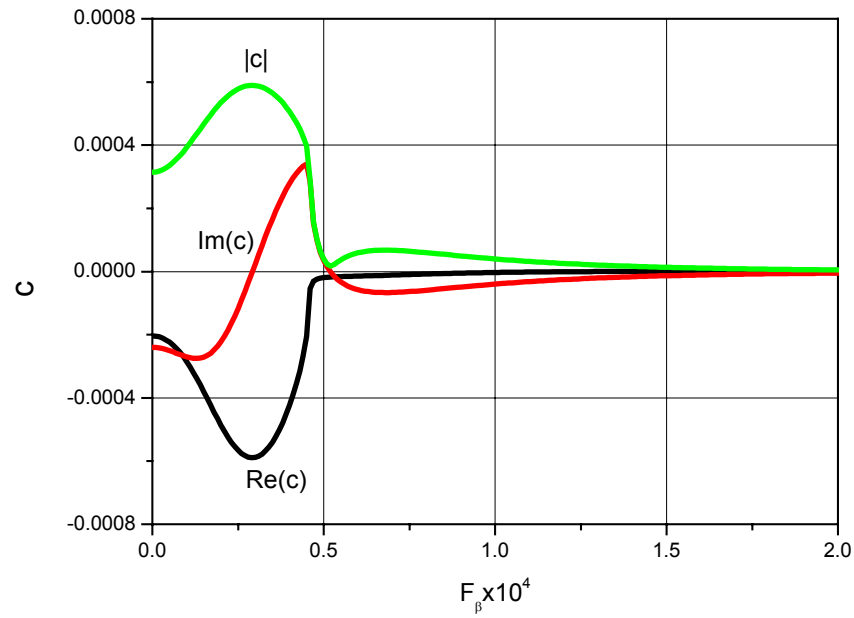


Fig. 15a. Receptivity coefficient as a function of F_β for fast acoustic wave of $\Theta_y = 45^\circ$, $\Theta_z = 0$; $R = 620$, $F = 1.4 \times 10^{-5}$.

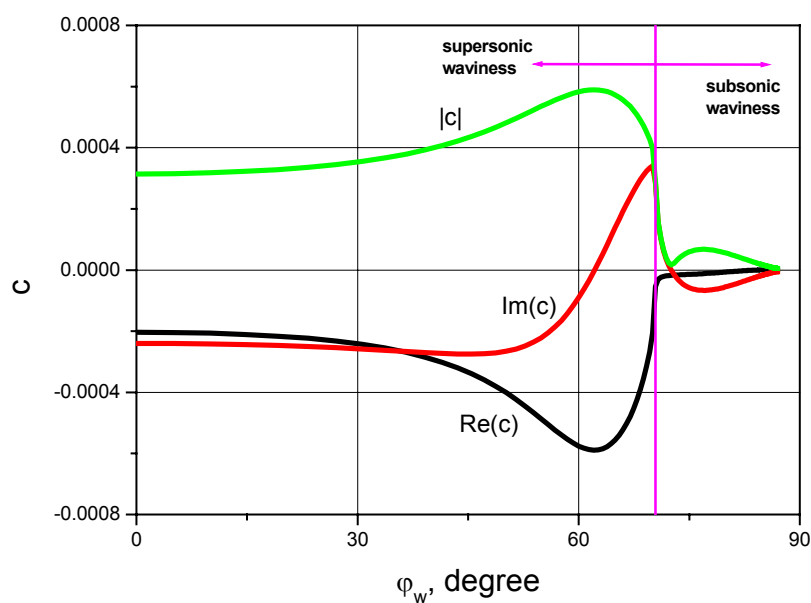


Fig. 15b. Receptivity coefficient as a function of φ_w for fast acoustic wave of $\Theta_y = 45^\circ$, $\Theta_z = 0$; $R = 620$, $F = 1.4 \times 10^{-5}$.

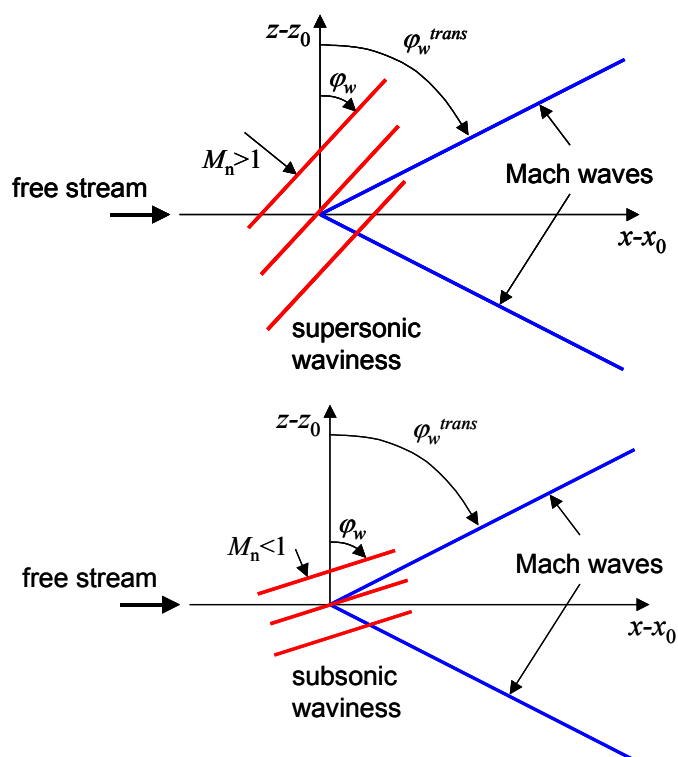


Fig. 16. Orientations of the wave-front of resonant waviness with respect to Mach waves.

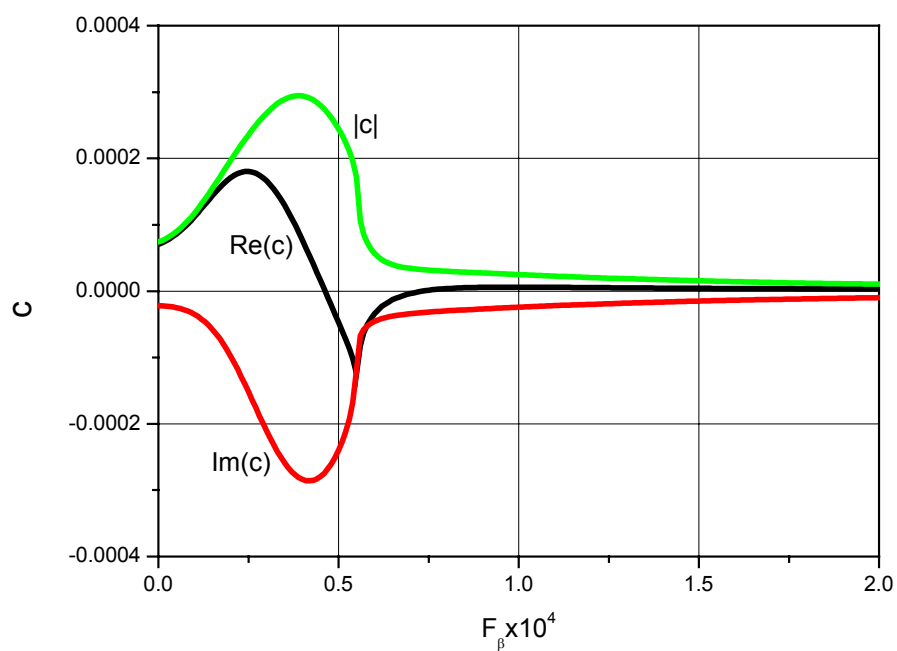


Fig. 17a. Receptivity coefficient as a function of F_β for fast acoustic wave of $\Theta_y = 0$, $\Theta_z = 45^\circ$; $R = 620$, $F = 1.4 \times 10^{-5}$.

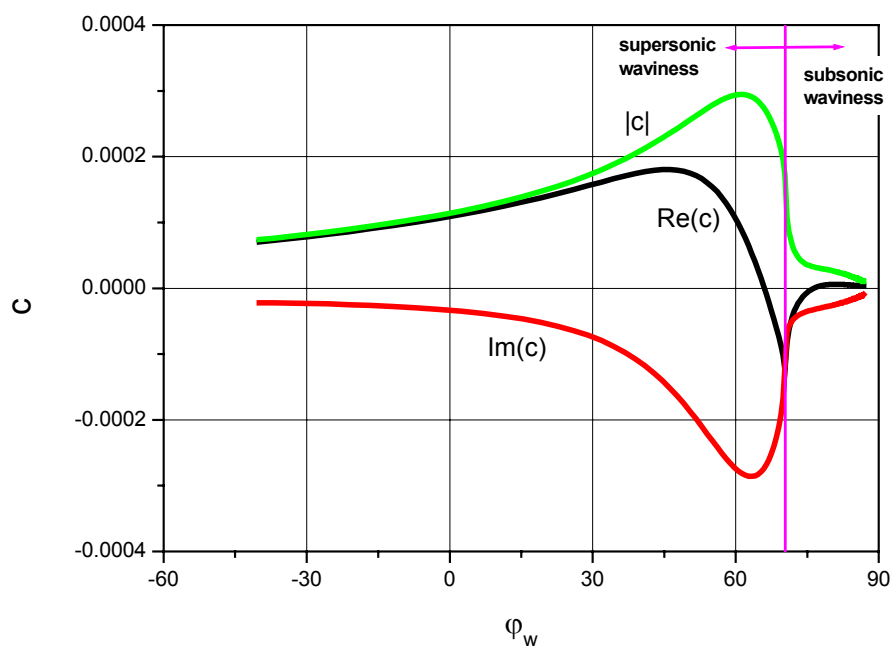


Fig. 17b. Receptivity coefficient as a function of φ_w for fast acoustic wave of $\Theta_y = 0$, $\Theta_z = 45^\circ$; $R = 620$, $F = 1.4 \times 10^{-5}$.

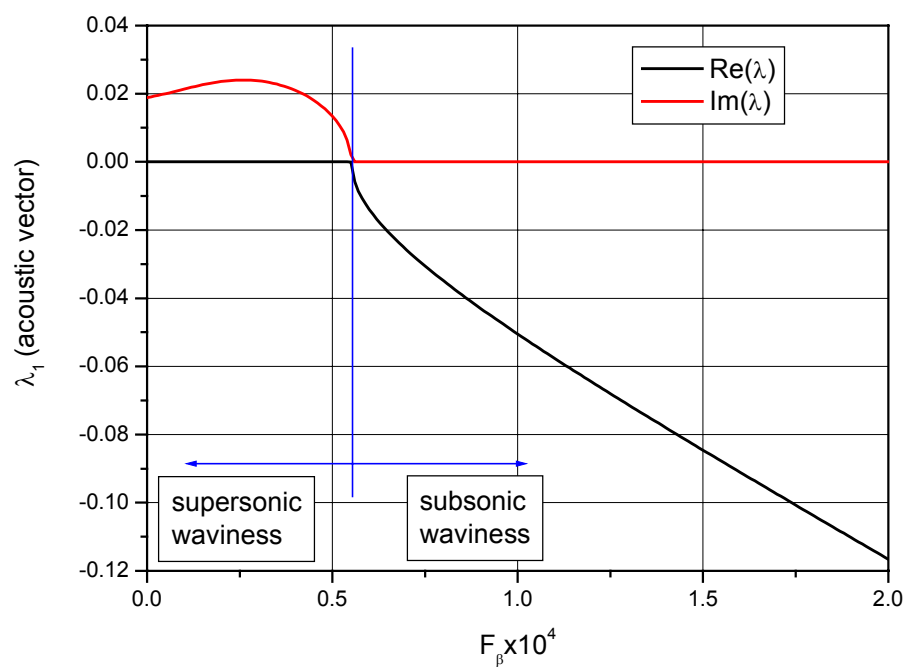
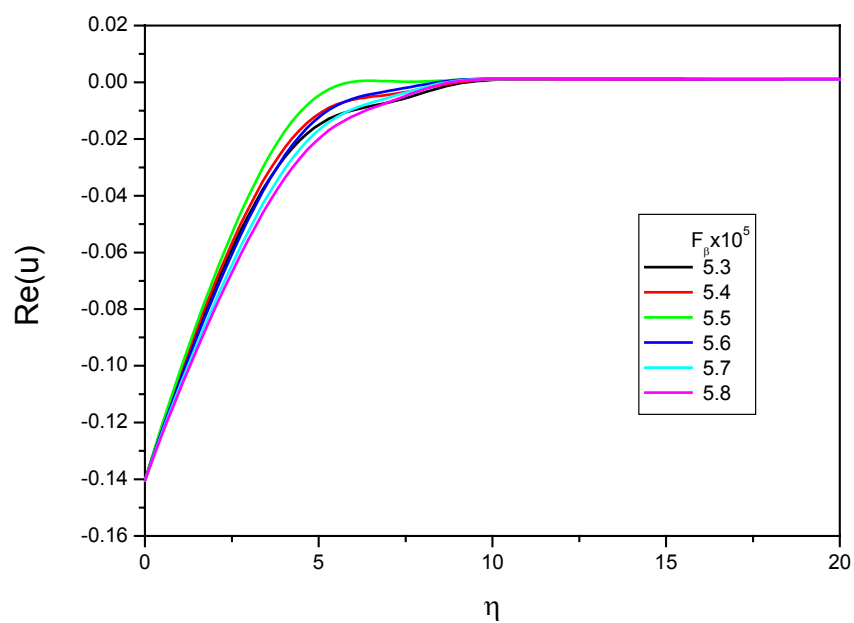
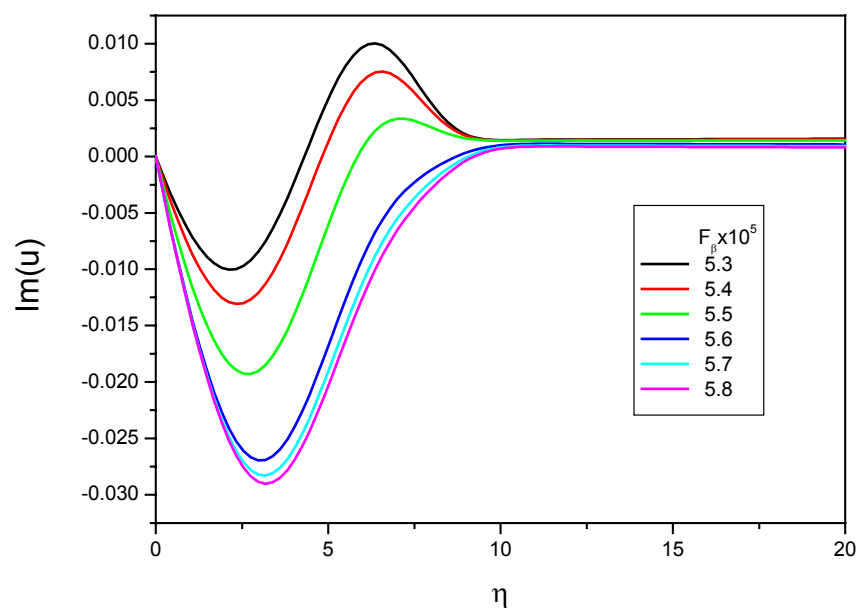


Fig. 18. The function $\lambda_1(F_\beta)$ for the case of fast acoustic wave of $\Theta_y = 0$, $\Theta_z = 45^\circ$, $R = 620$, $F = 1.4 \times 10^{-5}$.

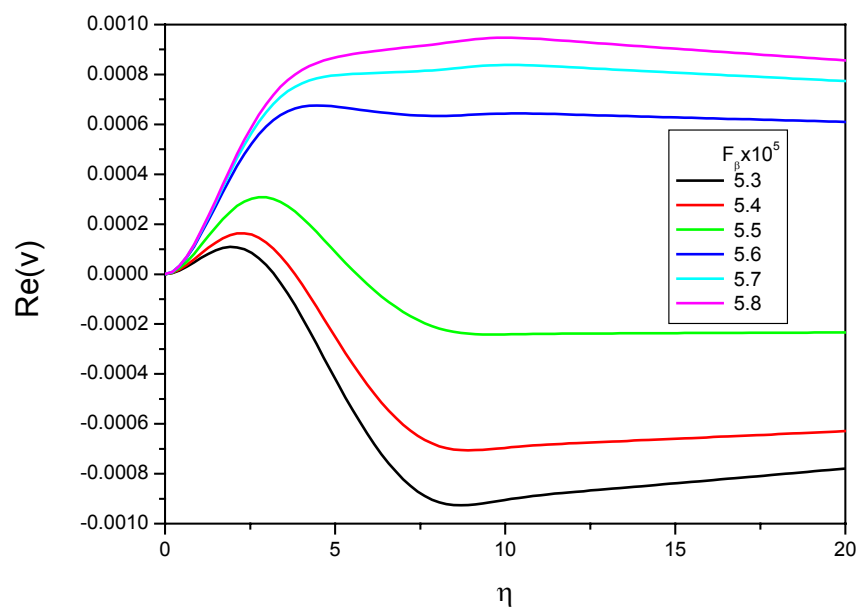


(a)

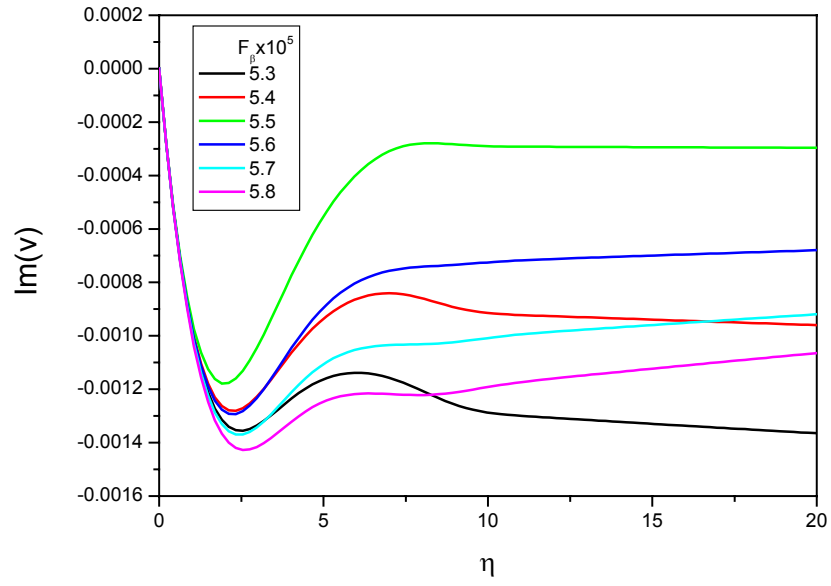


(b)

Fig. 19. Distributions of the x -component velocity induced by the wavy wall in the vicinity of the transonic point $F_\beta \approx 5.5 \times 10^{-5}$.



(a)



(b)

Fig. 20. Distributions of the y -component velocity induced by the wavy wall in the vicinity of the transonic point $F_\beta \approx 5.5 \times 10^{-5}$.

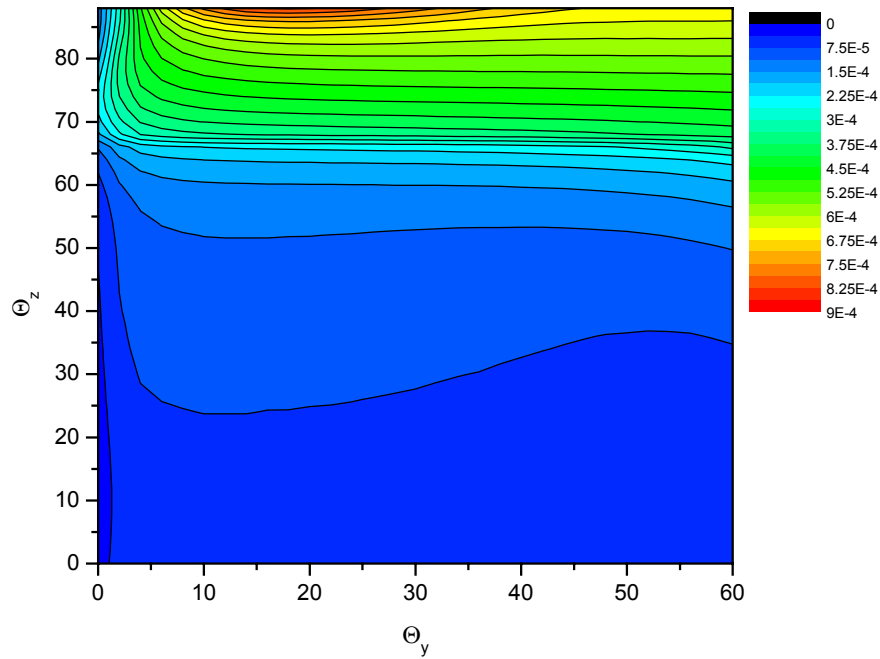


Fig. 21. Modulus of receptivity coefficient as a function of the fast acoustic-wave angles Θ_y and Θ_z ; $R = 620$, $F = 1.4 \times 10^{-5}$, $F_\beta = 6.8 \times 10^{-5}$.

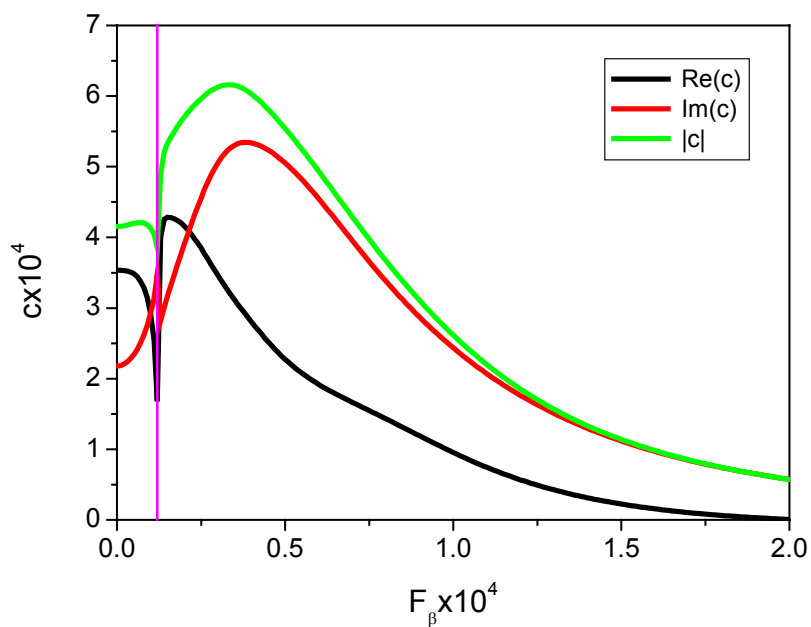


Fig. 22a. Receptivity coefficient as a function of F_β for slow acoustic wave of $\Theta_y = 45^\circ$, $\Theta_z = 0$; $R = 620$, $F = 1.4 \times 10^{-5}$.

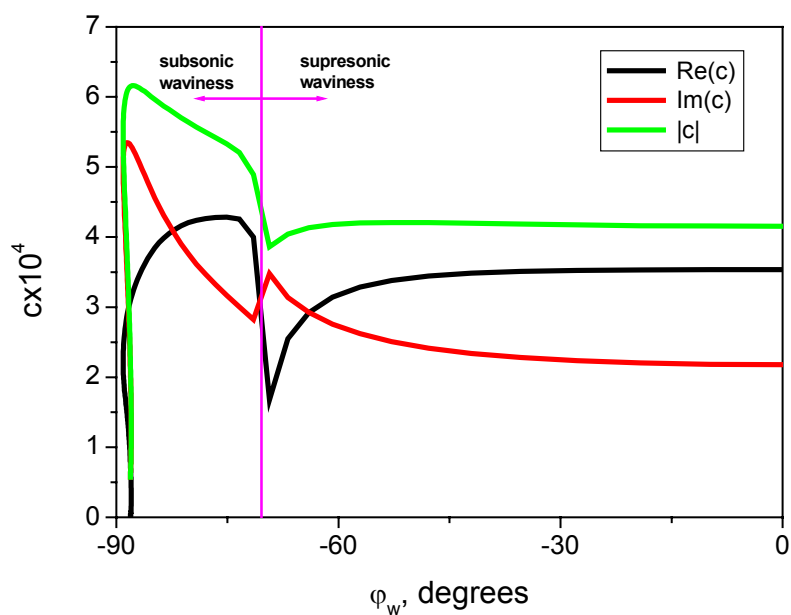


Fig. 22b. Receptivity coefficient as a function of φ_w for slow acoustic wave of $\Theta_y = 45^\circ$, $\Theta_z = 0$; $R = 620$, $F = 1.4 \times 10^{-5}$.

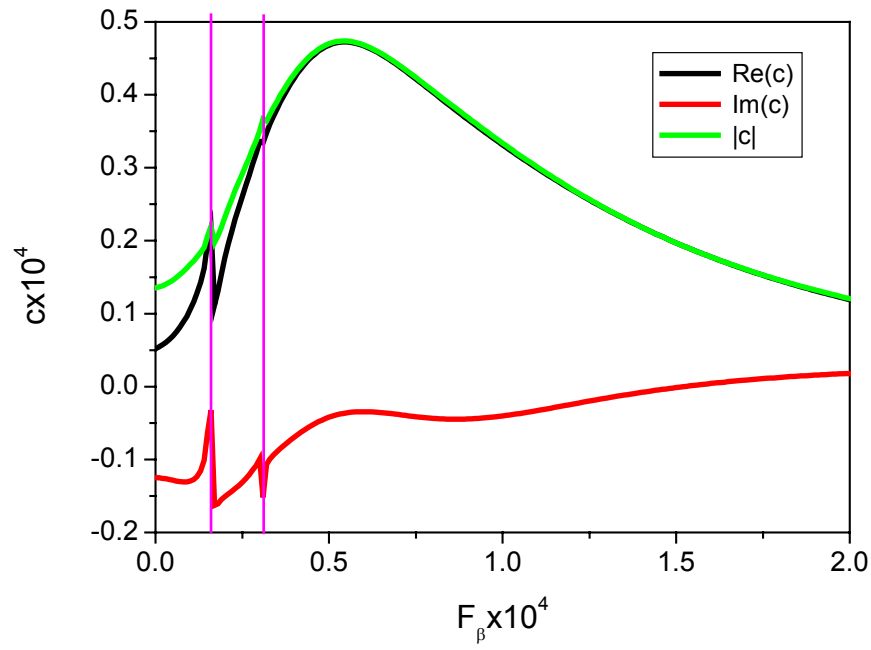


Fig. 23a. Receptivity coefficient as a function of F_β for slow acoustic wave of $\Theta_y = 0$, $\Theta_z = 45^\circ$; $R = 620$, $F = 1.4 \times 10^{-5}$.

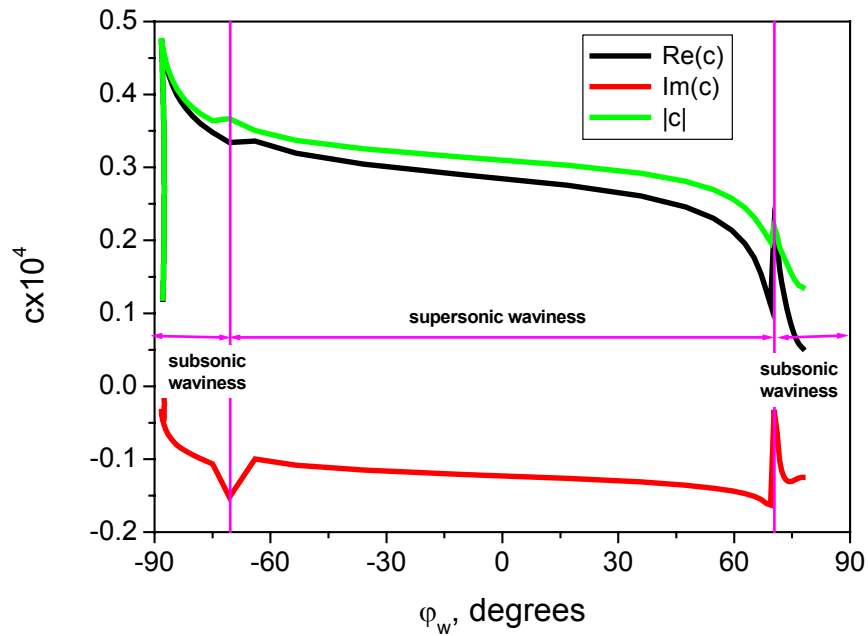


Fig. 23b. Receptivity coefficient as a function of φ_w for slow acoustic wave of $\Theta_y = 0$, $\Theta_z = 45^\circ$; $R = 620$, $F = 1.4 \times 10^{-5}$.

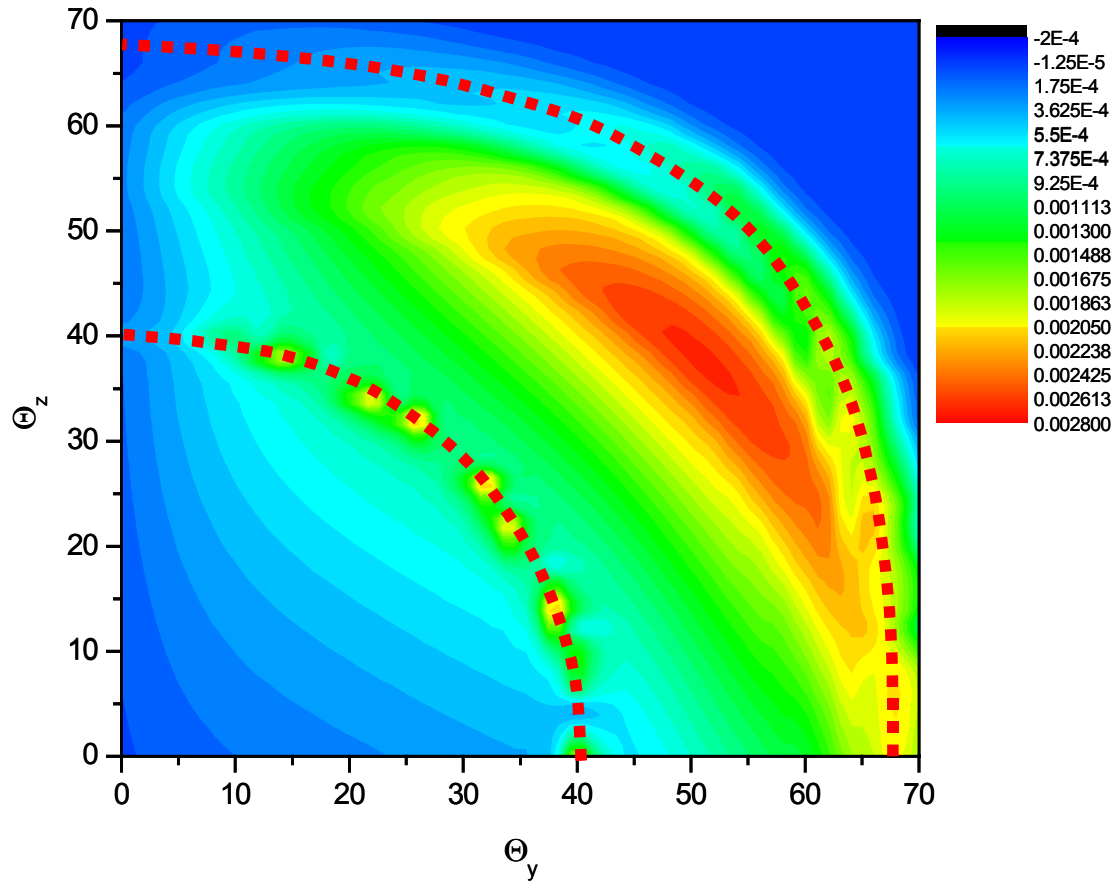


Fig. 24. Modulus of receptivity coefficient as a function of the slow acoustic-wave angles Θ_y and Θ_z ; $R = 620$, $F = 1.4 \times 10^{-5}$, $F_\beta = 6.8 \times 10^{-5}$; dashed red lines shows Θ_y and Θ_z of transonic resonant waviness.

7. Recommendations for design of receptivity experiments in quiet wind tunnels

Receptivity problem depends on many parameters including:

- Freestream parameters
- Mean flow parameters
- Spectral characteristics of acoustic field and other freestream disturbances
- Shape and location of roughness element

To reduce the number of independent parameters and focus on basic features of the receptivity process, experiments should be conducted on bodies of simple geometry, namely, on a flat plate with sharp leading edge at zero angle of attack (see Fig. 6). In this case: the bow shock is weak and its effect on acoustic field is minimal; mean-flow profiles in the boundary layer are easy to simulate; the boundary-layer disturbances (first and second modes) are well known. Even for this simple configuration, measurements of the receptivity coefficients are not straightforward.

The major challenge is associated with the fact that it is difficult to separate the boundary-layer disturbances induced by acoustic waves interacting with different non-uniformities of the mean flow. For example, acoustic waves radiating the flat plate with a local roughness element generate the boundary-layer modes near the plate leading edge and in the roughness vicinity. If hot-wire measurements are performed in the boundary layer downstream from the roughness element, then the hot-wire signal includes the disturbances from the both regions as well as the acoustic field comprising both fast and slow waves. In this case, it is difficult to identify signals relevant to various sources of receptivity.

This difficulty may be resolved using acoustic disturbances of relatively short duration as sketched in Fig. 25. If the acoustic source emanates a disturbance comprising few wavelengths (wave train), then the acoustic wave train and the wave trains of boundary-layer modes are observed in different time intervals. The hot wire first detects the train of fast acoustic waves, then the train of boundary-layer waves generated by the fast acoustic waves on the roughness element, then the train of boundary-layer waves generated by the fast acoustic waves near the plate leading edge. Similar sequence of signals is related to the train of slow acoustic waves. Tracking these signals it is feasible to measure characteristics of every wave train and calculate the correspondent receptivity coefficients.

By placing the acoustic source at various positions with respect to the roughness element it is possible to radiate the latter by acoustic wave trains of various front angles Θ_y , Θ_z (see Fig. 26). This makes feasible to measure the receptivity coefficients as functions of Θ_y , Θ_z and verify the correspondent theoretical dependencies.

Our theoretical analysis showed that receptivity to acoustic waves interacting with the roughness element strongly depends on the roughness locus and shape. For experiments on excitation of second-mode disturbances, which are dominant in high-speed boundary layer, it is reasonable to

focus on 2-D roughness since most unstable disturbances are two-dimensional. This may be a strip mounted on the plate at a certain streamwise station x_s as schematically shown in Fig. 27. The theory predicts that most receptive region corresponds to the lower neutral branch. Placing the strip at this station and varying the free-stream unit Reynolds number one could observe the receptivity dependence on the roughness element locus relative to the neutral point. Special attention should be given to the choice of the strip width d_x . Our theoretical analysis indicates that receptivity is maximal for d_x corresponding to the resonance conditions; i.e., the strip width should be chosen as $d_x \approx 2\pi / |\alpha_2 \pm \alpha_a|$, where α_2, α_a is the wave-number of second mode and acoustic wave, respectively. For more accurate estimates of the strip size and its locus, it is recommended to conduct calculations of receptivity coefficients for particular experimental conditions using the module RECEPT.

For boundary layers at moderate supersonic speeds (which are typified by the experiments of Graziosi and Brown [41] in the Mach=3 quiet wind tunnel of Princeton University), 3-D waves of the first mode (Tollmien-Schlichting waves) are most unstable. Experiments on excitation of TS waves should be focused on 3-D acoustic waves interacting with 2-D/3-D roughness elements. It is reasonable to start with cylindrical sources, which generate predominately 2-D acoustic waves, and the periodic 3-D roughness structure schematically shown in Fig. 28. The streamwise size d_x and the transversal period d_z of this structure are estimated as $d_x \approx 2\pi / |\alpha_1 \pm \alpha_a|$, $d_z \approx 2\pi / |\beta_1|$, where (α_1, β_1) are wave-number components of most unstable TS waves. As in the case of the second-mode excitation, roughness should be placed at the streamwise station relevant to the lower neutral branch of the first mode.

The parametric calculations of Section 6 show that the receptivity coefficient is singular if the roughness is transonic: the freestream velocity component normal to the front of roughness elements corresponds to the Mach number $M_n = 1$ (see Fig. 16). It is interesting to verify this theoretical finding by testing the roughness patterns of various angularities φ_w (from supersonic to subsonic).

Since receptivity is multi-parametric problem associated with delicate physical mechanisms, design of receptivity experiments should be guided by theoretical modeling of experimental conditions. This may be done using the receptivity module RECEPT. With such a combined theoretical and experimental approach, it is feasible to identify and investigate various features of supersonic boundary layer receptivity by performing non-extensive experimental programs. This helps to reduce the risk and cost of experiments, especially in high-speed wind tunnels where runs are quite expensive.

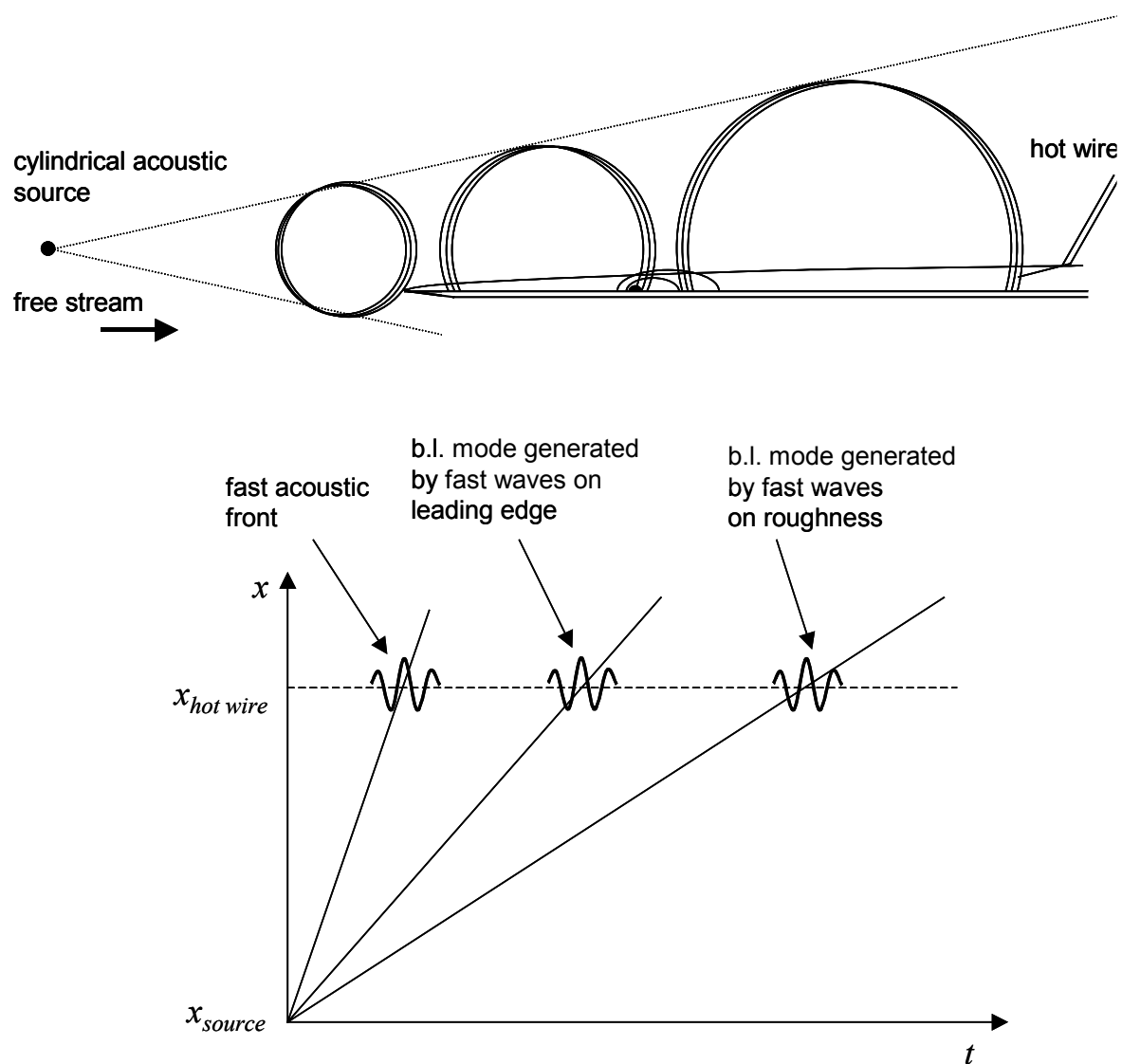


Fig. 25. Hot-wire measurements of disturbances generated by acoustic wave train in supersonic boundary layer.

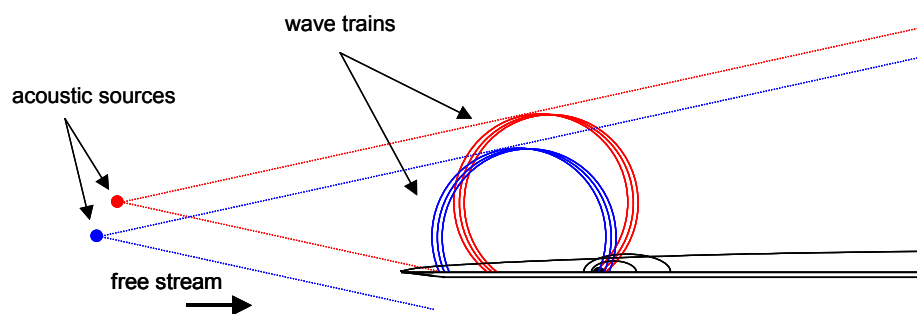


Fig. 26. Acoustic sources at various positions (red and black points) radiate the roughness element by wave trains of various front angles Θ_y .

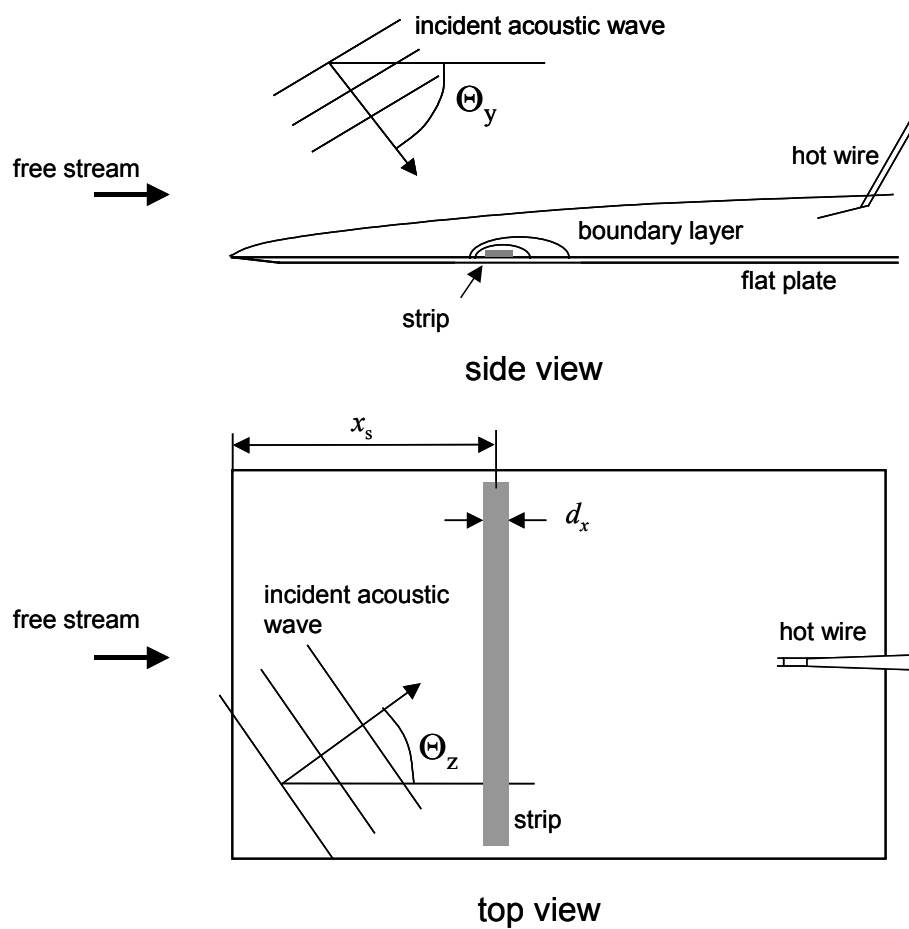


Fig. 27. Receptivity to acoustic waves interacting with 2-D roughness element (strip).

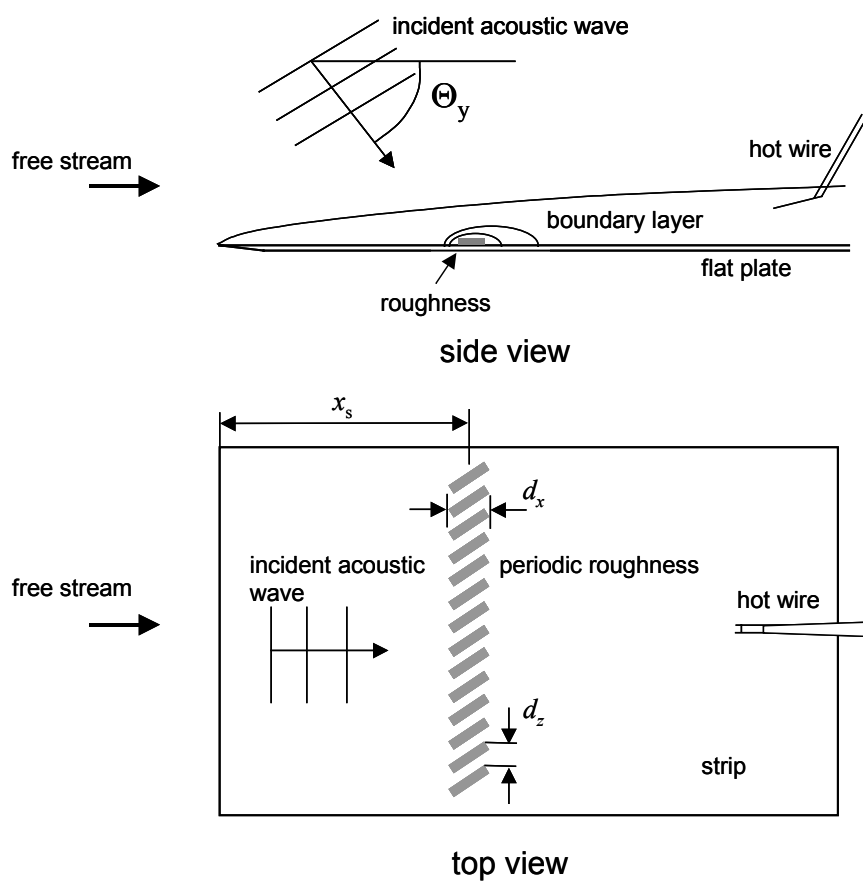


Fig. 28. Receptivity to acoustic waves interacting with 3-D periodic roughness element.

8. Conclusions

1. Analysis of high-speed boundary layer receptivity to 3-D external waves interacting with 3-D roughness element or waviness was performed and summarized in the AIAA Paper 2003-3137 (33rd Fluid Dynamics Conf. and Exhibit, 23-26 June 2003, Orlando Florida)
2. The FORTRAN computational module RECEPT.FOR was developed and delivered to the end user Dr. Roger Kimmel with the usage instructions. This module allows for calculations of the receptivity coefficients and the weight coefficients for modes of discrete spectrum (TS waves, second mode etc.).
3. It was shown that the RECEPT (with the option providing calculations of the weight coefficient for a particular discrete mode) allows for extraction of the normal wave of relatively small amplitude ($\sim 0.1\%$) from the disturbance field. With this tool, the user can identify normal waves, which latent in a “messy” disturbance field at early stages of instability. This is of particular importance for analyses of DNS results and experimental data in connection with receptivity and stability problems.
4. The module RECEPT was applied to the problem of high-speed boundary-layer receptivity to acoustic disturbances interacting with 3-D roughness element. Namely, the receptivity coefficients were calculated for 2-D second-mode excited by 3-D incident acoustic wave interacting with 3-D roughness element on a flat plate. These calculations were conducted for the free-stream Mach number 6 at flow and wall temperatures typical for quiet wind tunnels. It was found that the receptivity coefficient monotonically decreases with the acoustic-wave inclination angle Θ_z for both fast and slow incident waves. 2-D acoustic waves interacting with 3-D local roughness element provide maximum excitation of 2-D second mode. At $\Theta_z = \text{fixed}$, the modulus of receptivity coefficient has maximum versus the angle of incidence Θ_y . In the case of $\Theta_z = 0$ (2-D acoustic waves) this maximum is observed at $\Theta_y \approx 40^\circ$ for fast waves, and $\Theta_y \approx 50^\circ$ for slow waves. Receptivity to slow acoustic waves is higher than to fast waves. The initial phase of the excited second mode strongly depends on the angle of incidence. This may significantly reduce the second-mode initial amplitude, if acoustic waves are distributed over a wide range of Θ_y .
5. The receptivity coefficients were calculated for 3-D Tollmien-Schlichting waves (first mode) generated by acoustic waves interacting with local roughness element. These calculations were performed for the boundary layer on a flat plate at Mach=3 free stream with parameters relevant to the receptivity experiments of Graziosi and Brown [41]. It was found that the receptivity coefficient is singular if the resonant wall waviness is transonic; i.e., the free-stream velocity component normal to the waviness front equals the speed of sound. Numerical examples show that maximum of the receptivity coefficient associated with slow acoustic waves is essentially larger than that associated with fast waves.
6. Recommendations for design of receptivity experiments in supersonic quiet wind tunnels were formulated. It was recommended to conduct receptivity experiments on a flat plate in order to focus on basic features of receptivity process and minimize the number of independent parameters. It was pointed out that the major challenge of receptivity measurements is associated with the fact that it is difficult to sort out the boundary-layer

disturbances induced by acoustic waves interacting with different non-uniformities of the mean flow. This difficulty may be resolved using acoustic wave trains.

7. Since receptivity is multi-parametric problem associated with delicate physical mechanisms, design of receptivity experiments should be guided by theoretical modeling of experimental conditions, which could be performed using the module RECEPT. With such a combined theoretical and experimental approach, it is feasible to identify and investigate various features of supersonic boundary-layer receptivity by conducting non-extensive experimental programs. This helps to reduce the risk and cost of experiments, especially in high-speed wind tunnels where runs are quite expensive.

9. Future effort

Another mechanism of receptivity is associated with nonlinear interactions of freestream disturbances. Choudhari and Streett [22] pointed out that the bilinear interaction between a pair of freestream waves could be important in excitation of unstable disturbances. Wu [42] elaborated this mechanism considering suitable convecting gusts, which interact with sound waves producing a forcing that has the same time and length scales as those of Tollmien-Schlichting waves in the neutral point vicinity. The sound-convective gust interaction may be dominant in boundary layers at subsonic and low supersonic speeds.

For high-speed boundary layers it is feasible to identify pair of acoustic waves, which satisfies the resonance condition $\omega_n = \omega_{a1} \pm \omega_{a2}$ and the synchronization conditions $\alpha_n = \alpha_{a1} \pm \alpha_{a2}$, $\beta_n = \beta_{a1} \pm \beta_{a2}$. Here ω_a , α_a , β_a - frequency and wavenumber components of acoustic waves; ω_n , α_n , β_n - correspondent characteristics of the boundary-layer mode (this could be the first $n = 1$ or second $n = 2$ mode). Under these conditions, the scale conversion is achieved without resorting of a local non-homogeneity of the mean flow (roughness element, waviness etc.), that may give large receptivity coefficients on smooth surfaces. Moreover, one of interacting acoustic waves may belong to the low-frequency band, which corresponds to intense disturbances especially in the wind-tunnel free stream.

Our preliminary estimates show that the bilinear sound-sound interaction induces the boundary-layer modes of the amplitude $A_{n,0} \sim A_a^2 / R_{\delta^*}^{1/4}$, where R_{δ^*} is displacement thickness Reynolds number. For high-speed boundary layers, the Reynolds number is $R_{\delta^*} \sim 10^4$. Assuming that the transitional amplitude $A_{n,tr} \sim 10^{-2}$ and the amplification factor $N \sim 6$, we estimate the initial amplitude as $A_{n,0} \sim 10^{-2} e^{-6} \sim 10^{-5}$, which corresponds to the acoustic-wave amplitude $A_a \sim \sqrt{A_{n,0} R_{\delta^*}^{1/4}} \sim \sqrt{10^{-6}} = 0.1\%$. Such levels of acoustic disturbances may be generated by turbulent boundary layers on forebody surfaces (in flight) or nozzle walls (in wind tunnels). This leads to expectation that the bilinear sound-sound interaction may dominate the receptivity process.

To our knowledge the discussed above mechanism has not been studied yet. We suggest to perform theoretical studies of the bilinear sound-sound interaction and incorporate this receptivity mechanism into the computational module RECEPT.

References

1. Finley, D. "Hypersonic Aerodynamic Considerations and Challenges," AIAA Paper, No. 90-5222, Oct. 1990.
2. Kimmel, R., and Walker, S. H., "Research Directions in Hypersonic Boundary Layer Transition," A White Paper presented to Contractor's Meeting in Unsteady Aerodynamics and Hypersonics, AFOSR, September 8-10, Dayton.
3. Morkovin, M.V., "Critical Evaluation of Transition from Laminar to turbulent Shear Layers with Emphasis on Hypersonically Traveling Bodies," AFFDL-TR-68-149, Air Force Flight Dynamics Laboratory, Wright-Patterson AFB, OH, 1969.
4. Hefner, J.N., and Bushnell, D.M., "Application of Stability Theory to Laminar Flow Control," AIAA Paper No. 79-265, 1979.
5. Morkovin, M. V., "Bypass-Transition Research: Issues and Philosophy," *Instabilities and Turbulence in Engineering Flows*, ed. by Gatski and Hirsh, Kluwer, pp. 3-30, 1993.
6. Reshotko, E., "Boundary Layer Stability and Transition," *Ann. Rev. Fluid Mech.*, Vol. 8, pp. 311-349, 1976.
7. Reshotko, E., "Boundary Layer Instability, Transition and Control," AIAA Paper No. 94-0001, 1994.
8. Reed, H.L., Saric, W.S., and Arnal, D., "Linear Stability Theory Applied to Boundary Layers," *Ann. Rev. Fluid Mech.*, Vol. 28, pp. 389-428, 1996.
9. Arnal, D., Casalis, G., and Juillen, J.C., "A Survey of the Transition Prediction Methods: from Analytical Criteria to PSE and DNS," *Laminar Turbulent Transition*, ed. by R. Kobayashi, Sendai, Japan, Springer Verlag, pp. 3-14, 1995.
10. Malik, M.R., "Boundary-Layer Transition Prediction Toolkit," AIAA Paper No. 97-1904, June 29 - July 2, 1997.
11. Malik, M.R., "COSAL – A Black Box Compressible Stability Theory Analysis Code for Transition Prediction in Three-Dimensional Boundary Layers," NASA CR-165925.
12. Gaponov, S.A., "Nonparallel Flow Effect on Disturbance Evolution in Supersonic Boundary Layer," *Izv. AN SSSR. Mekhanika Zhidkosti i Gaza*, No. 2, pp. 26-31, 1980.
13. Tumin, A.M., and Fedorov, A.V., "On the Effect of Weak Flow Nonuniformity on Stability Characteristics," *Uchenye. Zapiski TsAGI*, Vol. 13, No. 6, pp. 91-96, 1982.
14. El-Hady, N.M., "Non-Parallel Instability of Supersonic and Hypersonic Boundary Layers," AIAA Paper No. 91-0324, 1991.
15. Bertolotti, F.P., and Herbert, Th., "Analysis of the Linear Stability of Compressible Boundary Layers Using the PSE," *Theoretical and Computational Fluid Dynamics*, Vol. 3, pp. 117-124, 1991.

16. Chang, C.-L., Malik, M.R., Erlebacher, G., and Hussaini, M.Y., "Compressible Stability of Growing Boundary Layers Using Parabolized Stability Equations," AIAA Paper No. 91-1636, 1991.
17. Malik, M.R., and Li, F., "Transition Studies for Swept Wing Flows Using PSE," AIAA Paper No. 93-0077, 1993.
18. Zhong, X., "Direct Numerical Simulation of Hypersonic Boundary Layer Transition over Blunt Leading Edges, Part I: A New Numerical Method and Validation," AIAA Paper No. 97-0755, 1997.
19. Fedorov, A.V., and Khokhlov, A.P., "Excitation and Evolution of Unstable Disturbances in Supersonic Boundary Layer," Proc. of 1993 ASME Fluid Engineering Conference, Washington, DC, June 20-24, 1993, FED-Vol. 151, Transitional and Turbulent Compressible Flows, ASME 1993, pp.1-13, 1993.
20. Fedorov, A.V., "Receptivity of a high-speed boundary layer to acoustic disturbances," *Journal of Fluid Mechanics*, Vol. 491, 2003, pp. 101 – 129.
21. Fedorov, A. V., and Khokhlov, A. P., "Prehistory of Instability in a Hypersonic Boundary Layer," *Theoretical and Computational Fluid Dynamics*, Vol. 14, No. 6, 2001, pp. 359-375.
22. Choudhari, M., Streett, C., "Boundary Layer Receptivity Phenomena in Three-Dimensional and High-Speed Boundary Layers," AIAA paper 90-5258.
23. Fedorov A.V., and Khokhlov, A.P., "Receptivity of Hypersonic Boundary Layer to Wall Disturbances," *Theoretical and Computational Fluid Dynamics*, Vol. 15, No. 4, 2002, pp. 231-254.
24. Zhigulev, V.N., and Tumin, A.M., Onset of Turbulence, Nauka, Novosibirsk, 1987.
25. Aizin, L.B., and Polyakov, M.F., "Acoustic Generation of Tollmien-Schlichting Waves over Local Unevenness of Surface Immersed in Stream," Preprint No. 17, SO AN SSSR, Institute of Theoretical and Applied Mechanics, Novosibirsk, 1979 (in Russian).
26. Fedorov, A.V., "Excitation and Development of Unstable Disturbances in Compressible Boundary Layer," Ph.D. Dissertation, Moscow Institute of Physics and Technology, 1982 (in Russian).
27. Zavol'skii, N.A., Reutov, V.P., Rybushkina, G.V., "Excitation of Tollmien-Schlichting Waves by Acoustic and Vortex Disturbance Scattering in Boundary Layer on a Wavy Surface," *J. Appl. Mech. Tech. Phys.*, Vol. 24, pp. 355-361, 1983.
28. Zhigulev, V.N., and Fedorov, A.V., "Boundary Layer Receptivity to Acoustic Disturbances," *J. Appl. Mech. And Tech. Phys.*, Vol. 28, pp. 28-34, 1987.
29. Goldstein, M.E., "Scattering of Acoustic Waves into Tollmien-Schlichting Waves by Small Streamwise Variations in Surface Geometry," *J. Fluid Mech.*, Vol. 154, p. 509, 1985.
30. Ruban, A.I., "On the Generation of Tollmien-Schlichting Waves by Sound," *Fluid Dyn.*, Vol. 19, p. 709, 1985.
31. Goldstein, M.E., and Hultgren, L.S., "Boundary-Layer Receptivity to Long-Wave Free-Stream Disturbances," *Annu. Rev. Fluid Mech.*, Vol. 21, p. 137, 1989.

32. Nishioka, M., and Morkovin, M.V., "Boundary-Layer Receptivity to Unsteady Pressure Gradients: Experiments and Overview," *J. Fluid Mech.*, Vol. 171, p. 219, 1989.
33. Kerschen, E.J., "Boundary Layer Receptivity Theory," AIAA Paper No. 89-1109, 1989.
34. Wiegel, M., and Wlezein, R.W., "Acoustic Receptivity of Laminar Boundary Layers over Wavy Walls," AIAA Paper No. 93-3280, 1993.
35. Choudhari, M., Street, C.L., "A Finite Reynolds-Number Approach for the Prediction of Boundary-Layer Receptivity in Localized Regions," *Phys. Fluids, A* Vol. 4 (11), pp. 2495-2514, 1992.
36. Choudhari, M., Street, C.L., "Theoretical Prediction of Boundary-Layer Receptivity," AIAA Paper No. 94-2223, 1994.
37. Crouch, J.D., "Theoretical Studies on the Receptivity of Boundary Layers," AIAA Paper No. 94-2224, 1994.
38. Saric, W.S., Hoos, J.A., and Radeztsky, R.H., "Boundary-Layer Receptivity of Sound with Roughness," in: *Boundary Layer Stability and Transition to Turbulence*, ASME FED-Vol. 114, pp. 17-22, 1991.
39. Choudhari, M., and Street, C., *Boundary Layer Receptivity Phenomena in Three-Dimensional and High-Speed Boundary Layers*, AIAA Paper No. 90-5258, 1990.
40. Fedorov, A.V., "Receptivity of Hypersonic Boundary Layer to Acoustic Disturbances Scattered by Surface Roughness," AIAA Paper No. 2003-3137, 33rd Fluid Dynamics Conf., 23-26 June 2003, Orlando Florida.
41. Graziosi, P., and Brown, G.L., "Experiments on Stability and Transition at Mach 3," *J. Fluid Mech.*, Vol. 472, 2002, pp. 83-124.
42. Wu, X., "Generation of Tollmien-Schlichting Waves by Convecting Gusts Interacting with Sound," *J. Fluid Mech.*, Vol. 397, 1999, pp. 285-316.

List of papers

1. Fedorov, A.V., "Receptivity of Hypersonic Boundary Layer to Acoustic disturbances Scattered by Surface Roughness," AIAA Paper No. 2003-3731, 33rd Fluid Dynamics Conference and Exhibit, 23-26 June 2003, Orlando, Florida.

Abstract

Theoretical study of hypersonic boundary-layer receptivity to acoustic waves interacting with wall waviness (distributed roughness) or a hump (local roughness) is performed using a combination of asymptotic and numerical techniques. It is shown that strong excitation of unstable disturbances occurs in local regions where the forcing, which is due to bilinear interaction of external waves with wall-induced disturbances, is in resonance with the boundary-layer modes. The receptivity coefficients are presented for two-dimensional second mode generated by acoustic disturbances of various frequencies and incident angles interacting with distributed and local roughness on a flat plate at Mach 6. The theoretical model can be used to predict initial amplitudes of the second mode, which is dominant instability in essentially two-dimensional boundary layers at hypersonic speeds.

2. Egorov, I.V., Fedorov, A.V., and Soudakov, V.G., "Direct Numerical Simulation of Unstable Disturbances in Supersonic Boundary Layer," AIAA Paper No. 2004-0588, 42nd AIAA Aerospace Sciences Meeting and Exhibit, Jan. 5-9, 2004, Reno, Nevada.

Abstract

A numerical algorithm and code are developed and applied to direct numerical simulation (DNS) of unsteady two-dimensional flow fields relevant to transition at supersonic and hypersonic speeds. An implicit second-order finite-volume technique is used for solving the compressible Navier-Stokes equations. Numerical simulation of disturbances generated by a periodic suction-blowing on a flat plate is performed at freestream Mach number 6. For small forcing amplitudes, the second-mode growth rates predicted by DNS agree well with the growth rates resulted from the linear stability theory including nonparallel effects. Calculations at large forcing amplitudes illustrate nonlinear dynamics of the disturbance flow field. DNS predicts a nonlinear saturation of fundamental harmonic and rapid growth of higher harmonics. These results are consistent with the experimental data of Stetson and Kimmel obtained on a sharp cone at the free-stream Mach number 8. The code can be used for direct simulation of receptivity and nonlinear dynamics in highly non-uniform flows such as separation bubbles, surface irregularities and leading edges.

Appendix

Receptivity of Hypersonic Boundary Layer to Acoustic Disturbances Scattered by Surface Roughness

**AIAA Paper No. 2003-3137, 33rd Fluid Dynamics Conf. and Exhibit, 23-26
June 2003, Orlando Florida**

RECEPTIVITY OF HYPERSONIC BOUNDARY LAYER TO ACOUSTIC DISTURBANCES SCATTERED BY SURFACE ROUGHNESS

A.V. Fedorov*

Department of Aeromechanics and Flight Engineering, Moscow Institute of Physics and Technology,
Zhukovskiy, 140180, Russia
afedorov@pt.comcor.ru

Abstract

Theoretical study of hypersonic boundary-layer receptivity to acoustic waves interacting with wall waviness (distributed roughness) or a hump (local roughness) is performed using a combination of asymptotic and numerical techniques. It is shown that strong excitation of unstable disturbances occurs in local regions where the forcing, which is due to bilinear interaction of external waves with wall-induced disturbances, is in resonance with the boundary-layer modes. The receptivity coefficients are presented for two-dimensional second mode generated by acoustic disturbances of various frequencies and incident angles interacting with distributed and local roughness on a flat plate at Mach 6. The theoretical model can be used to predict initial amplitudes of the second mode, which is dominant instability in essentially two-dimensional boundary layers at hypersonic speeds.

Nomenclature			
\mathbf{A}_k	= eigenvector(direct problem)	Θ	= angle of incidence
\mathbf{B}_k	= eigenvector(adjoint problem)	θ	= temperature disturbance
c	= phase speed	$\mathbf{F}(x, y)$	= amplitude vector-function
$F = \omega^* v_e^* / U_e^{*2}$	= frequency parameter	<i>Subscripts</i>	
f	= mass-flow disturbance	0	= resonance point
G	= receptivity function	a	= acoustic
g	= roughness shape-function	ad	= adiabatic
L	= streamwise scale	b	= branch point
M	= Mach number	dis	= distributed
$\tilde{p} = p^* / (\rho_e^* U_e^{*2})$	= pressure disturbance	e	= upper boundary-layer edge
$p = p^* / P_e^*$	= pressure disturbance	loc	= local
q	= receptivity factor	w	= wall
t	= time	<i>Superscripts</i>	
T	= mean flow temperature	bar	= complex conjugate
U, V	= mean flow velocity	asterisk	= dimensional
u, v, w	= velocity disturbance		
x, y, z	= Cartesian coordinates		
$x_1 = x^* / L^*$	= slow variable		
α, β	= wave-vector components		
$\varepsilon = \delta^* / L^*$	= small parameter		
Δ^*	= boundary-layer thickness		
ν	= kinematic viscosity		
ω	= angular frequency		

1. Introduction

Important mechanism of boundary-layer receptivity is the interaction of acoustic disturbances with steady disturbances induced by spatial variations of boundary conditions on the wall surface such as roughness/waviness, local heating/cooling and suction/blowing. Early experimental¹ and theoretical²⁻⁴ studies of this mechanism were performed in Russia for subsonic flows. Their results were summarized in Ref. [5]. An asymptotic theory of the Tollmien-Schlichting wave excitation due to interaction of acoustic waves with surface irregularities was

* Associate Professor, Department of Aeromechanics and Flight Engineering, Member AIAA

developed in Refs. [6-8] and reviewed in Refs. [8-10]. Detailed parametrical studies were represented in Refs. [11-14]. The theoretical predictions are in good agreement with the experiment¹⁵ conducted on a flat plate in low-speed wind tunnel.

Receptivity of high-speed boundary layers (in the Mach number range from 1.15 to 4.5) to freestream disturbances interacting with surface irregularities was analyzed by Choudhari and Streett¹⁶. They reported that, although the Mach=4.5 boundary layer is nearly 6 times thicker than in the Mach=0 case, the instability amplitudes generated by a wall hump of fixed height are only marginally smaller than those at low speeds. This example indicates that receptivity of hypersonic boundary layer to acoustic plus roughness disturbances may play important role in the initial phase of transition.

In this paper, we discuss theoretical analysis of hypersonic boundary-layer receptivity to acoustic waves interacting with surface waviness (distributed excitation) or hump (local excitation) on a flat plate. In Section 2, we formulate the problem and show that its main features are similar to the case of receptivity to wall disturbances.¹⁷ In Section 3, we discuss numerical results related to excitation of the second mode by fast and slow acoustic waves of various angles of incidence. In Section 4, we conclude the paper.

2. Problem formulation and analysis

Hereafter we consider excitation of the boundary-layer modes by acoustic waves radiating a flat plate with a wavy surface (distributed receptivity) or a hump (local receptivity). Analysis is conducted using the method¹⁷ for receptivity to wall-induced disturbances.

2.1 Distributed receptivity on wavy surface

Consider two-dimensional laminar boundary layer of perfect gas on a flat plate in hypersonic freestream. The global streamwise length L^* is assumed to be much larger than the boundary layer thickness scale $\delta^* = \sqrt{\nu_e^* L^* / U_e^*}$; i.e. the ratio $\varepsilon = \delta^* / L^*$ is small. The longitudinal x^* , normal y^* , transversal z^* coordinates and time t^* are made nondimensional as $(x, y, z) = (x^*, y^*, z^*) / \delta^*$, $t = t^* U_e^* / \delta^*$. Introducing the slow variable $x_1 = x^* / L^* = \varepsilon x$ we can specify

the nondimensional mean-flow velocity (U, V) , and temperature T as

$$U \equiv U^* / U_e^* = U(x_1, y), \quad V \equiv V^* / U_e^* = \varepsilon V_0(x_1, y),$$

$$T \equiv T^* / T_e^* = T(x_1, y), \quad (1)$$

The wall waviness is represented in the form

$$y_w(x, y, z) = h \exp(i\alpha_w x + i\beta_w z) + (c.c.), \quad (2)$$

where $h = h^* / \delta^*$ is nondimensional amplitude, (α_w, β_w) is wavenumber vector. It is assumed that the wavelength is of the order of the boundary-layer thickness Δ^* ($U^* = 0.99 U_e^*$ at $y^* = \Delta^*$). With h^* being smaller than the viscous sublayer thickness, the wavy wall generates small steady disturbances governed by the linearized Navier-Stokes equations.¹⁸

An external acoustic wave of the angular frequency ω and the wavenumber (α_a, β_a) , incidents upon the plate as schematically shown in Fig. 1. Its physical quantities are expressed in a traveling-wave form. For example, the pressure is

$$p = p_{a,inc} \exp[i(\alpha_a x + \beta_a z + k_{a,inc} y - \omega t)] + (c.c.) \quad (3)$$

The vertical wave-number component, $k_{a,inc}$, is determined from the acoustic dispersion relation $k_{a,inc} = k_{a,inc}(\alpha_a, \omega, M)$, where M is freestream Mach number. The incident wave is refracted by the boundary layer and reflected by the wavy wall. Interacting with the waviness-induced disturbance the acoustic wave generates boundary-layer normal waves including unstable modes. Our objective is to determine the receptivity function coupling characteristics of the incident acoustic wave and the wall waviness with the normal waves.

Using the approach¹⁷ we represent the unsteady flow field by the vector function

$$\Psi(x, y, t) = (u, \frac{\partial u}{\partial y}, v, \tilde{p}, \theta, \frac{\partial \theta}{\partial y}, w, \frac{\partial w}{\partial y})^T, \quad (4)$$

which is expressed in the form

$$\Psi = \mathbf{Q}(x_1, y) + h \mathbf{F}_w(x_1, y) \exp(i\alpha_w x + i\beta_w z) + \varepsilon_a \mathbf{F}_a(x_1, y) \exp(i\alpha_a x + i\beta_a z - i\omega t) + \mathbf{F}(x, y, z) \exp(-i\omega t) + (c.c.) \quad (5)$$

The first term of (5) describes the mean flow on a smooth surface; the second term corresponds to the stationary disturbance induced by the wall waviness; the third term corresponds to the acoustic disturbance. Definition of the amplitude ε_a depends on

normalization of the incident acoustic wave. Hereafter the vector-function $\mathbf{F}_a(y)$ is normalized as (pressure amplitude of the incident acoustic wave)=1 at the upper boundary-layer edge, *i.e.* $\varepsilon_a = p_{a,inc}^* / P_e^*$. The fourth term of (5) represent disturbances generated in the boundary layer due to nonlinear interaction of the acoustic wave with the waviness-induced perturbation.

Substituting (5) into Navier-Stokes equations we obtain the following problems written in a matrix-operator form.

For disturbances from wavy wall:

$$H(y, \partial_y, x_1, \omega = 0, \alpha_w, \beta_w) \mathbf{F}_w = 0, \quad (6a)$$

$$F_{w1}(x_1, 0) = -\frac{\partial U}{\partial y}(x_1, 0), \quad F_{w3}(x_1, 0) = 0,$$

$$F_{w5}(x_1, 0) = -\frac{\partial T}{\partial y}(x_1, 0), \quad F_{w7}(x_1, 0) = 0, \quad (6b)$$

$$|\mathbf{F}_w| < \infty, \quad y \rightarrow \infty, \quad (6c)$$

where the boundary conditions (6b) are obtained using the Taylor series expansion of the no-slip conditions, $u = v = w = 0$, and the wall-temperature condition, $\theta = 0$, at $y = y_w$.

For acoustic disturbances:

$$H(y, \partial_y, x_1, \omega, \alpha_a, \beta_a) \mathbf{F}_a = 0, \quad (7a)$$

$$F_{a1} = F_{a3} = F_{a5} = F_{a7} = 0, \quad y = 0, \quad (7b)$$

(pressure amplitude of incident wave)=1, $y \rightarrow \infty$.

For the boundary-layer disturbance:

$$H(y, \partial_y, x_1, \varepsilon \partial_{x_1}, z, \partial_z, \omega) \mathbf{F} = h \varepsilon_a G(y, x_1, \mathbf{F}_w; \omega, \alpha_w, \beta_w, \alpha_a, \beta_a) \mathbf{F}_a \times \exp[i(\alpha_w + \alpha_a)x + i(\beta_w + \beta_a)z], \quad (8a)$$

$$F_1 = F_3 = F_5 = F_7 = 0, \quad y = 0, \quad (8b)$$

$$|\mathbf{F}| < \infty, \quad y \rightarrow \infty. \quad (8c)$$

The right-hand side of (8a) describes bilinear interaction of the wall-induced disturbance with the acoustic wave; the higher order terms $\sim \varepsilon_a^2 h$, $\varepsilon_a h^2$ are neglected. In (6a), (7a) and (8a), the operator H can be expressed in the standard form $H = \frac{\partial}{\partial y} - H_0(y, x_1; R, \omega, \alpha, \beta)$, where the

8×8 matrix H_0 depends on the mean-flow profiles (1) and disturbance parameters.¹⁹

We consider a partial solution of the problem (8a)-(8c) as a decomposition of the discrete

modes $\mathbf{F}_k(x_1, y)$ with the eigenvalues $\alpha_k(x_1, \beta, \omega)$

$$\mathbf{F} = h \varepsilon_a \sum_k [\mathbf{F}_{k0}(x_1, y) + \varepsilon \mathbf{F}_{k1}(x_1, y) + \dots] \times \exp(i \varepsilon^{-1} S_k + i \beta z), \quad (9a)$$

$$S_k = \int \alpha_k(x_1, \omega, \beta) dx_1. \quad (9b)$$

If the nonlinear term of (8a) is not in resonance with the boundary-layer modes, $\alpha_k(x_1, \omega, \beta) \neq \alpha_w + \alpha_a$ and/or $\beta \neq \beta_w + \beta_a$, then receptivity is exponentially weak. In this case, we obtain the eigenvalue problem typical for linear stability analyses

$$\left(\frac{\partial}{\partial y} - H_0 \right) \mathbf{F}_{k0} = 0, \quad (10a)$$

$$(F_{k0})_{1,3,5,7} = 0, \quad y = 0, \quad (10b)$$

$$|\mathbf{F}_{k0}| \rightarrow 0, \quad y \rightarrow \infty. \quad (10c)$$

Solutions of (10) describe the boundary-layer normal waves far from resonance regions. They can be expressed as

$$\mathbf{F}_{k0} = c_k(x_1) \mathbf{A}_k(x_1, y, \alpha_k), \quad (11)$$

where \mathbf{A}_k are eigenfunctions normalized by a certain condition such as $A_{k4}(x_1, 0, \alpha_k) = 1$. The amplitude functions $c_k(x_1)$ are unknown on this stage.

If the nonlinear term is in resonance with one of the normal waves (say with $\alpha = \alpha_n$) at the point $x_1 = x_{10}$,

$$\alpha_n(x_{10}, \omega, \beta) = \alpha_w + \alpha_a \text{ and } \beta = \beta_w + \beta_a, \quad (12)$$

then the acoustic wave effectively generates this normal wave due to the sound-waviness interaction near the resonance point x_{10} .

We consider the case when the normal wave is unstable and the resonance point is close to the lower neutral branch. Analyzing the governing terms of (8a) we conclude that the resonance excitation occurs in the relatively narrow region $|x_1 - x_{10}| = O(\varepsilon^{1/2})$ with the inner variable $\xi = \varepsilon^{-1/2}(x_1 - x_{10}) = O(1)$. We assume that

$$\beta = \beta_w + \beta_a \text{ and } \alpha_w + \alpha_a = \alpha_0 + \gamma \varepsilon^{1/2}, \quad (13)$$

where $\alpha_0 \equiv \alpha_n(x_{10}, \omega, \beta)$; the real parameter γ characterizes resonance detuning. Then, the inner solution of the problem (8a)-(8c) is expressed as

$$\mathbf{F} = \varepsilon_a h [\varepsilon^{-1/2} c(\xi) \mathbf{A}_0(y) + \mathbf{A}_1(\xi, y) \dots] \times \exp(i\varepsilon^{-1/2} \alpha_0 \xi + i\beta z), \quad (14)$$

where $\mathbf{A}_0(y) = \mathbf{A}_n(x_{10}, y, \alpha_0)$ is the normal-wave eigenfunction at the resonance point. Expanding the matrix H_0 in the vicinity of $x = x_{10}$ we obtain the problem for \mathbf{A}_1

$$\left(\frac{\partial}{\partial y} - H_0(x_{10}, \alpha_0) \right) \mathbf{A}_1 = -i \frac{dc}{d\xi} \frac{\partial H_0}{\partial \alpha}(x_{10}, \alpha_0) \mathbf{A}_0 + c\xi \frac{\partial H_0}{\partial x_1}(x_{10}, \alpha_0) \mathbf{A}_0 + G\mathbf{F}_a \exp(i\gamma\xi), \quad (15a)$$

$$(A_1)_{1,3,5,7} = 0, \quad y = 0, \quad (15b)$$

$$|\mathbf{A}_1| \rightarrow 0, \quad y \rightarrow \infty. \quad (15c)$$

This problem is similar to (2.18) of Ref. [17]. It has non-trivial solution if its right-hand side is orthogonal to the eigenfunction $\mathbf{B}_0 = \mathbf{B}_n(x_{10}, y, \alpha_0)$ of the adjoint problem. This condition leads to the equation for $c(\xi)$

$$\frac{dc}{d\xi} - ib\xi c = q \exp(i\gamma\xi), \quad (16a)$$

$$b = \frac{d\alpha_n}{dx_1}(x_{10}), \quad (16b)$$

$$q = \frac{i \langle \mathbf{B}_0, G(x_{10}) \mathbf{F}_a \rangle}{\left\langle \mathbf{B}_0, \frac{\partial H_0}{\partial \alpha}(x_{10}, \alpha_0) \mathbf{A}_0 \right\rangle}, \quad (16c)$$

where the scalar product is defined as

$$\langle \mathbf{B}, \mathbf{A} \rangle = \int_0^8 \bar{B}_j A_j dy, \quad (17)$$

the overbar denotes complex conjugate values. If the normal wave has zero amplitude upstream from the resonance region, then the boundary condition for (16a) is

$$c(\xi) \rightarrow 0, \quad \xi \rightarrow -\infty. \quad (18)$$

The problem (16a)-(18) is similar to the problem (2.19)-(2.21) of Ref. [17]. Using this similarity we obtain the normal-wave amplitude downstream from the resonance region

$$\mathbf{F}_n = \varepsilon_a h \varepsilon^{-1/2} q \sqrt{\frac{2\pi i}{b}} \exp\left(\frac{i\gamma^2}{2b}\right) \mathbf{A}_n(x_1, y) \times \exp\left[i\varepsilon^{-1} \int_{x_{10}}^{x_1} \alpha_n(x_1) dx_1\right], \quad x_1 > x_{10}. \quad (19)$$

This amplitude is proportional to $(L^* / \delta^*)^{1/2} = \varepsilon^{-1/2}$, whereas the resonant region length is $l^* = \varepsilon^{-1/2} \delta^*$. In the parallel flow limit, $\varepsilon \rightarrow 0$, the resonance region is infinitely large and the normal-wave amplitude tends to infinity. In this case, the upper limit of the disturbance amplitude is determined from analysis accounting for nonlinear terms of higher-order. Due to nonparallel effects the receptivity mechanism is local in units of L^* even for distributed roughness. However, it can be treated as a distributed mechanism in units of δ^* . Our choice of the term “distributed receptivity” is a matter of convention.

2.2 Local receptivity on hump

We consider a spanwise row of local humps on a flat plate surface. For brevity we analyze one spanwise harmonic of this periodic structure, and specify its shape as

$$y_w(x, y, z) = hg(x') \exp(i\beta_w z) + (c.c.), \quad (20)$$

$$x' = x - x_0 \equiv \varepsilon^{-1}(x_1 - x_{10}).$$

The shape-function is represented by the Fourier integral

$$g(x') = \frac{1}{2\pi} \int_{-\infty}^{+\infty} \rho(\alpha_w) \exp(i\alpha_w x') d\alpha_w, \quad (21)$$

which can be expressed in the form

$$g = \frac{\varepsilon^{1/2}}{2\pi} \exp(i\alpha_{w0} x') \int_{-\infty}^{+\infty} \rho(\alpha_{w0} + \varepsilon^{1/2} \gamma) e^{i\gamma\xi} d\gamma. \quad (22)$$

Here $\alpha_{w0} = \alpha_n(x_{10}, \omega, \beta) - \alpha_a$ is the wave-number component determined from the resonance condition (12); γ characterizes resonance detuning in accordance with (13). Using (19) for the normal-wave amplitude excited by one harmonic and integrating over γ , we obtain

$$\mathbf{F}_n = \varepsilon_a h q \rho(\alpha_{w0}) \mathbf{A}_n \exp\left(i \int_0^{x'} \alpha_n(x') dx' + i\beta z\right) \quad (23)$$

Note that the function $q(x_{10}, \alpha_0, \alpha_a, \beta_a)$ does not depend on the hump shape $g(x')$. If this function is calculated once and for all, then we can evaluate the normal-wave amplitude for a wall hump of arbitrary shape (within the limit of basic assumptions).

Equation (23) indicates that acoustic waves interacting with a local hump generate normal waves of a finite amplitude even in the parallel mean flow. This is due to the fact that a small portion of the

hump spectrum, $(\alpha_w - \alpha_{w0}) = O(\varepsilon^{1/2})$, is involved into the resonance. As $\varepsilon \rightarrow 0$, the resonant excitation increases as $\varepsilon^{-1/2}$, whereas the active spectral band is narrowed down $\sim \varepsilon^{1/2}$. Because both trends compensate each other, the normal-wave amplitude remains finite.

The relations (19) and (23) hold for any combinations of freestream disturbances and wall perturbations. If we replace the acoustic wave by vortical (entropy) wave, then these expressions provide the normal-wave amplitude generated by vortical (entropy) wave interacting with the surface irregularity. The normal wave can also be of different nature: Tollmien-Schlichting wave, second mode, cross-flow vortices, Görtler vortices *etc.* All these cases can be treated using the following approach:

1. Solve the problem (6a)-(6c) for wall-induced disturbance
2. Solve the problem (7a)-(7c) for external (freestream) disturbance
3. Solve the eigenvalue problem (10a)-(10c) and the adjoint problem to obtain the eigenfunctions $\mathbf{A}_n(x_1, y)$ and $\mathbf{B}_n(x_1, y)$
4. Evaluate the scalar products of (16c)
5. Predict the normal-wave amplitude using (19) for distributed receptivity or (23) for local receptivity

This algorithm can be incorporated into a computational module, which may be linked with a standard linear stability solver.

2.3 Receptivity near spectrum branch points

Foregoing analysis is valid for “simple” discrete spectrums; *i.e.* the eigenvalues of boundary-layer modes are assumed to be essentially different. This is typical for boundary layers at subsonic and moderate supersonic speeds as well as hypersonic boundary layers on adiabatic walls. However, in the case of low wall temperature ratios, the first and second modes have the branch points, which are close to the real parameter space.^{17,21,22} The upstream branch point, $x_1 = x_{1b}$, is located near the lower neutral branch of the second mode whereas the downstream branch point is close to the upper neutral branch. In the branch-point vicinity (say for the upstream point x_{1b}), the eigenvalues behave as^{17,22}

$$\alpha_{1,2} = \alpha_b \pm i\lambda\sqrt{x_1 - x_{1b}} + \dots, \quad (24)$$

where $\alpha_b \equiv \alpha_1(x_{1b}, \omega) = \alpha_2(x_{1b}, \omega)$.

The receptivity factor q given by (16c) tends to infinity as the resonance point tends to the branch point, since the scalar product

$$\left\langle \frac{\partial H_0}{\partial \alpha}(x_{10}, \alpha_0) \mathbf{A}_0, \mathbf{B}_0 \right\rangle \rightarrow 0, \quad x_{10} \rightarrow x_{b1}. \quad (25)$$

Moreover, the eigenvalue derivative in (19) for distributed receptivity behaves as

$$b = \frac{d\alpha_n}{dx_1}(x_{10}) \rightarrow \infty, \quad x_{10} \rightarrow x_{b1}. \quad (26)$$

This singularity was analyzed in Ref. [17] for the case of receptivity to wall-induced perturbations. Since the analysis¹⁷ is easily extended to the problem considered herein, we briefly outline key points of this extension for the case of two-dimensional disturbances ($\beta = 0$).

Near the branch point, one discrete mode (say Mode 1 of the eigenvalue $\alpha_1(x_1, \omega)$) strongly interacts with another (say Mode 2 of the eigenvalue $\alpha_2(x_1, \omega)$). This interaction can be described by the two-mode approximation

$$\begin{aligned} \mathbf{F}(x_1, y) &= c_1(x_1) \mathbf{A}_1(x_1, y) \exp(\varepsilon^{-1} i S_1) + \\ &+ c_2(x_1) \mathbf{A}_2(x_1, y) \exp(\varepsilon^{-1} i S_2). \end{aligned} \quad (27)$$

Far from the resonance regions, the amplitude coefficients $c_{1,2}(x_1)$ are solutions of the problem

$$\frac{dc_1}{dx_1} = c_1 W_{11} + c_2 W_{12} \exp[\varepsilon^{-1} i(S_2 - S_1)], \quad (28a)$$

$$\frac{dc_2}{dx_1} = c_2 W_{22} + c_1 W_{21} \exp[\varepsilon^{-1} i(S_1 - S_2)], \quad (28b)$$

$$c_1(x_{1s}) = c_{1s}, \quad c_2(x_{1s}) = c_{2s}. \quad (28c)$$

Here c_{1s} and c_{2s} are specified at a certain initial point x_{1s} ; the matrix elements are

$$W_{jk} = - \frac{\left\langle \mathbf{B}_j, \frac{\partial H_0}{\partial \alpha} \frac{\partial \mathbf{A}_k}{\partial x_1} \right\rangle + i \left\langle \mathbf{B}_j, H_1 \frac{\partial \mathbf{A}_k}{\partial x_1} \right\rangle}{\left\langle \mathbf{B}_j, \frac{\partial H_0}{\partial \alpha} \frac{\partial \mathbf{A}_j}{\partial x_1} \right\rangle}, \quad (29)$$

where $j=1,2$ $k=1,2$; H_1 depends on the mean-flow derivatives $\partial U / \partial x_1$, $\partial T / \partial x_1$ and the vertical

velocity V_0 . Near the branch point, the matrix elements (29) behave as

$$W_{jk} \rightarrow \frac{(-1)^{j+k-1}}{4(x_1 - x_{1b})}, \quad x_1 \rightarrow x_{1b}. \quad (30)$$

This leads to the following singularity of the amplitude coefficients

$$c_{1,2}(x_1) = \frac{C_{1,2}}{(x_1 - x_{1b})^{1/4}} + \dots, \quad x_1 \rightarrow x_{1b}, \quad (31)$$

where constants $C_{1,2}$ depend on normalization of the eigenfunctions $\mathbf{A}_{1,2}(x_1, y)$.

In the inner region $x_1 - x_{1b} = O(\varepsilon^{2/3})$, the mode decomposition (27) is replaced by the local expansion with the variable $\zeta = \varepsilon^{-2/3}(x_1 - x_{1b})$

$$\mathbf{F} = \varepsilon^{-1/6} [c_0(\zeta)\mathbf{A}_0(y) + \varepsilon^{-1/3}c_{01}(\zeta)\mathbf{A}_{01}(y) + \dots] \times \exp(i\varepsilon^{-1}S_b + i\varepsilon^{-1/3}\alpha_b\zeta), \quad (32)$$

where $c_0(\zeta)$ is solution of Airy equation

$$\frac{d^2 c_0}{d\zeta^2} - \lambda^2 \zeta c_0 = 0. \quad (33)$$

Matching the inner and outer solutions we can establish an exchange rule in the branch-point vicinity.^{21,22} The local expansion (32) indicates that the disturbance amplitude has a peak $\sim \varepsilon^{-1/6}$ in the inner region $\zeta = O(1)$. To separate this effect from the receptivity mechanism we need to establish a relationship between the coefficients $C_{1,2}$ (instead of the amplitude functions $c_{1,2}(x_1)$) and characteristics of the incident acoustic wave plus the wall disturbance.

Wavy wall

In the case of acoustic waves interacting with the wall waviness, the normal-wave amplitude is expressed as

$$\mathbf{F}_n = \varepsilon_a h \varepsilon^{-1/2} \frac{\sqrt{\pi\lambda}}{(x_{10} - x_{1b})^{1/4}} \frac{\langle \mathbf{B}_0, G(x_{10}) \mathbf{F}_a \rangle}{\left\langle \mathbf{B}_0, \frac{\partial H_0}{\partial x_1}(x_{10}, \alpha_0) \mathbf{A}_0 \right\rangle} \times \mathbf{A}_n(x_1, y) \exp \left[i\varepsilon^{-1} \int_{x_{10}}^{x_1} \alpha_n(x_1) dx_1 \right], \quad x_1 > x_{10}, \quad (34)$$

Then, the local amplitude coefficient is

$$C_n = \varepsilon_a h \varepsilon^{-1/2} \sqrt{\pi\lambda} \frac{\langle \mathbf{B}_0, G(x_{10}) \mathbf{F}_a \rangle}{\left\langle \mathbf{B}_0, \frac{\partial H_0}{\partial x_1}(x_{1b}, \alpha_b) \mathbf{A}_0 \right\rangle}. \quad (35)$$

The relation (35) indicates that distributed receptivity has no singularity at the spectrum branch point. In accordance with (31) the disturbance peak is totally due to singular behavior of the normal wave itself. If we measure the disturbance amplitude Q_n at a fixed point downstream from the branch point for various locations of the resonant point x_{10} , then we do not observe significant changes in the distribution $Q_n(x_{10})$ near the point $x_{10} = x_{1b}$. This conclusion is similar to that formulated in Ref. [17] for receptivity to wall-induced disturbances.

Local hump

If a local hump is far from the branch point, then the normal-wave amplitude is determined from (23). As the hump approaches the branch point, $x_{10} \rightarrow x_{1b}$, the receptivity factor behaves as

$$q \rightarrow \frac{\langle \mathbf{B}_0, G(x_{10}) \mathbf{F}_a \rangle}{\left\langle \mathbf{B}_0, \frac{\partial H_0}{\partial x_1}(x_{10}, \alpha_0) \mathbf{A}_0 \right\rangle} \frac{\lambda \rho(\alpha_0)}{2(x_{10} - x_{1b})^{1/2}}. \quad (36)$$

Then, the amplitude coefficient from (31) is expressed as

$$C_n = \frac{\varepsilon_a h \lambda \rho(\alpha_0)}{2(x_{10} - x_{1b})^{1/4}} \frac{\langle \mathbf{B}_0, G(x_{10}) \mathbf{F}_a \rangle}{\left\langle \mathbf{B}_0, \frac{\partial H_0}{\partial x_1}(x_{10}, \alpha_0) \mathbf{A}_0 \right\rangle}. \quad (37)$$

Local receptivity increases proportionally to $(x_{10} - x_{1b})^{-1/4}$ as the hump approaches the branch point. This effect is due to increasing of the active wavenumber range of the hump spectrum. If the hump center x_{10} is far from the branch point, then this range is estimated as $\alpha_w + \alpha_a - \alpha_0 = O(\varepsilon^{1/2})$. If $x_{10} - x_{1b} = O(\varepsilon^{2/3})$, then $\alpha_w + \alpha_a - \alpha_0 = O(\varepsilon^{1/3})$ and the amplitude coefficient is $C_n = O(\varepsilon_a h \varepsilon^{-1/6})$.

Matching of the inner solution (32) with the outer solution gives the normal-wave amplitude

$$\mathbf{F}_n = \varepsilon_a h \varepsilon^{-1/6} \frac{\lambda \rho(\alpha_b) \Gamma(1/3)}{2\sqrt{\pi}(x_1 - x_{1b})^{1/4}} \left(\frac{\lambda}{3} \right)^{1/6} \times \frac{\langle \mathbf{B}_b, G(x_{1b}) \mathbf{F}_a \rangle}{\left\langle \mathbf{B}_b, \frac{\partial H_0}{\partial x_1} \mathbf{A}_b \right\rangle_b} \mathbf{A}_n(x_1, y) \exp \left(i\varepsilon^{-1} \int_{x_{10}}^{x_1} \alpha_n(x_1) dx_1 \right) \quad (38)$$

where $\varepsilon^{2/3} \ll x_1 - x_{1b} \ll 1$; the subscript “b” denotes quantities at $x_1 = x_{1b}$; the Gamma-function $\Gamma(1/3) = 2.678938\dots$. From (38) and (31) we obtain the amplitude coefficient

$$C_n = \varepsilon_a h \left(\frac{\lambda}{3\varepsilon} \right)^{1/6} \frac{\lambda \rho(\alpha_b) \Gamma(1/3)}{2\sqrt{\pi}} \frac{\langle \mathbf{B}, G\mathbf{F}_a \rangle_b}{\left\langle \mathbf{B}, \frac{\partial H_0}{\partial x_1} \mathbf{A} \right\rangle_b} \quad (39)$$

Summarizing we conclude that local receptivity strongly depends on the distance between the hump and the branch point. As $x_{10} \rightarrow x_{1b}$, the amplitude coefficient $C_n \sim |x_{10} - x_{1b}|^{-1/4}$ and attains its maximum $\sim \varepsilon_a h \varepsilon^{-1/6}$ at $x_{10} = x_{1b}$. If we measure the disturbance amplitude Q_n at a certain fixed point downstream from the branch point for various hump locations, then we observe a local peak of $Q_n(x_{10})$ in the vicinity of $x_{10} = x_{1b}$. Again this result is consistent with that obtained in Ref. [17] for receptivity to wall-induced disturbances.

3. Numerical results

Receptivity calculations were conducted for the boundary layer on a flat plate at $M = 6$, stagnation temperature $T_0^* = 390^\circ \text{F}$ and the wall temperature $T_w^* = 80^\circ \text{F}$ that corresponds to the wall temperature ratio $T_w^*/T_0^* = 0.6356$. This case is a good candidate for wind tunnel experiments at Mach 6. The fluid is a perfect gas with the specific heats ratio $\gamma = 1.4$ and Prandtl number $\text{Pr} = 0.72$. The viscosity-temperature dependency is given by Sutherland’s law

$$\mu(T) = \frac{(1+S)}{(T+S)} T^{3/2}, \quad (40)$$

where $S = 110/T_e^*$ for air temperature measured in Kelvin degrees; $\mu = \mu^*/\mu_e^*$ is nondimensional viscosity. Hereafter the global length scale is $L^* = x^*$; the boundary-layer scale is $\delta^* = \sqrt{\nu_e^* x^*/U_e^*}$, and the Reynolds number is $R = \sqrt{U_e^* x^*/\nu_e^*}$.

Effects of hypersonic viscous-inviscid interaction are neglected; *i.e.*, mean flow characteristics at the upper boundary-layer edge

coincide with freestream characteristics. The boundary-layer flow is approximated by the self-similar profiles $U(y)$, $T(y)$, with $y = y^*/\sqrt{\nu_e^* x^*/U_e^*}$. The boundary-layer thickness is $\Delta^* = 16.73\sqrt{\nu_e^* x^*/U_e^*}$ and the displacement thickness is $\Delta_d^* = 13.64\sqrt{\nu_e^* x^*/U_e^*}$.

The second-mode eigenvalues, $\alpha_2(R)$, are shown in Fig. 2 for various frequency parameters $F = \omega^* \nu_e^*/U_e^{*2}$. Figures 3 and 4 illustrate the phase-speed distributions $c_2(R) = \omega/\alpha_2$ and the branch-point loci, respectively. Local maximums (minimums) of $c_2(R)$ correlate with the upstream (downstream) branch points. The latter are close to the neutral branches of the second mode. The upstream branch points are below the real axis of complex R , whereas the downstream branch points are above this axis. In what follows, we assume that the branch-point influence domains are far enough from the real axis. Then we can use the theoretical model of Section 2 relevant to the simple discrete spectrum.

Distributions of the pressure amplitude, $p_2(y) = \gamma M^2 |A_{24}(y)|$, and the streamwise mass-flow amplitude,

$$f_2(y) = \left| A_{21} + \left(\gamma M^2 A_{24} - \frac{A_{25}}{T} \right) U \right| \frac{1}{T}, \quad (41)$$

are shown in Fig. 5 for $F = 8 \times 10^{-5}$ and $R = 1000$ (near the lower neutral branch). The eigenfunction is normalized as $p_2(0) = 1$. The mass-flow amplitude has a typical sharp maximum in the critical layer located slightly below the upper boundary-layer edge.

3.1 Waviness-induced perturbations

The pressure distributions $\text{Re}[p_w(y)] = \gamma M^2 \text{Re}[F_{w4}(y)]$ are shown in Fig. 6 for the Reynolds number $R = 1000$ and the wave numbers $\alpha_w = 0.001, 0.05, 0.1$. The major portion of boundary layer is weakly perturbed. The first maximum of pressure fluctuations is located near the upper boundary-layer edge. The disturbance amplitude in the external flow is essentially higher than that within the boundary layer.

Distributions of the mass flow $\text{Re}[f_w(y)]$ are shown in Fig. 7. Similar to the case of pressure disturbances, the mass-flow amplitude outside the boundary layer is essentially higher than that within the boundary layer.

3.2 Acoustic waves

In a supersonic uniform flow, it is possible to generate slow and fast acoustic waves with the phase speeds $c_a \leq 1 - 1/M$ and $c_a \geq 1 + 1/M$, respectively. It is convenient to express the acoustic wavenumber as a function of the angle of incidence Θ . For slow waves:

$$\alpha_a = \frac{\omega M \cos \Theta}{M \cos \Theta - 1}, \quad c_a \equiv \frac{\omega}{\alpha_a} = 1 - \frac{1}{M \cos \Theta}, \quad (42)$$

$$0 < \Theta < \Theta_{cr} \equiv \arccos(1/M),$$

For fast waves:

$$\alpha_a = \frac{\omega M \cos \Theta}{M \cos \Theta + 1}, \quad c_a = 1 + \frac{1}{M \cos \Theta}, \quad (43)$$

$$0 < \Theta < \pi/2.$$

In all figures presented hereafter, Θ is measured in degrees.

A good insight into interactions of acoustic waves with a hypersonic boundary layer is provided by the short-wave approximation.^{19,20} Schematic picture of the disturbance field is shown in Fig. 8 for slow waves with the phase speed $a(0) < c_a < U_e - a_e$, where $a(y)$ is local speed of sound. In the lower wave-guide, acoustic rays are reflected by the wall and refracted near the lower sonic line, $U(y) = c_a - a(y)$. In the upper half-space, incident acoustic waves are refracted near the upper sonic line, $U(y) = c_a + a(y)$. In the quiet zone between the sonic lines, the disturbance amplitude is relatively small.

Slow waves

Slow acoustic waves were calculated at frequency $F = 8 \times 10^{-5}$ and Reynolds number $R = 1000$. The critical angle of incidence is $\Theta_{cr} = 80.4^\circ$ at the Mach number $M = 6$. Figure 9 shows contours of the pressure amplitude $|p_a(y, \Theta)|$. Figure 10 represents the function $|p_a(y)|$ at various angles of incidence. Pressure waves weakly penetrate into the boundary layer because its major portion is covered by the quiet zone (see Fig. 10). Due to interference between reflected and incident waves, the pressure amplitude oscillates from 0 to approximately 2 outside the boundary layer. This indicates that the reflection coefficient is ≈ 1 ; *i.e.*, the boundary layer is passive with respect to pressure waves. A flat maximum of the pressure

amplitude is observed in the boundary layer at $\Theta \approx 40^\circ$. As $\Theta \rightarrow \Theta_{cr}$, the disturbance wavelength decreases, the phase speed $c_a \rightarrow 0$. The upper sonic line moves toward the wall allowing pressure waves to penetrate deeper into the boundary layer.

The contours of mass-flow $|f_a(y, \Theta)|$ and the functions $|f_a(y)|$ are shown in Figs. 11 and 12 for various angles of incidence. As contrasted to the pressure wave, the mass-flow disturbance has a sharp peak near the upper boundary-layer edge. Its maximum is observed at $\Theta \approx 40^\circ$. This peak overlaps with the second-mode peak located in the critical-layer (Fig. 5). Such an overlapping may increase the scalar product $\langle G(x_{10}) \mathbf{F}_a, \mathbf{B}_0 \rangle$ and enhance receptivity.

Fast waves

Characteristics of fast acoustic waves were calculated at the same frequency $F = 8 \times 10^{-5}$ and Reynolds number $R = 1000$. The pressure amplitude distributions are shown in Figs. 13, 14. These waves have no sonic lines because their phase speed is $c_a > 1 + 1/M$. Acoustic rays easily penetrate into the boundary layer that changes the pressure amplitude pattern (compare Figs. 9 and 13). The maximum of $|p_a(y)|$ is observed near the wall at the angle of incidence $\Theta \approx 50^\circ$.

The contours of mass-flow $|f_a(y, \Theta)|$ and the functions $|f_a(y)|$ are shown in Figs. 15 and 16. The mass-flow amplitude has a peak near the upper boundary-layer edge. It is higher and sharper than in the case of slow acoustic waves (compare Figs. 12 and 16).

Foregoing numerical examples indicate that hypersonic boundary layer is more sensitive to fast acoustic waves. This is consistent with the acoustic field topology predicted by the short-wave theory (Fig. 8). On the other hand, the slow-wave phase speed is closer to the second-mode phase speed that is more preferable for receptivity. The latter argument is important for the case of smooth surfaces. However, it is less critical for receptivity to sound plus wall roughness, because the roughness shape can be always tuned to meet the synchronization condition (12).

Small angles of incidence

Figures 9, 11 (for slow waves) and Figures 13, 15 (for fast waves) show that the disturbance amplitude decreases rapidly as the angle of incidence tends to zero ($c_a \rightarrow 1 \pm 1/M$). This is due to the fact that the

reflected acoustic wave is almost in counter-phase with the incident wave and they cancel each other within the boundary layer. The limit $\Theta \rightarrow 0$ needs special treatment because the length scale l_y^* of the amplitude variation in the vertical direction tends to infinity. According to Ref. [21] nonparallel effects can change the acoustic field substantially if $l_y^* / \Delta_d^* = O(\Delta_d F^{1/2})$ (in the case considered, the nondimensional displacement thickness is $\Delta_d \approx 14$). Using (42) we conclude that the local-parallel approximation is not valid for $\Theta \leq O(\Delta_d F^{1/2})$. For disturbances of the frequency $F = 8 \times 10^{-5}$, this occurs at $\Theta \leq 7^\circ$.

The asymptotic analysis²¹ showed that the boundary layer growth (nonparallel effect) causes diffraction of incident acoustic waves. The latter leads to decreasing of the acoustic-wave amplitude at the upper boundary-layer edge in downstream direction. For acoustic sources fixed in space, the major portion of the plate surface is radiated by waves of small Θ . Then, diffraction and counter-phase interference can essentially reduce the sound amplitude in the boundary layer. This, in turn, reduces the normal-wave excitation due to sound-roughness interaction far downstream from the leading edge. However, in many practical cases, acoustic waves are generated by convective sources. Their angles of incidence are not small. For example, Laufer²³ showed that the turbulent boundary layer on wind-tunnel walls predominantly radiated acoustic waves with $\Theta > 45^\circ$.

These arguments indicate that receptivity experiments should cover a wide range of angles of incidence. Special techniques need to be developed to simulate acoustic field from convective sources.

3.3 Distributed receptivity on wavy surface

Using (19) we express the initial amplitude of the second-mode wave generated by the wavy wall in the resonance region as

$$|p_2(x_{10}, 0)| = \varepsilon_a h G_{p,dis}(x_{10}, \omega, \alpha_a), \quad (44)$$

where $|p_2(x_{10}, 0)|$ is pressure amplitude on the wall surface. The receptivity function is

$$G_{p,dis} = \varepsilon^{-1/2} \left| q \sqrt{\frac{2\pi i}{b}} \gamma M^2 A_{24}(x_{10}, 0) \right|, \quad (45)$$

The vector-function \mathbf{F}_a is normalized by the condition: (pressure amplitude of the incident wave at the upper boundary-layer edge)=1; i.e. $\varepsilon_a = p_{inc}^* / P_e^*$ at $y = y_e$. The nondimensional amplitude of the wavy wall is $h = h^* / \sqrt{\nu_e^* x_0^* / U_e^*}$, where x_0^* is the resonance point. The receptivity function $G_{p,dis}$ depends on the frequency parameter F , the Reynolds number $R = \sqrt{U_e^* x_0^*} / \nu_e^*$ and the acoustic-wave incident angle Θ . Because $|\text{Im}(\alpha_2)| \ll |\text{Re}(\alpha_2)|$ for all parameters under consideration, the resonance condition (12) is approximated as

$$\alpha_w = \alpha_2(x_{10}, \omega) - \alpha_a \approx \text{Re}[\alpha_2(x_{10}, \omega) - \alpha_a]. \quad (46)$$

Calculations of $G_{p,dis}$ were performed for slow and fast acoustic waves of the frequency $F = 8 \times 10^{-5}$ in the Reynolds number ranges relevant to the second-mode instability.

Slow acoustic waves

For α_a given by (42), the receptivity function $G_{p,dis}(\Theta, R)$ is shown in Fig. 17. This function is highly non-uniform with respect to the Reynolds number. It has two sharp maximums near the lower and upper neutral branches. Similar to the case of wall-induced disturbances,¹⁷ these maximums correlate with the spectrum branch points shown in Fig. 4. The first maximum is of the most interest, since it corresponds to the initial stage of instability. It is observed at relatively high angles of incidence, $\Theta \approx 65^\circ$. Receptivity to acoustic waves of small Θ is on the order of magnitude lower. This is consistent with the fact that such acoustic waves weakly penetrate into the boundary layer (see Section 3.2).

Fast acoustic waves

For α_a given by (43), the receptivity function $G_{p,dis}(\Theta, R)$ is shown in Fig. 18. Comparing Figs. 17 and 18 we conclude that receptivity to the fast acoustic waves is higher than that to the slow waves. This agrees with the fact that the fast-wave amplitude is relatively large in the boundary layer (see Section 3.2). The first and second maximums of $G_{p,dis}$ merge into a dome covering the unstable range of Reynolds numbers. The receptivity maximum is located at $\Theta \approx 45^\circ$. As the angle of incidence tends to zero, the receptivity function decreases rapidly. Similar features were observed at other frequencies of the range $F = (4-10) \times 10^{-5}$.

3.4 Local receptivity on hump

Using (23) we can express the second-mode amplitude generated by acoustic waves on a local hump as

$$|p_2(x_{10}, 0)| = \varepsilon_a h G_{p,loc}(x_{10}, \omega, \alpha_a) |\rho(\alpha_{w0})|, \quad (47)$$

$$G_{p,loc} = |q \gamma M^2 A_{24}(x_{10}, 0)|, \quad (48)$$

$$\rho(\alpha_w) = \int_{-\infty}^{+\infty} g(x') \exp(-i\alpha_w x') dx'. \quad (49)$$

Here q is given by (16c); the resonance wavenumber α_{w0} is approximated by (46). Similar to the case of receptivity on a wavy wall, $G_{p,loc}$ is a function of the frequency parameter F , the Reynolds number $R = \sqrt{U_e^* x_0^* / \nu_e^*}$ based on the hump center x_0^* , and the acoustic-wave incident angle Θ . The distribution of $G_{p,loc}(\Theta, R)$ is shown in Fig. 19 for slow acoustic waves and in Fig. 20 for fast waves. Comparing these functions with the case of distributed receptivity (Figs. 17 and 18) we conclude that the local receptivity is much weaker than the distributed one, $G_{p,loc} \approx 10^{-2} G_{p,dis}$. Nevertheless, qualitative behaviors of $G_{p,loc}$ and $G_{p,dis}$ are similar. This is due to the fact that the ratio,

$$\frac{G_{p,dis}}{G_{p,loc}} = \varepsilon^{-1/2} \left| \frac{2\pi i}{(d\alpha_2/dx_1)_{x_1=x_{10}}} \right|, \quad (50)$$

does not depend on characteristics of acoustic wave and roughness.

In the cases considered, the eigenvalue derivative $d\alpha_2/dx_1$ is a regular function of x_1 because the spectrum branch points are essentially complex (see Fig. 4). The ratio (50) is a smooth function of the streamwise coordinate x_{10} or, what is the same, the Reynolds number R . However, for hypersonic boundary layers on a cooled wall,^{17,22} the branch points may cross the real axis. Since the eigenvalue derivative tends to $\pm\infty$ in the branch-point vicinity (see (24)), the local behaviors of $G_{p,dis}$ and $G_{p,loc}$ are different. In this case, one needs to use the receptivity model of Section 2.3.

4. Summary discussion

In this paper, the receptivity model¹⁷ for wall-induced perturbations is extended to the case of

acoustic waves interacting with surface roughness. We considered the second-mode excitation on a wavy wall (distributed roughness) or a hump (local roughness element). This problem includes the following components:

- (a) Stationary disturbances generated by surface roughness
- (b) Acoustic disturbances
- (c) Disturbances resulted from the bilinear interaction of the roughness-induced disturbance with the acoustic wave

It was shown that the receptivity mechanism depends on the discrete spectrum topology. If this spectrum is simple (its branch points are far from the real parameter space), then receptivity reveals the following features:

- For distributed roughness (wavy wall), a strong excitation of the normal waves occurs in the local region of the length $l^* = R^{-1/2} L^* = R^{1/2} \delta^*$, where the component (c) is in resonance with the second-mode wave. In this region, the normal-wave amplitude is $\sim (L^* / \delta^*)^{1/2}$. The relative length of the resonance region, l^* / δ^* , increases with the Reynolds number. As $R \rightarrow \infty$, the normal-wave amplitude tends to infinity. Its upper bound is associated with nonlinear effects of higher-order approximations.
- For local roughness, the normal-wave amplitude is finite even in the parallel flow limit. In this case, only a small portion of roughness spectrum, $(\alpha_w - \alpha_{w0}) = O(R^{-1/2})$, is involved into the resonance. As $R \rightarrow \infty$, the resonant excitation increases $\sim R^{1/2}$, whereas the active spectral band is narrowed down $\sim R^{-1/2}$. Because both trends compensate each other, the normal-wave amplitude tends to a finite value.

If the branch-point influence domain overlaps with the real parameter space, then propagation and/or excitation of normal waves are singular. Asymptotic analysis of this singularity shows:

- The second-mode excitation on a wavy wall (distributed roughness) is not singular at the branch point. The amplitude peak is totally due to a singular behavior of the normal wave itself. If we measure the disturbance amplitude Q at a fixed point downstream from the branch point x_{1b} for various loci of the resonance point x_{10} , then

we do not observe substantial changes in the distribution $Q(x_{10})$ near the point $x_{10} = x_{1b}$.

- The second-mode excitation over a local hump strongly depends on the distance between the hump center x_{10} and the branch point x_{1b} . As $x_{10} \rightarrow x_{1b}$, the normal-wave amplitude increases $\sim |x_{10} - x_{1b}|^{-1/4}$ and attains its maximum value $\sim \varepsilon_a h \varepsilon^{-1/6}$ at $x_{10} = x_{1b}$. If we measure the disturbance amplitude Q at a fixed point downstream from the branch point for various loci of the hump center, then we observe a local peak of $Q(x_{10})$ in the vicinity of $x_{10} = x_{1b}$.

Numerical examples were presented for two-dimensional disturbances interacting with the boundary layer on a flat plate with adiabatic wall at the Mach number $M = 6$. In this case, the spectrum branch points are essentially complex that allows us to calculate the receptivity coefficients assuming that the disturbance spectrum is simple. Results of these calculations are summarized as follows:

1. In the boundary layer, the pressure amplitude of fast acoustic waves is larger than that of slow waves. The amplitude maximum is observed at the angle of incidence $\Theta \approx 40^\circ$ for slow waves and $\Theta \approx 45^\circ$ for fast waves. Due to counter-phase interference between the incident and reflected waves, the disturbance amplitude decreases rapidly as $\Theta \rightarrow 0$.
2. *On wavy-wall*, the receptivity coefficient is highly non-uniform with respect to the Reynolds number $R = \sqrt{U_e^* x_0^* / \nu_e^*}$.
- For slow acoustic waves, the receptivity coefficient has two maximums, which are close to the lower and upper neutral branches. Loci of these maximums correlate with the spectrum branch points. The boundary layer is most receptive to acoustic waves of relatively high angles of incidence: $\Theta \approx 65^\circ$ near the first maximum and $\Theta \approx 40^\circ$ near the second maximum.
- For fast acoustic waves, the receptivity maximums merge into a dome covering the instability region. The boundary layer is most receptive to acoustic waves of $\Theta \approx 45^\circ$.
- The receptivity coefficients for both slow and fast acoustic waves of small angles of incidence are on the order of magnitude smaller of their maximal values.
3. *On local hump*, the receptivity coefficient has the same qualitative behavior as in the wavy-wall case. However its quantity is essentially smaller: $G_{p,loc} \approx 10^{-2} G_{p,dis}$.

Acknowledgments

The author would like to thank Dr. Roger Kimmel for coordination of this effort. The work was sponsored by the European Office of Aerospace Research and Development (EOARD) under Special Program Contract SPC 98-4071. Further theoretical studies of this problem are supported by EOARD (the ISTC Project 2393).

References

- ¹Aizin, L.B., and Polyakov, M.F., "Acoustic Generation of Tollmien-Schlichting Waves over Local Unevenness of Surface Immersed in Stream," Preprint No. 17, SO AN SSSR, Institute of Theoretical and Applied Mechanics, Novosibirsk, 1979 (in Russian).
- ²Fedorov, A.V., "Excitation and Development of Unstable Disturbances in Compressible Boundary Layer," Ph.D. Dissertation, Moscow Institute of Physics and Technology, 1982 (in Russian).
- ³Zavol'skii, N.A., Reutov, V.P., Rybushkina, G.V., "Excitation of Tollmien-Schlichting Waves by Acoustic and Vortex Disturbance Scattering in Boundary Layer on a Wavy Surface," *J. Appl. Mech. Tech. Phys.*, Vol. 24, pp. 355-361, 1983.
- ⁴Zhigulev, V.N., and Fedorov, A.V., "Boundary Layer Receptivity to Acoustic Disturbances," *J. Appl. Mech. And Tech. Phys.*, Vol. 28, pp. 28-34, 1987.
- ⁵Zhigulev, V.N., and Tumin, A.M., *Onset of Turbulence*, Nauka, Novosibirsk, 1987.
- ⁶Goldstein, M.E., "Scattering of Acoustic Waves into Tollmien-Schlichting Waves by Small Streamwise Variations in Surface Geometry," *J. Fluid Mech.*, Vol. 154, p. 509, 1985.
- ⁷Ruban, A.I., "On the Generation of Tollmien-Schlichting Waves by Sound," *Fluid Dyn.*, Vol. 19, p. 709, 1985.
- ⁸Goldstein, M.E., and Hultgren, L.S., "Boundary-Layer Receptivity to Long-Wave Free-Stream Disturbances," *Annu. Rev. Fluid Mech.*, Vol. 21, p. 137, 1989.
- ⁹Nishioka, M., and Morkovin, M.V., "Boundary-Layer Receptivity to Unsteady Pressure Gradients:

Experiments and Overview,” *J. Fluid Mech.*, Vol. 171, p. 219, 1989.

¹⁰Kerschen, E.J., “Boundary Layer Receptivity Theory,” AIAA Paper No. 89-1109, 1989.

¹¹Wiegel, M., and Wlezein, R.W., “Acoustic Receptivity of Laminar Boundary Layers over Wavy Walls,” AIAA Paper No. 93-3280, 1993.

¹²Choudhari, M., Street, C.L., “A Finite Reynolds-Number Approach for the Prediction of Boundary-Layer Receptivity in Localized Regions,” *Phys. Fluids*, A Vol. 4 (11), pp. 2495-2514, 1992.

¹³Choudhari, M., Street, C.L., “Theoretical Prediction of Boundary-Layer Receptivity,” AIAA Paper No. 94-2223, 1994.

¹⁴Crouch, J.D., “Theoretical Studies on the Receptivity of Boundary Layers,” AIAA Paper No. 94-2224, 1994.

¹⁵Saric, W.S., Hoos, J.A., and Radeztsky, R.H., “Boundary-Layer Receptivity of Sound with Roughness,” in: *Boundary Layer Stability and Transition to Turbulence*, ASME FED-Vol. 114, pp. 17-22, 1991.

¹⁶Choudhari, M., and Street, C., *Boundary Layer Receptivity Phenomena in Three-Dimensional and High-Speed Boundary Layers*, AIAA Paper No. 90-5258, 1990.

¹⁷Fedorov, A.V., and Khokhlov, A.P., “Receptivity of Hypersonic Boundary Layer to Wall Disturbances,” *Theoretical and Computational Fluid Dynamics*, Vol. 15, No. 4, pp. 231-254, 2002.

¹⁸Bogolepov, V.V., and Neiland, V.Ya., “Viscous Flow over Small Irregularities on Supersonic Body Surface,” *Trudy TsAGI*, vyp. 1363, 1971.

¹⁹Mack, L.M., “Boundary-Layer Stability Theory,” JPL Rep. No. 900-277, Rev. B, Pasadena, California, 1969.

²⁰Guschin V.R., and Fedorov, A.V., “Asymptotic Analysis of Inviscid Perturbations in a Supersonic Boundary Layer,” *Zhurnal Prikl. Mekh. I Tekh. Fiz.*, No. 1, pp. 69-75, 1989 (translated in English).

²¹Fedorov, A.V., and Khokhlov, A.P., “Excitation and Evolution of Unstable Disturbances in Supersonic Boundary Layers,” in: *Transitional and Turbulent Compressible Flows*, ASME Vol. 151, pp. 1-13, 1993.

²²Fedorov, A.V., and Khokhlov, A.P., “Prehistory of Instability in a Hypersonic Boundary Layer,” *Theoretical and Computational Fluid Dynamics*, Vol. 14, No. 6, pp. 359-375, 2001.

²³Laufer, J., “Some Statistical Properties of the Pressure Field Radiated by a Turbulent Boundary Layer,” *Phys. Fluids*, Vol. 7, pp. 1191-1197, 1964.

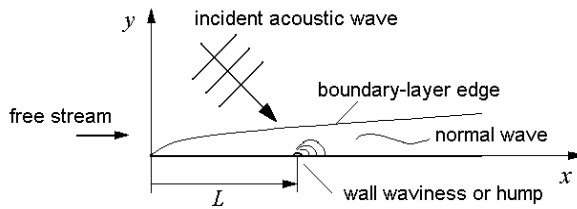


Fig. 1 Flow scheme.

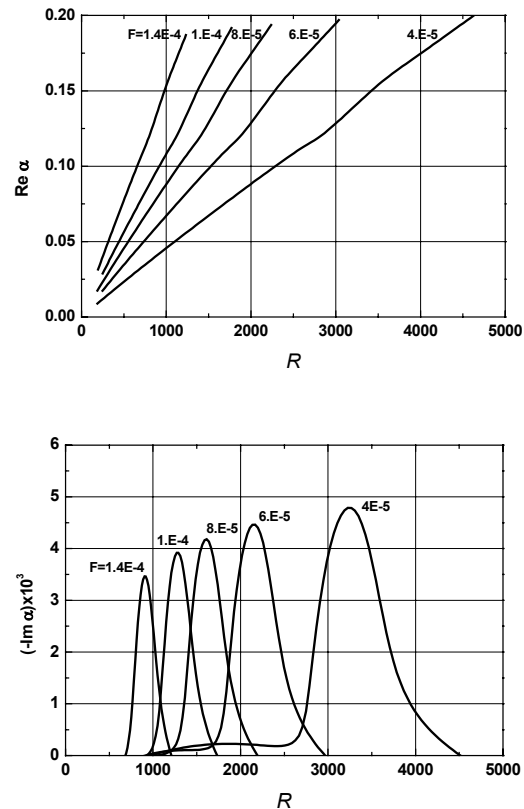


Fig. 2 Second-mode eigenvalues α_2 as a function of Reynolds number at various frequencies.

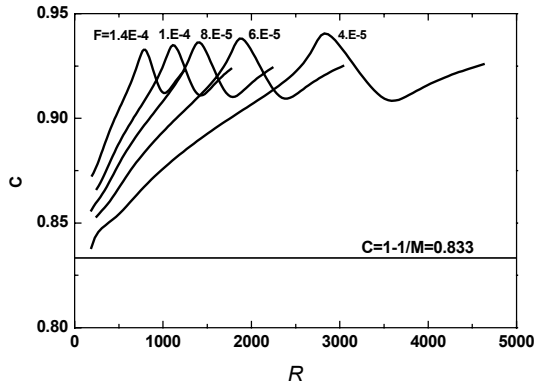


Fig. 3 Second-mode phase speed as a function of Reynolds number at various frequencies.

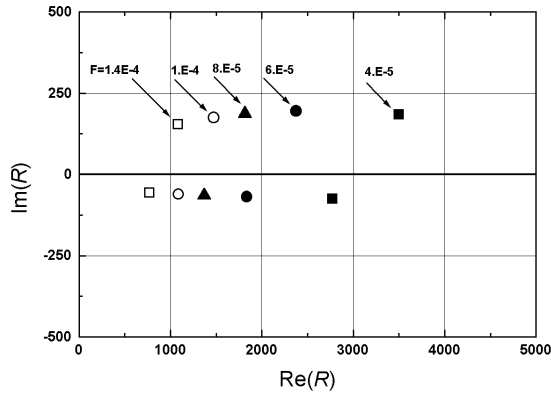


Fig. 4 Branch points in complex R -plane at various frequencies.

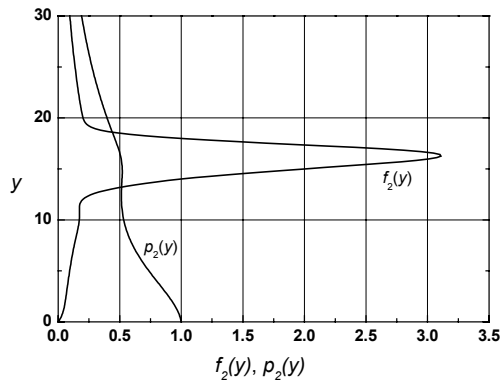


Fig. 5 Second-mode eigenfunctions for pressure $p_2(y)$ and streamwise mass flux $f_2(y)$ near the lower neutral curve: $R = 1000$, $F = 8 \times 10^{-5}$.

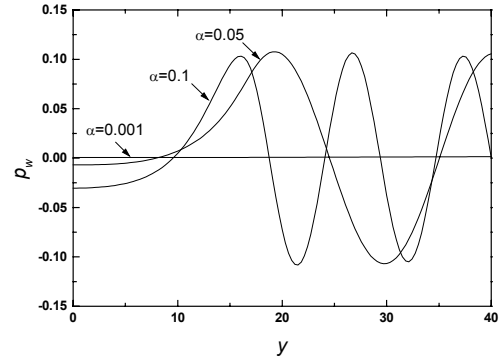


Fig. 6 Distributions $\text{Re}[p_w(y)]$ for wall-induced perturbation at various wavenumbers $\alpha = \alpha_w$; $R = 1000$.

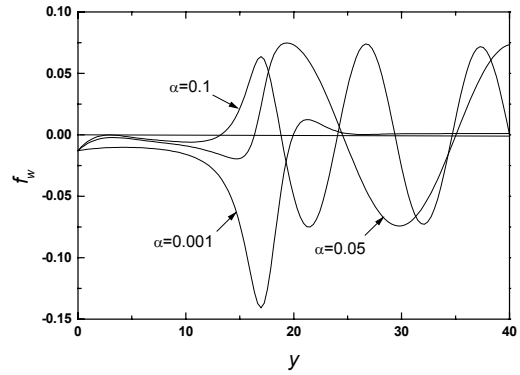


Fig. 7 Mass-flux distributions $\text{Re}(f_w(y))$ for wall-induced perturbation at various wavenumbers $\alpha = \alpha_w$; $R = 1000$.

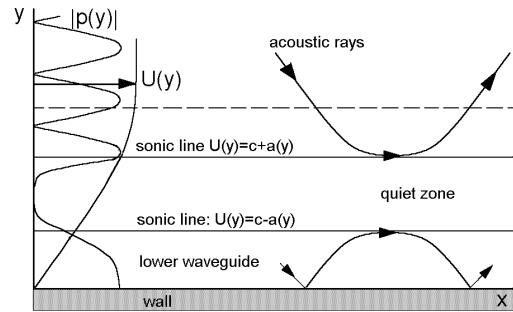


Fig. 8 Scheme of acoustic field in the boundary layer.

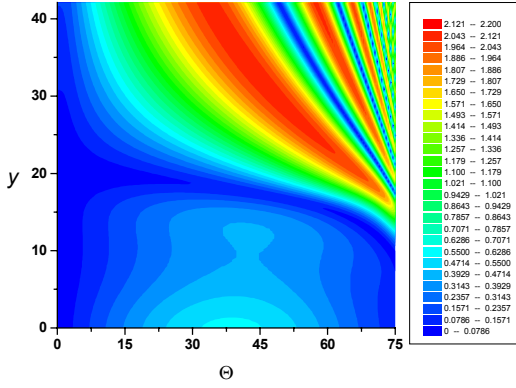


Fig. 9 Contours $|p_a(y, \Theta)| = \text{const}$ for slow waves; $R = 1000$, $F = 8 \times 10^{-5}$.

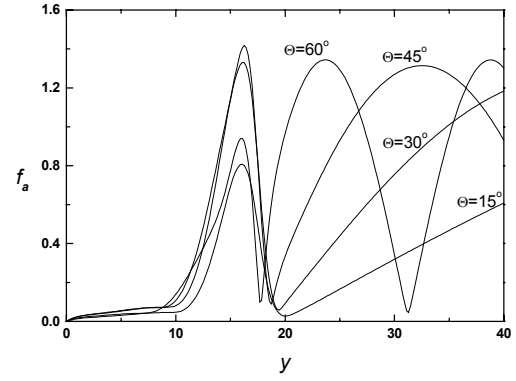


Fig. 12 Distributions $|f_a(y, \Theta)|$ at various incident angles for slow waves $R = 1000$, $F = 8 \times 10^{-5}$.

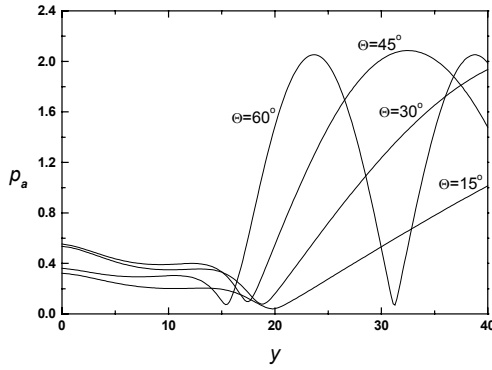


Fig. 10 Distributions $|p_a(y, \Theta)|$ at various incident angles for slow waves, $R = 1000$, $F = 8 \times 10^{-5}$.

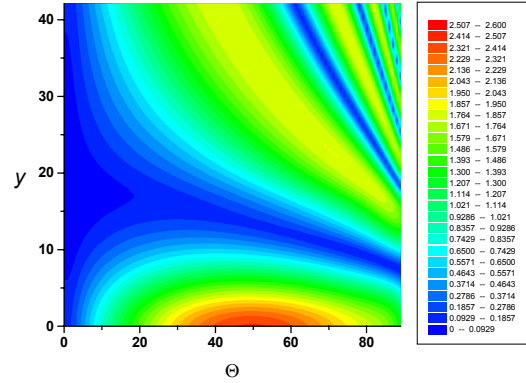


Fig. 13 Contours $|p_a(y, \Theta)| = \text{const}$ for fast waves; $R = 1000$, $F = 8 \times 10^{-5}$.

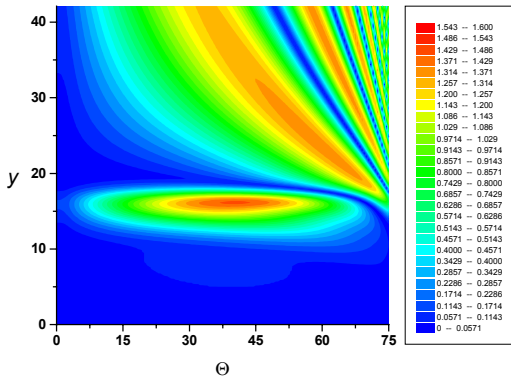


Fig. 11 Contours of $|f_a(y, \Theta)| = \text{const}$ for slow waves; $R = 1000$, $F = 8 \times 10^{-5}$.

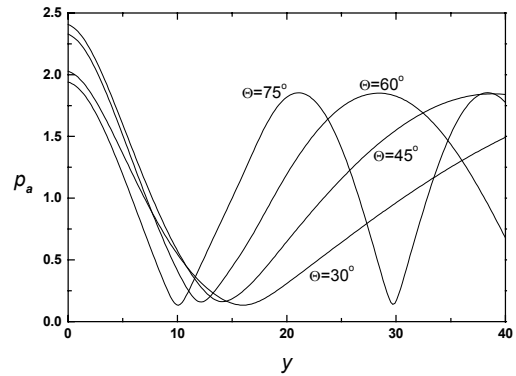


Fig. 14 Distributions $|p_a(y, \Theta)|$ at various incident angles for fast waves, $R = 1000$, $F = 8 \times 10^{-5}$.

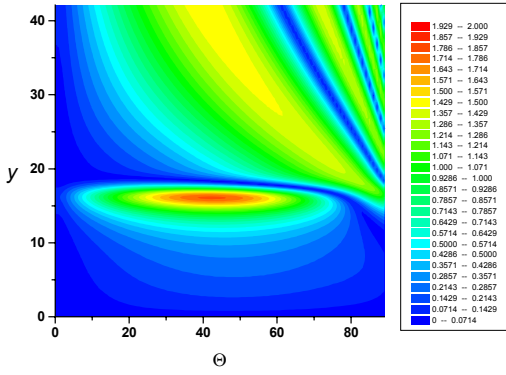


Fig. 15 Contours $|f_a(y, \Theta)| = \text{const}$ for fast waves;
 $R = 1000$, $F = 8 \times 10^{-5}$.

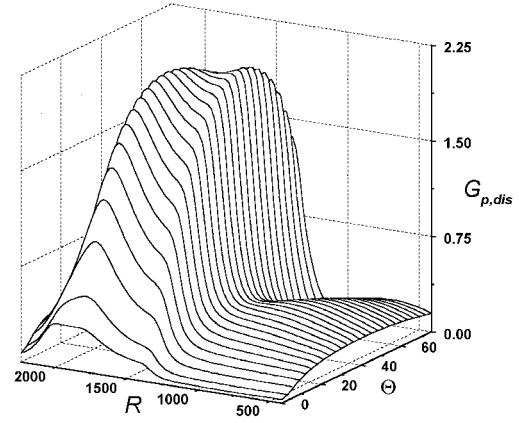


Fig. 18 Distributed receptivity function for fast acoustic waves; $F = 8 \times 10^{-5}$.

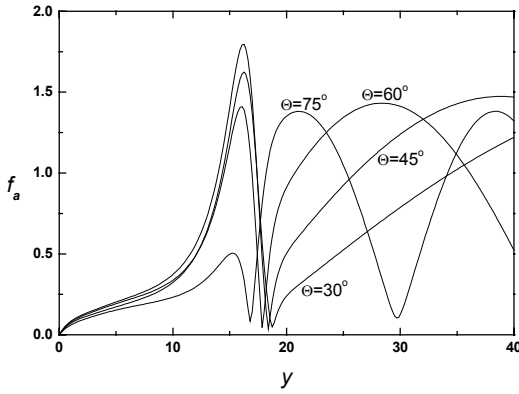


Fig. 16 Mass-flux amplitude $|f_a(y, \Theta)|$ at various Θ for fast waves; $R = 1000$, $F = 8 \times 10^{-5}$.

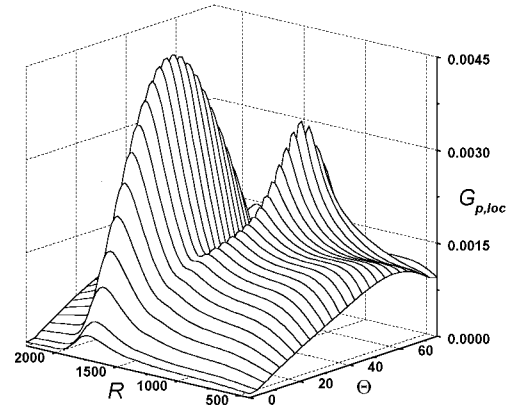


Fig. 19 Local receptivity function for slow acoustic waves; $F = 8 \times 10^{-5}$.

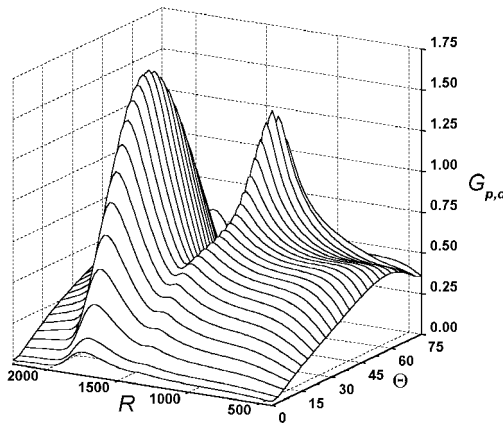


Fig. 17 Distributed receptivity function for slow acoustic waves; $F = 8 \times 10^{-5}$.

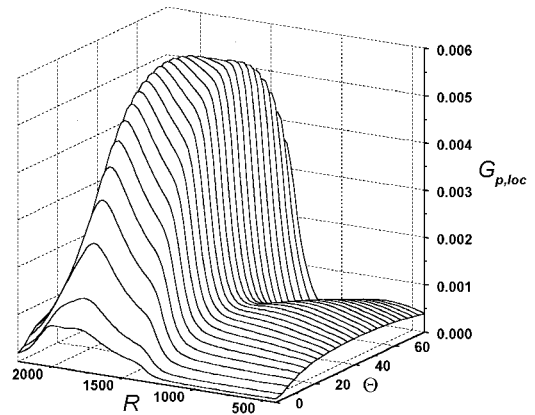


Fig. 20 Local receptivity function $G_{p,loc}(\Theta, R)$ for fast acoustic waves; $F = 8 \times 10^{-5}$.